VERTICALLY ALIGNED NANOCOMPOSITE THIN FILMS

A Dissertation

by

ZHENXING BI

Submitted to the Office of Graduate Studies of
Texas A&M University
in partial fulfillment of the requirements for the degree of

DOCTOR OF PHILOSOPHY

May 2011

Major Subject: Electrical Engineering

VERTICALLY ALIGNED NANOCOMPOSITE THIN FILMS

A Dissertation

by

ZHENXING BI

Submitted to the Office of Graduate Studies of
Texas A&M University
in partial fulfillment of the requirements for the degree of

DOCTOR OF PHILOSOPHY

Approved by:

Chair of Committee,	Haiyan Wang
Committee Members,	Xing Cheng
	Deepa Kundur
	Xinghang Zhang
Head of Department,	Costas Georghiades

May 2011

Major Subject: Electrical Engineering

ABSTRACT

Vertically Aligned Nanocomposite Thin Films. (May 2011)

Zhenxing Bi, B.E., Tianjin University, China;

M.E., Tianjin University, China;

Chair of Advisory Committee: Dr. Haiyan Wang

Vertically aligned nanocomposite (VAN) thin films have recently stimulated significant research interest to achieve better material functionality or multifunctionalities. In VAN thin films, both phases grow epitaxially in parallel on given substrates and form a unique nano-checkerboard structure. Multiple strains, including the vertical strain which along the vertical interface and the substrate induced strain which along the film and substrate interface, exist in VAN thin films. The competition of these strains gives a promise to tune the material lattice structure and future more the nanocomposite film physical properties. Those two phases in the VAN thin films are selected based on their growth kinetics, thermodynamic stability and epitaxial growth ability on given substrates.

In the present work, we investigated unique epitaxial two-phase VAN $(BiFeO_3)_x$:$(Sm_2O_3)_{1-x}$ and $(La_{0.7}Sr_{0.3}MnO_3)_x$:$(Mn_3O_4)_{1-x}$ thin film systems by pulsed laser deposition. These VAN thin films exhibit a highly ordered vertical columnar structure with good epitaxial quality. The strain of the two phases can be tuned by deposition parameters, e.g. deposition frequency and film composition. Their strain tunability is

found to be related directly to the systematic variation of the column widths and domain structures. Their physical properties, such as dielectric loss and ferromagnetisms can be tuned systematically by this variation.

The growth morphology, microstructure and material functionalities of VAN thin films can be varied by modifying the phase ratio, substrate orientation or deposition conditions. Systematic study has been done on growing $(SrTiO_3)_{0.5}$:$(MgO)_{0.5}$ VAN thin films on $SrTiO_3$ and MgO substrates, respectively. The variation of column width demonstrates the substrate induced strain plays another important role in the VAN thin film growth.

The VAN thin films also hold promise in achieving porous thin films with ordered nanopores by thermal treatment. We selected $(BiFeO_3)_{0.5}$:$(Sm_2O_3)_{0.5}$ VAN thin films as a template and get uniformly distributed bi-layered nanopores. Controllable porosity can be achieved by adjusting the microstructure of VAN $(BiFeO_3)$:(Sm_2O_3) thin films and the annealing parameters. In situ heating experiments within a transmission electron microscope column provide direct observations into the phases transformation, evaporation and structure reconstruction during the annealing.

Systematic study in this dissertation demonstrate that the vertically aligned nanocomposite microstructure is a brand new architecture in thin films and an exciting approach that promises tunable material functionalities as well as novel nanostructures.

Dedicated to my parents

ACKNOWLEDGEMENTS

It is so hard to describe all my appreciation to my advisor, Dr. Haiyan Wang. She is a nice person who makes the group like a family, but she is also tough and always wants her students to be the best. She showed me the way to do research and forced me to build a rigid work style. She never slowed down her steps and confirmed for us that the only way to success is hard work. I was so lucky that I could study for my Ph.D. under her supervision and those four years will be the most important period of my life.

I thank all my committee members, Dr. Xing Chen, Dr. Deepa Kundur and Dr. Xinghang Zhang, for their great help and continued attention on my research work. I also thank Dr. Fred Strieter and Dr. Andreas Holzenburg, for their great classes given in IC fabrication and transmission electron microscopy. I also appreciate all the great help from Dr. Zhiping Luo. He trained me in the operation of TEM facilities and always was a good tutor.

Special appreciation goes to our collaborators Dr. Judith Driscoll at the University of Cambridge and Dr. Quanxi Jia at Los Alamos National Lab. I thank Emily Weal for all the exciting collaboration work and Dr. Lata Sahonta for her great help on TEM.

It was a great experience to work with my other labmates, Jongsik Yoon, Roy Araujo, Joonhwan Lee and Chenfong Tsai in the past years. They are humorous, warm-hearted and always wanted to help others! I would like also thank my friends, Dehu, Xiangfeng, Pu, Xiaoqing and Fei! I had a colorful life in College Station together with you all.

TABLE OF CONTENTS

CHAPTER Page

CHAPTER Page

LIST OF FIGURES

FIGURE Page

FIGURE Page

FIGURE Page

FIGURE Page

FIGURE Page

FIGURE Page

FIGURE Page

FIGURE Page

FIGURE Page

LIST OF TABLES

CHAPTER I

INTRODUCTION

This chapter presents the motivation and objectives of the research in this dissertation. Vertically aligned nanocomposite (VAN) thin films are one of the most promising material architectures that can achieve tunable strain control, further more diverse material physical properties as well as novel nanostructures. The VAN architectures are also rich in the growth mechanism study of nanoscale multiple phases. Literature review in this chapter summarizes the structures, properties and strain tuning in oxide thin films and the needs of VAN structures.

1.1 Overview

Over the past several decades, new discoveries and major advances have been made to enhance the understanding of metal-oxides and their properties such as magnetism, ferroelectricity, and superconductivity. While multifunctionalities in epitaxial nanocomposite films are technologically interesting, the implication of strain resulting from elastic coupling is vital not only for the control of multifunctionalities but also for a range of applications where strain in films is critical. The research work

---

This dissertation follows the style of Journal of Applied Physics.

in this dissertation focuses on VAN oxide thin films – the growth mechanism(s), strain tunability, interface engineering and novel nanostructures achieved from VAN thin films.

In VAN thin films, two phases are self-assembled heteroepitaxially grown on given substrates and form a unique nano-checkerboard structure in-plane. Both phases grow alternatively as columns with lattice matching next to each other. The VAN thin film system exhibit many interesting physical properties with its unique microstructure.

The VAN architecture promises a novel way of achieving multifunctionality and tunable strains which is very different from the situation on normal composite films. In the first part of the main content (Chapter III), we investigate the strain control as well as tunable physical properties of $(BiFeO_3)_x$:$(Sm_2O_3)_{1-x}$ VAN thin films. We demonstrate that the strains of the two phases in both out-of-plane and in-plane directions can be tuned by the deposition parameters during growth, which found to be directly related to the systematic variation of the column widths in the nanocomposite. The dielectric property measurement shows that increasing vertical strain control will lead to a systematic dielectric loss reduction in the VAN thin films.

VAN thin film is a "smart" system that can control or improve material functionalities at nano-scale with existing processing techniques. In the second part of the main content (Chapters IV and V), we analysis the interface effects including domain and grain boundary (GB) structures in $(La_{0.7}Sr_{0.3}MnO_3)_{0.7}$:$(Mn_3O_4)_{0.3}$ VAN thin films. Tunable strain is found directly related to microstructure tuning of VAN thin films grown at different deposition frequencies. Physical properties including

saturation magnetization, Curie temperature (T_c), magnetoresistance and metal-insulator transition temperature (T_{MI}), all show systematic trends as the domain/GBs varies.

There are many VAN thin films systems have been developed till now. However, the growth mechanism of VAN thin film is not yet clear and currently the VAN architectures are limited to oxides. In the third part of the main content (Chapter VI), we present a brand new $(SrTiO_3)_{0.5}$:$(MgO)_{0.5}$ VAN system as a model to study the substrate strain effect on VAN thin film growth. The column width of VAN thin films grown on MgO substrate is much larger as compare to that of VAN thin films grown on $SrTiO_3$ substrate. Substrate induced surface tension is proved to be a critical factor that will affect the adatoms' surface diffusion during the VAN growth.

The VAN thin film can also be a promising template for developing various nanostructures such as nanowires, nanorods and nanopores. In the forth part of the main content (Chapter VII), we developed porous thin films with ordered nanopores that were processed by thermal treatment on VAN thin films. Controllable porosity can be achieved by adjusting the microstructure of VAN thin films as well as the annealing parameters. In situ heating experiments within a transmission electron microscope (TEM) column provides significant insights into the phases transformation, evaporation and structure reconstruction during the thermal process.

1.2 Functional oxide thin films

Functional oxides represent a number of smart oxide systems in which the physical and chemical properties of the oxides can be tuned through adjusting the anion deficiency or cation valence states.[1] They have diverse crystal structures with unique properties covering all aspects of condensed matter physics and solid state chemistry including semiconductivity, superconductivity, ferroelectricity, magnetism and piezoelectricity.

Oxide materials have shown a broad range of interesting physical properties and the modern study on functional oxide thin films has been largely driven by the development of new thin films growth techniques and material characterization methods.[2] Advanced thin film growth techniques allow non-equilibrium deposition conditions which lead to large variation in microstructure, oxygen content and other film properties. Also the high quality of currently grown thin films permits the study of defect free physical properties in the form of epitaxial films, multilayers, superlattices and vertically aligned multiphase nanocomposite films. Ultra-thin functional oxide films (<100nm) are now of great interest in investigating fundamental defect chemical properties of low-dimensional systems. Various applications of ultra-thin oxide films have been achieved in electronic and renewable energy technologies. [2]

1.2.1 Structures of oxide thin films

With a wide range of structures and properties, metal-oxides have been the most widely investigated functional oxide materials.[3] Metal oxide materials have natural ionic bonds and can be categorized to binary oxides and ternary oxides as shown in Table 1.1. Common structures of binary oxide materials include rock salt, wurtzite, fluorite, rutile and corundum. Common structures of ternary oxide materials include ilmenite, spinel, perovskite and perovskite derived structures such as ruddlesden-popper series and other layered-perovskite structures. Those structures cover most of the metal-oxide materials, and from chemical bonding to doping, the chemical structures of the material largely interact with the electronic structures. Among those complex oxides, perovskite structure materials exhibit a large variety of functional behavior and have gained increasing significance with attractive properties as insulating dielectrics, metals, ferro/antiferroelectrics, multiferroics and thermoelectrics.[4] Perovskites are cubic or pseudocubic ABO_3-type earned the name from the prototype $CaTiO_3$ mineral as shown in Figure 1.1. It has a corner shared octahedral in unit cell with A-cation and B-cation coordinated by 12 and 6 oxygen ions, respectively.[4] The ionic radius of A-cation is larger than that of the B-cation, and the structure accommodates a wide range of valence states which make the perovskite structure acts as a collection of a wide range of structures.[4,5]

Table 1.1. The category of common metal-oxide materials.

System	Structure	Standard materials
Binary oxide	Rock salt	MgO, TiO, VO, CoO, MnO
	Wurtzite	ZnO, BeO
	Fluorite	CeO_2, ThO_2, ZrO_2
	Rutile	TiO_2, IrO_2, MoO_2, RuO_2, WO_2
	Corundum	Al_2O_3, V_2O_3, Cr_2O_3
Ternary oxide	Ilmenite	$FeTiO_3$, $MnTiO_3$, $LiNbO_3$
	Spinel	$MgAl_2O_4$, $CoFeO_4$, $LiTi_2O_4$
	Perovskite	$BiFeO_3$, $CaTiO_3$, $SrRuO_3$
	Layered perovskite	$YBa_2Cu_3O_7$
	Ruddlesden-popper series	$SrRuO_3$, Sr_2RuO_4, $Sr_3Ru_2O_7$

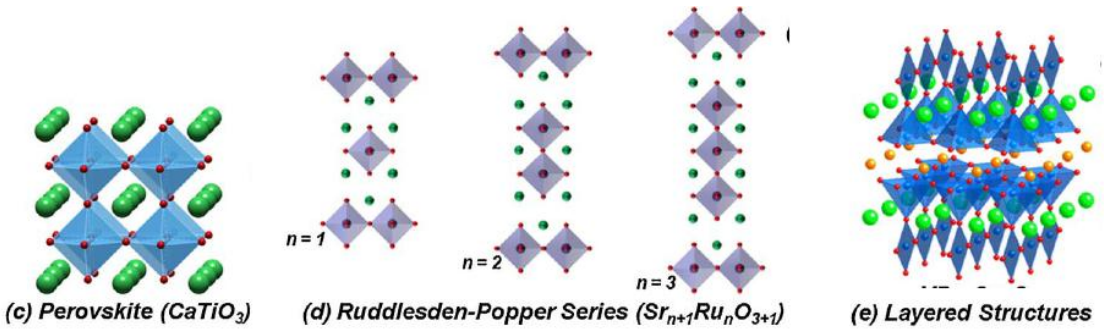

FIG. 1.1. Crystal structures of (a) perovskite and the derivatives of perovskite such as (b) Ruddlesden-Popper series and (c) layered perovskites.

There are two most important perovskite structure materials worth to be noted here. The first one is intrinsically layered perovskite (ABO_3 type) in the form of $Re_{1-x}AE_xMnO_3$, where RE is trivalent rare earth cation and AE is divalent alkaline earth cation, Figure 1.2 shows the ideal cubic $LaMnO_3$ perovskite structure. The large size Re trivalent ions and AE divalent ions occupy the A-site with 12-fold oxygen coordination.[6] These mixed-valence perovskite have a rich and complex physics related to the electron-lattice and electron-electron interactions. The second one is $BiFeO_3$ which is the most studied multiferroic material that can reveal the multiferroic origin. As shown in Figure 1.3, the structure of bulk $BiFeO_3$ can be described as a distorted perovskite.[7] The absence of centrosymmetry in the R3c allows the relative displacements of the atomic sublattices along (111) where the Bi ions are with respect to the distortion of FeO_6 cage. The $BiFeO_3$ thin films are in tetragonal structure which is similar to cubic perovskite with symmetry lowered to P4mm.

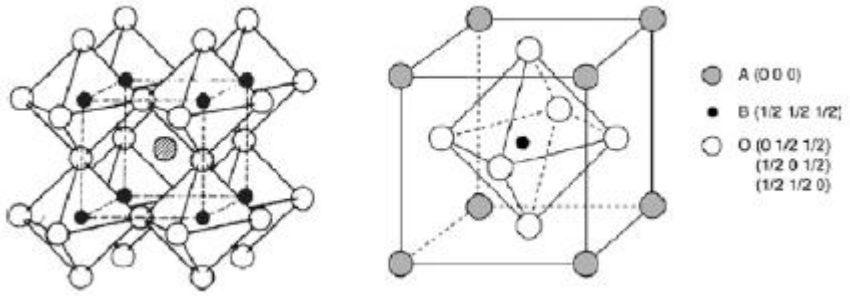

FIG. 1.2. Schematic of the $LaMnO_3$ cubic perovskite structure, where trivalent rare earth (RE) cation and divalent alkaline earth (AE) cation shared the A-site.

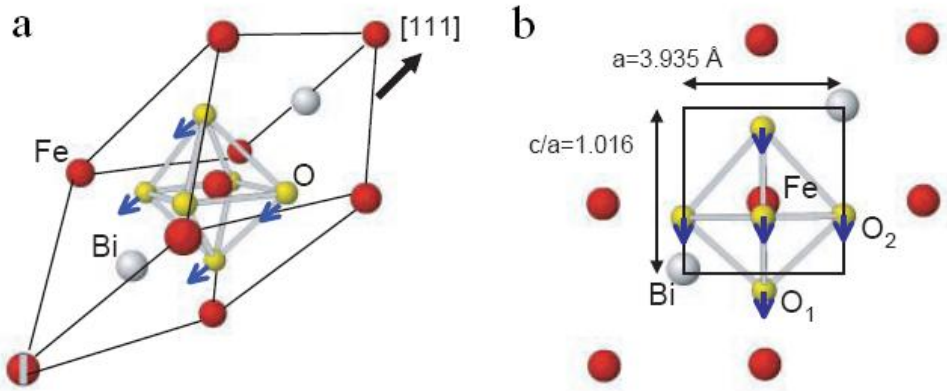

FIG. 1.3. Schematic of the $BiFeO_3$ with distorted perovskite structures. (a) Bulk $BiFeO_3$ in rhombohedral structure and (b) $BiFeO_3$ thin film in tetragonal structure.

Besides single phase oxide thin films, multiphase nanocomposite oxides have attracted extensive research interest. Nanocomposites consist of nanosized particles embedded in different materials matrix.[8] In recent years, high quality nanocrystalline materials have shown novel physical, chemical, magnetic, optical and electrical properties. Some interesting phenomena including nonlinear optical behavior and quantum confinement effects of carriers have been reported in nanocomposite materials. Nanocomposite thin films posses many unique physical properties that could not be realized with single phase thin films. The nanocomposite thin films can be classified based on some criteria such as material function, processing and microstructures. Besides nanoconposite oxide thin films, there are also polymer nanocomposites, metal nanocomposites, metal/polymer nanocomposites and metal/semiconductor nanocomposites.[9] Physical vapor deposition techniques are the main technologies till now to grow high quality nanocomposite thin films. Either single composite target or multiple single phase targets will be involved in sputtering or pulsed laser deposition.[10]

1.2.2 The growth of oxide thin films

Most of the modern oxide thin films are deposited under vacuum, by various thin film deposition techniques. Basically, the oxide thin film deposition technologies can be divided as either purely physical ones, such as evaporative methods, or purely chemical ones, such as gas- and liquid-phase chemical process. There are also a considerable number of processes that are based on glow discharges and reactive

sputtering which combine both physical and chemical reactions. Table 1.2 summarizes and compares several typical thin film deposition techniques for oxide growth.

Physical vapor deposition (PVD) techniques include electron-beam evaporation, molecular beam epitaxy (MBE), pulsed laser deposition (PLD) and magnetron sputtering. Those are with relatively simple system set up and can give good surface coverage and smooth surface. PVD techniques fit for the growth of almost all materials and can provide good film stoichiometry for complex composites. Chemical vapor deposition (CVD) techniques deposit film through chemical reactions and surface absorptions. In CVD systems, vapor gases are introduced into the deposition chamber that react and form the desired film on the surface of the substrate. CVD techniques include low-pressure CVD (LPCVD), plasma-enhanced CVD, metal-organic CVD and atomic layer CVD (ALD). Above PVD and CVD are all vacuum based techniques that usually selected to grow thin films. With those systems, the film density, microstructure, stoichiometry as well as other properties can be easily controlled.

Besides the vacuum based techniques, there are other thin films deposition systems that have been developed recently and started to drawn more attention. Those techniques include liquid phase epitaxy (LPE) and solution-based techniques (sol-gel and polymer assisted deposition). These are non-vacuum techniques and more cost-effective. These techniques are widely used in large industrial applications where the material microstructure property is not the first consideration.

Table 1.2. The comparison of different thin film deposition techniques.

		Main Features	Advantages	Disadvantages
PVD	E-beam evaporation	High-energy beam fired from an electron gun to boil a target material	Both metal and dielectrics can be deposited	Poor film uniformity and film density, high cost.
	MBE	Low energy thermal atomic beams of each component generated by heater/ e-beam evaporators	Good film stoichiometry and epitaxial quality, in-situ diagnosis.	High cost, low through put.
	PLD	High-power laser as external energy source to vaporize materials and deposit thin films	Can deposite all metals and complex ceramic materials, reproduction of stoichiometry	High cost of laser source, small surface coverage and formation of particulates.
	Magnetron Sputtering	Using magnetic field to confine electrons near the target to sustain plasma.	Denser film, smaller grain size and better film adhesion.	Poor growth directionality
CVD	LPCVD	The lowering pressure of gas stream increases the diffusion and extends the reaction to higher temperature.	High deposition rate, good film uniformity and density	No gas-phase collisions occur in the near furface region at low temperature, high cost.
	PECVD	Plasma source used to supply additional energy and reduce reaction temperature	Low deposition temperature, high deposition rate.	Nonequilibrium process and nonstoichiometric
	MOCVD	CVD processes based on metal-organic precursors	High film quality and throughput, large area production.	Not for all materials, require high temperatures.
	ALD	Two complementary precursors alternatively introduced into the reaction chamber	Extremely precise control of film thicnkess and uniformity	Low throughput, high cost.
Others	LPE	Top seeded solution growth method with a substrate introduced vertically	High quality films and high deposition rate	Ultra high temperature needed, hard to deposite thin films
	Solution-based	Transition of a system from liquid phase to solid phase.	Simple technique and low cost	Poor surface roughness and coverage

There are no other thin film growth techniques that have gained as much attention as PLD in the past decades for oxide growth. This is a relative simple thin film growth process with many advantages. In a typical PLD system, the target surface species are ionized by laser ablation and the transfer of atomic and ionic species from the target enables the growth of films in certain composition.[11] Oxygen is always involved to complete the oxidation of oxide films and no other background gases are required. The details of oxide films deposited by PLD will be discussed in Chapter II.

One of the primary research limitations on functional oxide thin films was the difficulty in achieving precise property control in films due to a large range of possible defects. It has been reported that the point defect concentration in oxide thin films can significantly modulate the electrical and electrochemical responses.[12,13] Also the oxygen vacancies play a critical role in enabling magnetic properties in complex oxides. In addition to controlling above equilibrium defects by either growth temperature and post-annealing treatments, the growth kinetics and growth mode both play important roles in achieving high-quality defect free oxide thin films.[14]

1.2.3 Physical properties of oxide thin films

Functional oxide thin films are an important class of materials: from both scientific and technological perspectives where they present interesting physical phenomenon including electrical, optical, ferromagnetic and ferroelectric properties.

1.2.3.1 Electrical and optical properties

Oxide thin films with homo and hetero structures are attractive for future optoelectrical devices with their exciting fundamental intrinsic and extrinsic optical and electrical properties. In the class of optoelectronic materials, ZnO attracts the most attention because of its direct and wide band gap and its ability to tailor electronic, magnetic and optical properties through doping, alloying, quantum wells, heterostructures and nano-engineering.[15,16] ZnO is a wide band gap, optoelectronic material belonging to II-VI family of semiconductors. The stable crystalline of ZnO is in wurtzitic hexagonal structure, as shown in Figure 1.4, in which the Zn and O planes are alternately stacked along the c-axis direction with lattice parameters a=0.3296nm and c=0.52065nm.[17] The tetrahedral coordination in ZnO results in a lack of a centre symmetry in wurtzite combined with large electromechanical coupling properties.

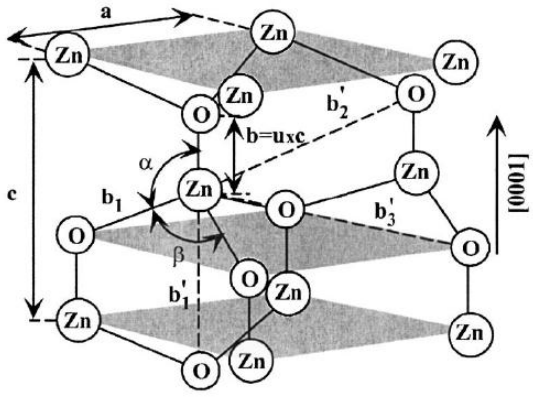

FIG. 1.4. Schematic of wurtzitic ZnO crystal structure.

ZnO has a direct energy bandgap of 3.3 eV at room temperature. The energy band parameters, such as electron and hole effective masses, as well as optical and electrical properties are quite comparable to that of GaN, and well established for blue LED and semiconductor laser diode. However, ZnO is a more intense and efficient UV emitter at its band edge as compare with that of GaN, owning to the advantage that it has a higher free exaction binding energy of 60meV which is more than twice of that in GaN. The radiate recombination in ZnO is mediated by exactions. That will lead to narrow emission line widths, where the band-to-band in other systems yielding broad bandwidths. Based on these properties, ZnO system has a niche for a wide range of devices applications such as blue and UV light emitting diodes, heterojunction diode lasers, visible and solar blind UV light detectors.

The optical properties of ZnO are connected with both intrinsic and extrinsic effects. Intrinsic optical transitions take place between the electrons in the conduction band and holes in the valence band, including exaction effects due tot the coulomb interaction. The optical transitions in ZnO have been studied by a variety of experimental techniques such as optical absorption and transmission. It has been reported that the excitonic absorption features were sharper in ZnO thin films annealed in oxygen.[18] In the photo reflectance study of high quality ZnO epitaxial layers, a larger broadening was observed for the B and C excitons compared to the A exciton, which due to a contribution by the exciton polaritons in terms of large splitting of the respective excitons.[19]

With a direct and large band gap material, ZnO also have advantages include higher breakdown voltages, lower noise generation, and high temperature and high power operation. The electron transport in ZnO thin films can be considered for low and high electric fields. The room temperature ZnO thin films mobility values are comparable to the value of bulk ones. It has been reported that the best reproducible electron mobilities from 115 up to 155 cm^2/Vs at 300K in nominally undoped ZnO thin films of total thickness of 1-2 um grown on C-sapphire substrates by a multistep PLD technique. To attain potential high conductivity, both high quality n- and p- type dopings in ZnO are required. Unintentionally doped ZnO is n type whether the donors are Zn or O. The main obstacle to the development of ZnO has been the lack of reproducible and low-resistivity p-type ZnO. Dopants may be compensated by low-energy native defects, such as Zn or O, or background impurities. Low solubility of the dopants in the host material is also another possibility.

1.2.3.2 Magnetism and magnetotransport properties

Magnetism is a property of materials that respond at atomic or subatomic level to an applied magnetic field. The definition of magnetism lies in the orbital and spin motions of electrons and how the electrons interact with one another. As a matter of fact, all matter is magnetic and some materials are much more magnetic than others. The main distinction corresponds to the interaction of atomic magnetic moments.

There are a few materials which are naturally magnetic and can be turned into magnets. For example, iron, hematite, magnetite and ionized gases.[20]

The theory of magnetism is a rich field, and is built upon the idea of the quantum mechanical exchange energy which causes electrons with parallel spins at lower energy than spins with anti-parallel spin at higher energy. Ferromagnetic materials exhibit parallel alignment of moments resulting in large net magnetization even in the absence of a magnetic field. Anti-ferromagnetism represents the case of all sublattice moments are exactly equal but opposite and the net moment is zero. As for ferrimagnetism, the magnetic moments of sublattices are not equal and result in a net magnetic moment. [21]

There are a number of fundamental ideas of coupling in magnetic oxide materials that have been developed to address how indirect exchange interacts through non-magnetic ions like oxygen. Classic models including super-exchange, double exchange and RKKY coupling are shown in Figure 1.5.[5] Super-exchange model describes the normally short range exchange interaction can extend to a longer range.[22] Figure 1.5a shows an oxygen bonding leads to an anti-parallel spin alignment of nearest neighboring Mn ions in $LaMnO_3$. Double exchange describes the magnetic coupling of A site doped ABO_3 type pervoskites (like Sr or Ca doped $LaMnO_3$) which is called mixed valence compounds.[23] In these materials, as shown in Figure 1.5b, electrons on the Mn sites jumps back and forth across the oxygen and delocalized over the entire Mn-O-Mn. This model can explain magnetic structures with identical Mn ions and further ferromagnetic alignments. The RKKY coupling represents the case where

magnetic ions are too far to interact with each other, and the local moment will induce a spin polarization in surrounding conduction electron sea.[24]

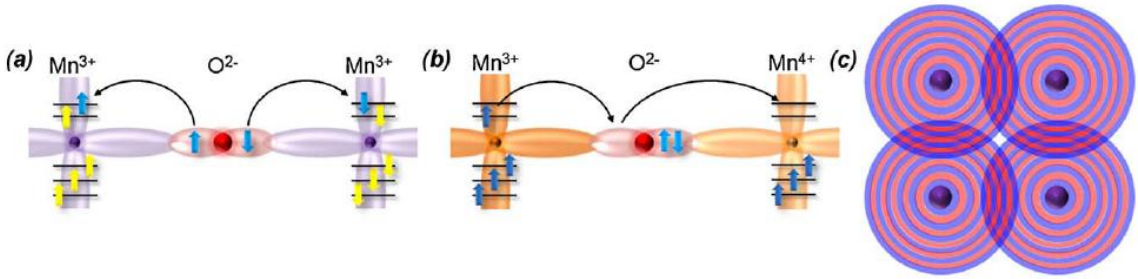

FIG. 1.5. Schematic illustrations of magnetic coupling in oxides. (a) Superexchange, (b) double exchange, and (c) RKKY coupling.

Ferro- and ferri-magnetic oxides are half-metallic and the most interesting candidates for the study of extrinsic magnetotransport phenomena. Following with the discovery of high temperature superconductivity in the mid-1990s, mixed-valence perovskites manganese oxides have received much attention. These manganese oxides have remarkable interrelated structural, magnetic and transport properties induced by the mixed valence of the Mn^{3+} and Mn^{4+} ions. Historically they led to new physical concepts such as double exchange and the Jahn-Teller effect.[25] More recent work on oxide thin films has revealed new phenomena including colossal magnetoresistance

(CMR), low field magnetoresistance (LFMR) and optically-induced magnetic phase transitions.

The CMR effect is attributed to the ratio of the Mn^{3+} and Mn^{4+} ions in the perovskite and sensitive to the partial doping of the trivalent RE ion by divalent AE cation. The doped perovskite manganites have strong correlation between the structure and electronic magnetic phases. One of the origins of the lattice distortion is the deformation of the MnO_6 octahedron called Jahn-Teller effect and the other one comes from the connection pattern of the MnO_6 octahedra in the perovskite structure governed by the tolerance factor t where

$$t = \frac{d_{A-O}}{\sqrt{2}d_{Mn-O}} = \frac{\langle r_A \rangle + r_o}{\sqrt{2}(\langle r_{Mn} \rangle + r_o)} \qquad (1.1)$$

Jahn-Teller effect describes the lifting of degeneracy due to the orbital-lattice interaction in the MnO_6 octahedral which is the basic building blocks of the maganites. It tends to occur spontaneously as the lattice distortion grows while the energy splitting of other degenerate orbitals is in linear. The tolerance factor reveals the Mn-O-Mn bond angle as well as the ionic radii of the A-site cations. It is also dependent on both doping level temperature and pressure.

The magnetic properties of the manganites are also governed by exchange interactions between the Mn ion spins. Zener proposed the double-exchange model to ensure the strong ferromagnetic type interaction of Mn^{3+}-O-Mn^{4+}.[26] The probability of the e_g electron transfer from Mn^{3+} to neighboring Mn^{4+} is $t_o\cos(\text{theta}/2)$, theta being the angle between the Mn spins, in the case of strong Hund coupling. The electron transfer

as well as the energy gain of the parallel spin configuration all reveals the ferromagnetic character of the double-exchange interaction.

As a metal-insulator transition of mixed-valence manganese oxides, CMR interprets the phenomena of by applying external magnetic field, some mangnetes show large negative mangnetoresistance with peaks at about Curie temperature T_c.[27,28] It has been reported that the resistance ratio $R(0)/R(6T)>10^2$ was observed in $La_{0.67}Ca_{0.33}MnO_3$ thin films which close to 500% with T_c = 260K. This enormous factor reveals a thousand-fold change in resistivity with and without magnetic field. The interpretations of CMR were based on the double exchange model and Hund's coupling. However, those models do not matched with the electron-phonon interaction and new theoretical models have been proposed. [29]

The CMR of mixed-valence manganites requires a large applied magnetic field and are restrict to specific temperature region which limits its application potential. Another extrinsic magnetic transport effect called LFMR can be observed at low magnetic field (<0.1T) and the grain boundary plays the dominant role over all.[30,31] The LFMR interprets the spin-polarized tunneling (SPT) through electronic barriers across the grain boundaries (GBs). Much work has been done to figure out the role of nature and size of GBs in polycrystalline bulk, polycrystalline and epitaxial films, and nanocomposite films.[32,6] The LFMR has been found to depend on the degree of texturing in polycrystalline and nanocomposite thin films and show substantial MR over a wide temperature range. [33,34,35] The importance f manganite composites has been

emphasized in many recent reports including epitaxial LCMO:MgO, LSMO:ZnO and LSMO:Mn_3O_4 nanocomposite thin films. [36,37,38]

1.2.3.3 Ferroelectric properties

Ferroelectrics are a group of compound crystals or thin films that have noncentrosymmetic crystal structure and posses reversible spontaneous electric dipoles which can switch directions under externally electric field or internal electric field from adjacent unit cells. The spontaneous electric polarization is due to the noncentrosymmetric crystal structure and it will disappear at above the Curie point when the thermal motion will cancel individual electron spins.

Ferroelectricity has been discovered in typical perovskite (ABO_3) $BaTiO_3$ half century ago. [39,40] As shown in Figure 1.2, perovskite crystal structure is an ideal model to investigate ferroelectric behavior and spontaneous polarization. The oxygen octahedron distortion is always accompanied with electric dipoles, and the polarization value of each unit cell also largely determined by the size of A and B cations as well as the deformation of A cations. Figure 1.6a shows the cases of isotropic perovskites $BaTiO_3$ and $PbTiO_3$. Ferroelectric perovskite can save information in the form of polarization direction in individual FE domains as they usually have totally two ground states of opposite ionic polarizations.[41] The hysteresis loop is the most important characteristic of ferroelectric thin films. As shown in Figure 1.6b, it demonstrates the polarization of ferroelectric material as a function of applied electric field.[42] One of the

most interesting ferroelectric materials that has been intensively investigated in the past decades is lead zirconate titanate ($Pb(Zr_xTi_{1-x})O_3$)(PZT), a combination of ferroelectric $PbTiO_3$ and antiferroelectric $PbZrO_3$.[41] Lead titanate preferred composition will lead to memory applications and a 50:50 Zr:Ti composition ratio usually associated with piezoelectric applications.

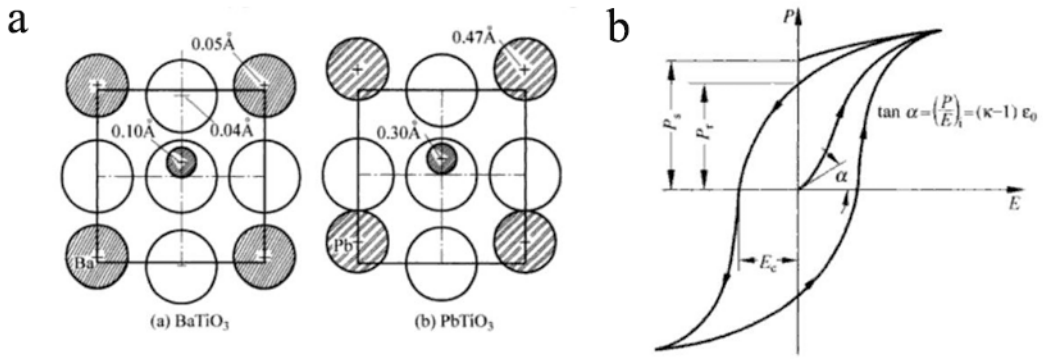

FIG. 1.6. (a) Spontaneous polarization in isotropic perovskite, $BaTiO_3$ and $PbTiO_3$. (b) Typical ferroelectric hysteresis loop for $BaTiO_3$ ceramic.

Ferroelectric of materials can be dramatically engineered and controlled in the form of thin films. Observations have been reported including size effect, strain enhancement of ferroelectricity, engineered ferroelectricity in superlattice and domain structures control in ferroelectric thin films.[43,44,45,46] Structural defects in epitaxial

ferroelectric films such as misfit dislocations (MDs) and threading dislocations (TDs) can drastically affect physical properties of the material and limit the performance as devices. The strain field surrounding dislocations will influence more in ferroelectric nanostructures due to the relativly enhanced volume of the defect regions.[47] Nagarajan reported a quantitative study on PZT ferroelectric thin films with different film compositions and thicknesses, and studied the role of dislocations.[48] One of the ways to get rid of defects in ferroelectric films is to grown the film on vicinal substrates in which the step flow will serves as a template for subsequent layer-by-layer epitaxial film growth. Another important aspect regarding ferroelectric thin films is ferroelectric domains which determine the polarization switching of the films. Domain patterns depend largely on growth conditions, substrate orientations and boundary conditions. Figure 1.7 shows a simulated phase diagram and equilibrium domain structures of $BaTiO_3$ thin film as functions of strain and temperatures. Much works has been done to investigate ferroelectric 90° and 180° domains.[49,50]

The memory density of ferroelectric materials is now still much lower (40Gbit/cm^2 in epitaxial PZT thin films) as compared with that of ferromagnetic date recordings.[51] It has been established that the ferroelectric stability can be maintained as the ferroelectric film thickness down to a few unit cells.[52] Following that, the ferroelectric nanostructures can be achieved by either classical top-down patterning process or self-assembled geometrically ordered arrays.[53,54] Considering the ultimate nanostructure shape, dimensions and material quality, the later self-assembly technique has draw more and more attention as combined with developed film growth methods.[55]

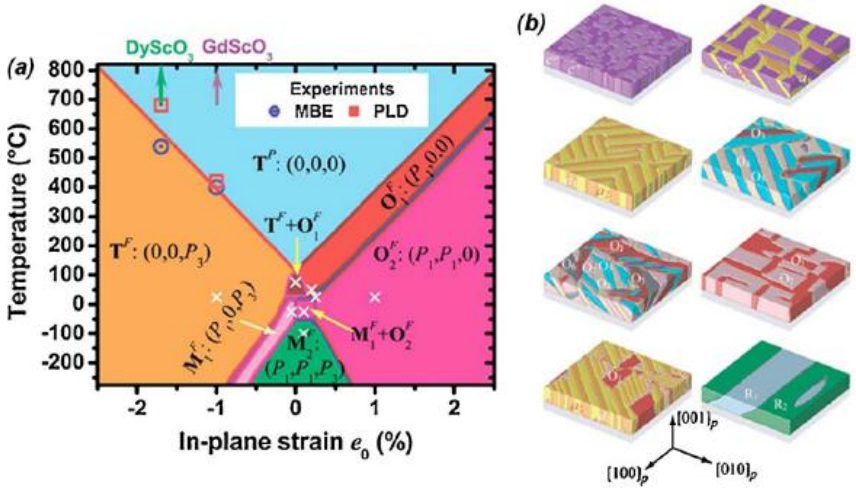

FIG. 1.7. Phase field models of ferroelectrics. (a) Phase diagram of the evolution of the structure of $BaTiO_3$ films as functions of temperature and substrate in-plane strain. (b) Simulated domain structures of $BaTiO_3$ thin films at different strain status.

1.2.3.4 Multiferroic properties

Multiferroism describes materials which show simultaneous ferroelectricity, ferromagnetism and ferroelasticity in parallel. As shown in Figure 1.8, the overlap of ferromagnetic and ferroelectric is classified as multiferroic.[56] For multiferroic in a single phase material, the atoms that move off center to form the electric dipole moment must be different from those which carry the magnetic moment and there is a possibility that electric fields can control magnetization or a magnetic field can change electric polarization.[57]

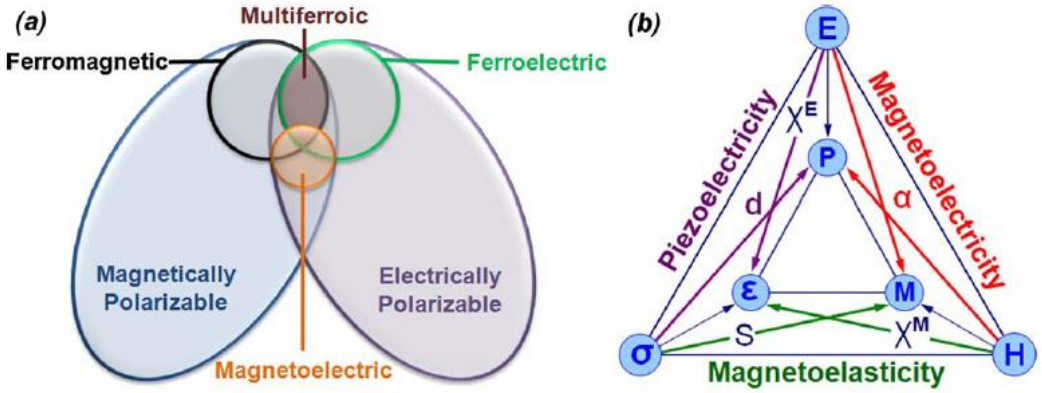

FIG. 1.8. Relationship between ferromagnetic and ferroelectric materials. (a) The requirements to achieve both in a material. (b) Schematic illustrating different types of coupling present in materials.

The earliest multiferroism study can be tracked back to the boracite $Ni_3Bi_7O_{13}I$ in the 1960s.[58] As the development of ability to product high-quality single-crystallines, epitaxial thin films and the improvement of material computational techniques, there has been a flurry research focused on multiferric materials in the past decade.[59] In general, multiferroic could be achieved through an alternative mechanism from either magnetism or ferroelectricity.[60] In the magnetic perovskite oxides, the stereochemical activity of A-site cation with a lone pair will lead to a structural distortion and ferroelectricity. Another route to multiferroism is by geometrically driven effects with long dipole interactions and anion rotations which can also drive the system to a ferroelectric state. On the other hand, there are certain materials in which magnetism

can cause ferroelectricity, the strong coupling between two order parameters can lead to multiferroism.[61]

Multiferroic materials can be categorized based on the size and type of couplings as particulate composites, laminated structures, thin films and nanocomposites.[62] Mutiferroics in thin films allow non-equilibrium phases growth and strain engineering of existing materials. To date, high-quality multiferroics thin films have shown diverse architectures including single phase epitaxial films, horizontal multilayered heterostructures and vertically aligned heterostructures (shown in Figure 1.9) to tailor their properties through strain, interfacial coupling and atomic level engineering of chemistry.

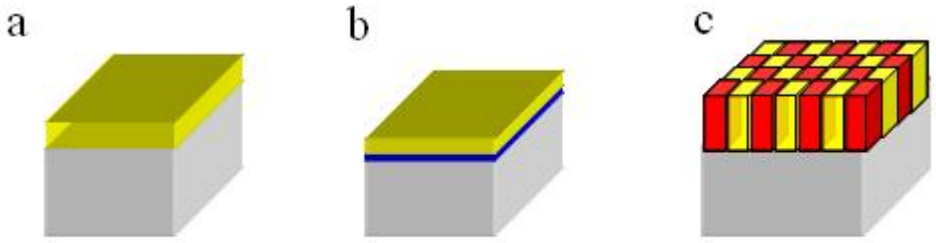

FIG. 1.9. Schematics of three types of model multiferroic thin film architectures. (a) Single phase epitaxial films grown on single-crystal substrates; (b) horizontal multilayered heterostrucures; (c) vertically aligned horizontal heterostructures.

The single-phase multiferroic thin films include only hexagonal manganites and Bi-based perovskites. The earliest hexagonal manganite has been investigated is $YMnO_3$. It shows both ferroelectric and antiferromagnet caused by the long range dipole interactions and oxygen rotations. It was also found that there are ferroelectric and antiferromagnetic domain walls coincident in $YMnO_3$ which could then rise to the magnetic coupling. Perovskite structure bismuth ferrite ($BiFeO_3$) is currently the most studies multiferroics because of its large polarization and high Curie temperature. J. Wang *et al.* reported enhancements of polarization and related properties in heteroepitaxially constrained $BiFeO_3$ thin films in 2003.[7] The structure analysis of the film suggested differences between films and bulk single crystals in enhancing the polarization up to $90uc/cm^2$ at room temperature. It also demonstrated a magnetoelectric coupling coefficient at 3V/cm Oe without applied field. Following that, much progress has been made in understanding the structure, properties and growth of BFO thin films. However, there are some conflictions in some of the reports. It was argued that the large magnetization may only arise in deoxygenated films and the impurity phases could also play a role in the multiferroic performance.[63,64]

The second thin film architecture using horizontal multilayer heterostructures takes advantages of atomic level layering to engineer specific magnetic ordering through super exchange interactions, and the compositional ordering will increase polarizations.[56] Many interesting multiferroic systems with this architecture have been demonstrated including $CaTiO_3/BaTiO_3/SrTiO_3$, $Fe/BaTiO_3$, Co-doped TiO_2/PZT etc.[65,66,67] Multiferroic materials could also be fabricated in a nanostructured columnar

structure, as shown in Figure 1.9c, as the vertically aligned horizontal heterostructures. The growth of the horizontal heterostructures requires special material selections considering lattice matching, immiscibility and different elastic modulus. Zheng *et al.* first developed $BaTiO_3$:$CoFe_2O_4$ nanocomposite in this architecture as CFO pillars embedded in BTO continued film matrix.[68] This structure showed strong magnetoelectric coupling through the changes of magnetization at ferroelectric curie temperature of BTO. The large interface-volume ratio permits the couple of two phases via strain and the perpendicular interface removes the effect of substrate clamping and allows for better strain-induced couplings. Many other composite systems with combinations of a number of perovskites have been developed including $BaTiO_3$, $PbTiO_3$, $BiFeO_3$ and spinel $CoFe_2O_4$, $NiFe_2O_4$, Fe_2O_3.[69,70,71,72] It has shown that the nanostructured multiferroics have gained significantly enhanced magnetoelectric properties over traditional multilayer heterostructures.

Multiferroic materials hold great potential for applications in aspects of ferroelectric random access memory (FeRAM) and magnetic data storage.[73] Multiferroic could lead to a new generation of memory devices that the coupling could permit data to be written electrically and read magnetically.

1.3 Strain and strain engineering in oxide thin films

1.3.1 Thin film epitaxy and strains

Strain represents the change of material's dimensions as compared with that in their equilibrium state. In the form of thin films, the strain is mainly caused by the heteroepitaxial growth where the lattice parameters of the film and the substrates are not usually identical and the coherent growth will alter the dimensions of the film materials, thus produce strain.

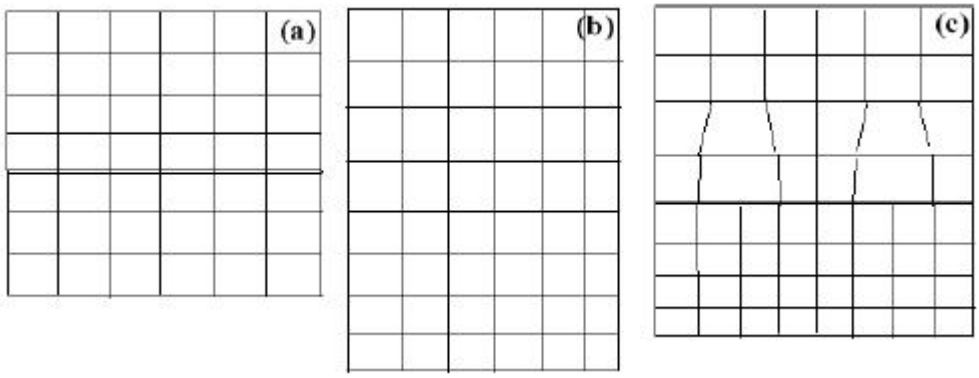

FIG. 1.10. Schematic of lattice matching in heteroepitaxy thin film growth. (a) Coherently strained lattice-mismatched heteroepitaxy; (b) lattice-matched epitaxial heterostructure; (c) incoherently growth-relaxed lattice mismatched heteroepitaxy.

Epitaxial growth of thin film and the strain engineering in thin film heterostructures are very important for the next generation of electronics, optical and magnetic devices. The epitaxy strain in thin films represents the change in a film's lattice parameters from their equilibrium values. Figure 1.10 shows three different modes of lattice matching in heteroepitaxy thin films growth.

The strained lattice mismatch system in Figure 1.10a, which is also called pseudomorphic growth is the main mode of strain engineering in functional epitaxial thin films growth. It reveals the grown film is under tensile or compression stress on substrate without relaxing by generating misfit dislocations. The in-plane strain $\varepsilon_{\parallel}$ is defined as,

$$\varepsilon_{\parallel} = \frac{(a_{f\parallel} - a_f)}{a_f} \tag{1.2}$$

where $\varepsilon_{\parallel}$ is the in-plane lattice constant of the deposited film material and a_f is the lattice constant of bulk material. The strain in the perpendicular direction of the growth films is defined as,

$$\varepsilon_{\pm} = \frac{(a_{f\pm} - a_f)}{a_f} \tag{1.3}$$

The lattice mismatch is evaluated by,

$$f = 2 \times \frac{(a_f - a_s)}{(a_f + a_s)}, \tag{1.4}$$

where a_f and a_s are the unstrained lattice parameters of film and substrate. In pseudomorphic thin film growth, the strains only exist in a certain region before fully

relaxed. Coherent films of perovskite can be grown up to around 100 unit cells (~ 50nm) before relaxing via dislocations. With larger lattice mismatch f>0.7%, domain matching epitaxy will form as shown in Figure 1.11.[74] In this framework, the conventional lattice matching epitaxy becomes a special case where the epitaxial growth of thin films is possible by matching of domains where integral multiples of major lattice planes match across the interface.[75]

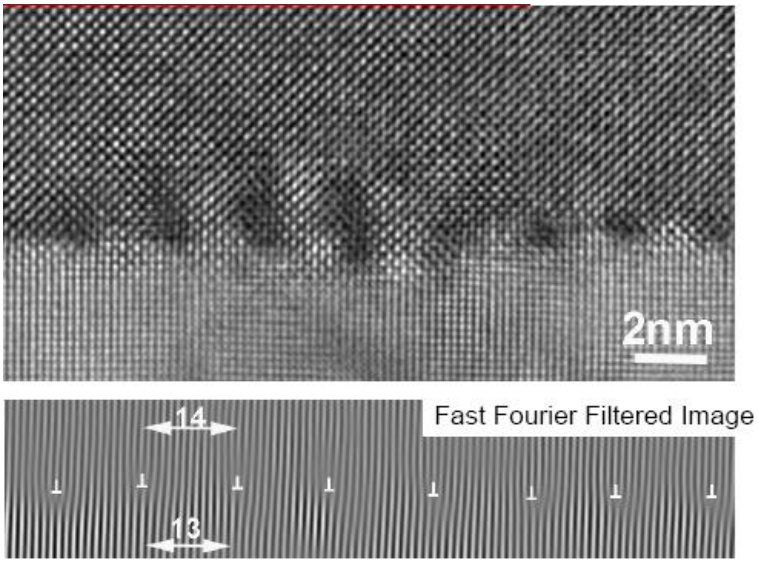

FIG. 1.11. HRTEM and fast Fourier filtered images of domain matching epitaxy $SrTiO_3$ thin film grown on MgO substrate with 14:13 match.

In domain matching epitaxy, misfit dislocations are generated at the interface to fully or partially relax the strain and to achieve an equilibrium structure. The minimum dislocation density is always required in pseudomorphic film to enhance the electronic transport through the heteroepitaxial interface.

One great advantage of epitaxial growth is that the strain in thin films can be manipulated through the selection of appropriate substrates, to engineer the physical properties of the deposited thin films. As Millis *et al.* predicted in their analytical model, the substrate induced biaxial strains (ε_{xx} and ε_{yy}) will carry out strain-induced magnetic anisotropy and affect the magnetotransport properties of epitaxial manganite films.[76] The biaxial strain is defined as,

$$\varepsilon_s = \frac{(a_{\parallel} - a_0)}{a_0}, \qquad (1.5)$$

where a_0 is the lattice parameter of the material in the original cubic state under stress-free conditions and $a_{\parallel}$ is the in-plane lattice parameter of the biaxially strained thin film.[77]

1.3.2 Strain engineering in oxide thin films

Strain engineering provides a powerful and accessible way in manipulating the properties of functional oxide thin films and much work has been done to investigate the influence of strain on the ABO_3 perovskite structures. The general form of ABO_3 perovskite consists cubic sublattices of A and B cations where the B cations

octahedrally coordinated by oxygen anions, as shown in Figure 1.2. It is with Pm3m space group, however many functionalities of the ABO_3 perovskite material are generated by the characteristic distortions of the structure. Figure 1.12 interprets three main structure distortion modes in perovskite including the polar displacement of B cation, rigid rotation of the octahedral BO_6 unit and Jahn-Teller elongation of the BO_6 octahedral.[78,79] These modes compete with each other and the one condenses in the material ground state will play a major role over all. These structure instabilities typically include long-range cooperative displacements of atoms in the crystal, as shown in Figure 1.13. The material properties in ABO_3 perovskites tend to be closely coupled to the energy balance between the intrinsic instable states and the structure distortions in oxide thin films actually help to maintain a lower energy distortion (ground state). Some work has been done and demonstrated that the disabling the distortions will cause higher energy distortions.[80,81]

The understanding of octahedral rotations is very important to investigate the strain effect in magnetic materials. It has been explored that the tensile strain in $LaCoO_3$ magnetic films stabilized the intermediate or high spin states and the lattice distortion will increase the paramagnetic effective moment. [82,83,84]

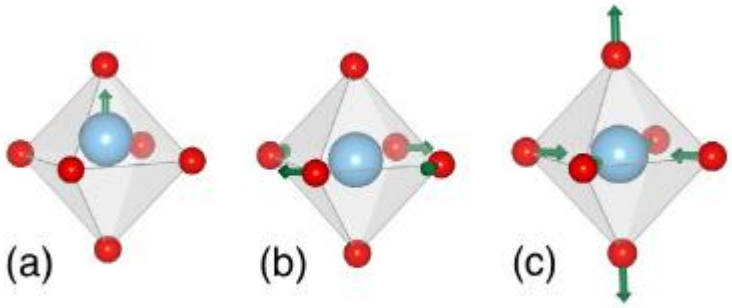

FIG. 1.12. Common perovskite instable modes. (a) Polar displacement of B-site cation; (b) rigid rotation of the BO_6 octahedral, and (c) Jahn-Teller distortion of the BO_6 octahedral.

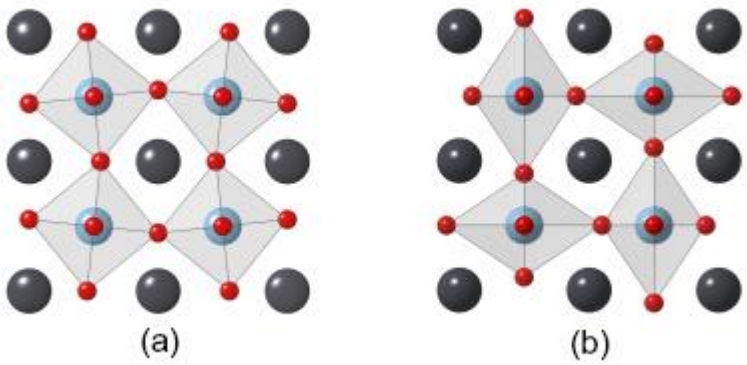

FIG. 1.13. Lattice diagram of (a) the octahedral rotations and (b) the Jahn-Teller distortion. The A cations are shown in black, B cations are shown in blue and oxygen atoms shown in red.

Ferroelectric materials are one of the best systems for analysis in the field of strain engineering. They are characterized by spontaneous polarizations and very sensitive to small values of strain. It has been reported that the strain on the order of 1% can lead to dramatically enhancement of the ordering temperature and coercivities in ferroelectric materials.[85,86,87] Also the bi-axial strain will cause switchable polarizations either parallel or perpendicular to the plane of epitaxy that stabilize the incipient ferroelectric properties in thin films form.[88] Epitaxial strain also plays an important role in multiferroic materials. Dramatic strains have been reported on multiferroic $BiFeO_3$ thin films grown on $LaAlO_3$ and $YAlO_3$ substrates of 5% and 7.5%, respectively. Models simulation on these films suggested a strain-induced metastable phase separated by a low energy barrier from an isosymmetric parent phase.[89] Exciting results have also been found in strained superconductors where strain can be used to increase the critical ordering temperature T_c. $La_{1.9}Sr_{0.1}CuO_4$ superconducting films were grown on different substrates with 0.63% compressive strain and 0.54% tensile strain, respectively. And the first one showed increased T_c and higher metal-insulator transition. It has been also reported that strain can be used to manipulate the band structure of perovskite nickelates to achieve higher T_c.[90]

In the recent decade, material computational simulation techniques have been involved to understand the effects of strain in functional oxide, specially the perovskite oxide thin films. For example, the density functional theory (DFT) has been remarkably successful in predicting and reproducing the properties of a wide variety of materials.[91,92] It is a power tool to investigate the competing instabilities and separate

ionic, electronic and lattice responses of a material to strain. In the computational model, the lattice parameters of a material can be continuous varied and simulation on the influence of strains can be done.

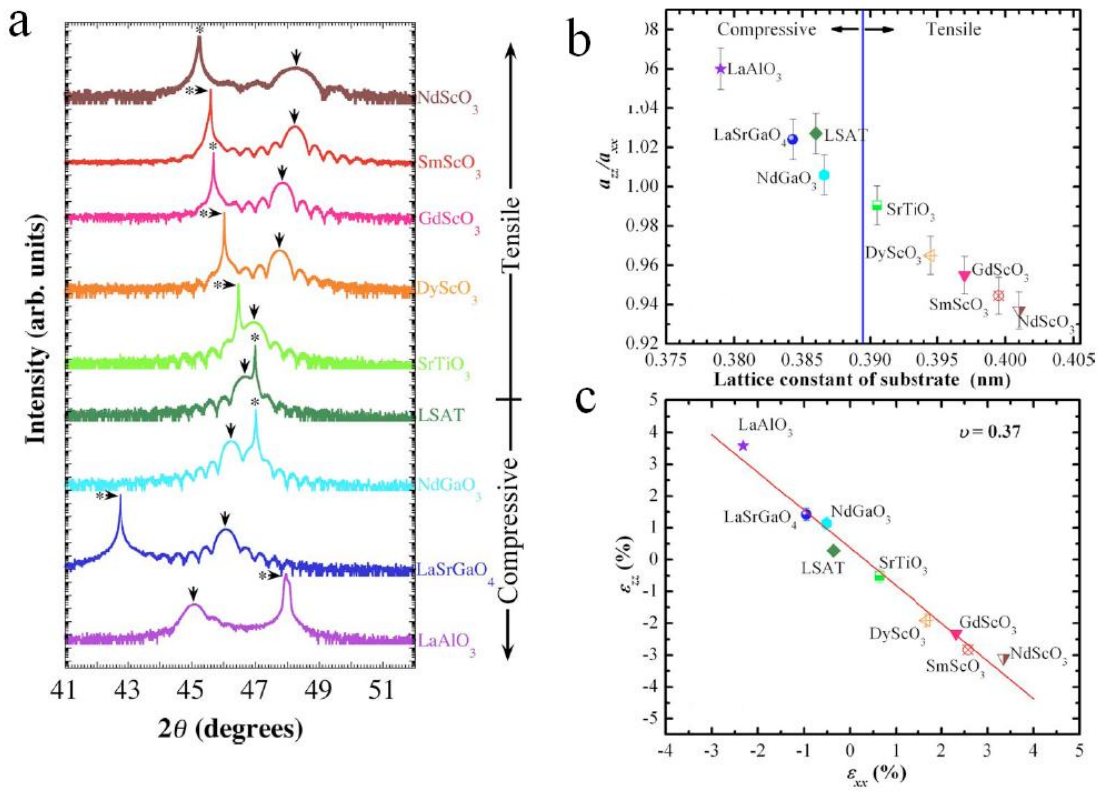

FIG. 1.14. (a) θ -2 θ XRD scans of 22nm thick LSMO films grown on different substrates. (b) The ratio between out-of-plane and in-plane lattice spacing of commensurately LSMO films as a function of the in-plane lattice parameter. (c) The out-of-plane lattice strain as a function of the in-plane lattice strain.

Lehmann *et al.* also reported their work of epitaxial LSMO thin films deposited on STO and $LaAlO_3$ (LAO) substrate by MBE and demonstrated different magnetic behaviors of LSMO films which are only due to different substrates induced strain.[93] More recently, Adamo *et al.* reported their systematical study on biaxial strain on epitaxial (001) LSMO thin films. The films were deposited by MBE on different single crystalline substrates shown in Figure 1.14.[94] The magnetization and electrical transport measurements reveal the dependence of Curie temperature on biaxial strains by varying the substrate-induced biaxial strain from -2.3% to +3.2%. A film-substrate lattice matching diagram has been summarized for ferroelectric perovskite thin films growth which requires chemically and structurally compatible perovskite substrates.[44] Figure 1.15 shows various substrates in the diagram with lattice parameters from 3.70 to 4.0Å.

In recent years, a considerable effort has been spent in developing methods to obtain low defect strained epitaxial heterstructured thin films for industrial applications. Building various buffer layers have been demonstrated to be an effective way to reduce the level of elastic stresses accumulated in the heterostructures during the thin films growth. The buffer layer can help reducing the lattice mismatch at certain thickness while maintaining the crystal structure perfection. However, the residual strain caused by the uncompleted relaxation in the buffer layer can also generate additional defects during subsequent film growth which may extend to threading dislocations to the device region.[95,96]

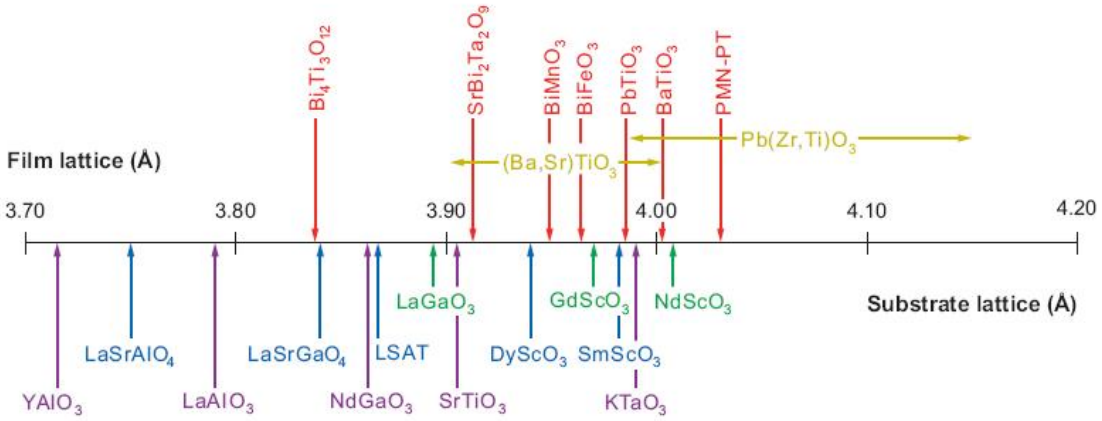

FIG. 1.15. Strain engineering of ferroelectric epitaxial thin film grown on various substrates. The number line shows the pseudocubic or pseudotetragonal a-axis lattice constants of some ferroelectric perovskite and some perovskite-related commercial substrates.

Superlattice is another effective way that can achieve strain control in oxide thin films. It is a periodic structure of layers of two (or more) materials with the thickness of each layer at several nanometers. In superlattice, the in-plane lattice parameter of all the constituents is constrained to that of the underlying substrates and the primary interaction that determines the overall properties of the superlattice is the substrate imposed elastic constraint. Several superlattice systems have been heavily studies recently including $(001)_pPbTiO_3/(001)_pSrTiO_3$ and $(001)_pBaTiO_3/(001)_pSrTiO_3$ superlattices to investigate the effect of strain on thin layers of the ferroelectric

materials as shown in Figure 1.16.[97] In a recently study, Tenne *et al.* reported their growth of $(001)_pBaTiO_3/(001)_pSrTiO_3$ superlattice on $(100)SrTiO_3$ substrate by MBE.[98] The $BaTiO_3$ layer in the superlattice varied from 1 to 8 unit cells in thickness and the $(001)_p$ $SrTiO_3$ spacer layer was fixed to be either 4 or 13 unit cells thick. Both experimental and First-principle calculations work demonstrate a significant increase of the T_c (shown in Figure 1.17) in a multiple-domain state as compared with that in single-domain state by varying the thicknesses of BTO and STO interlayer in the superlattice.[97]

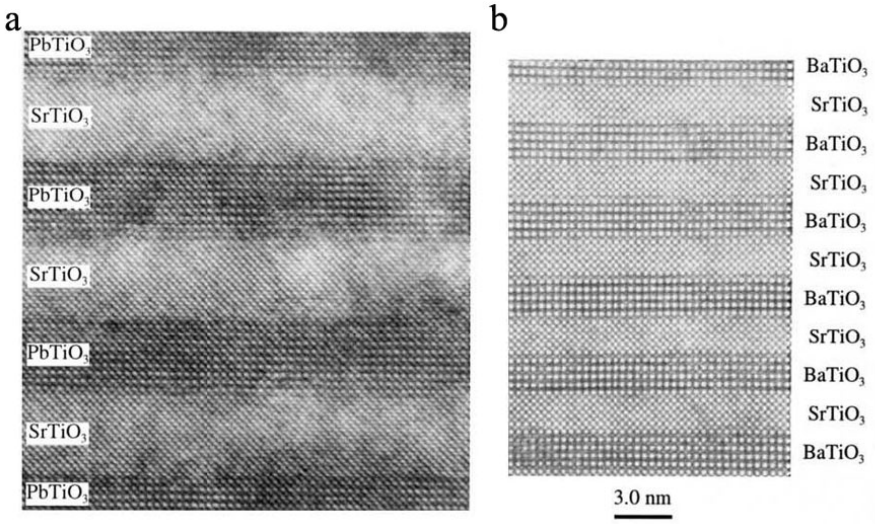

FIG. 1.16. HRTEM images of $PbTiO_3/SrTiO_3$ and $BaTiO_3/SrTiO_3$ superlattices grown by MBE.

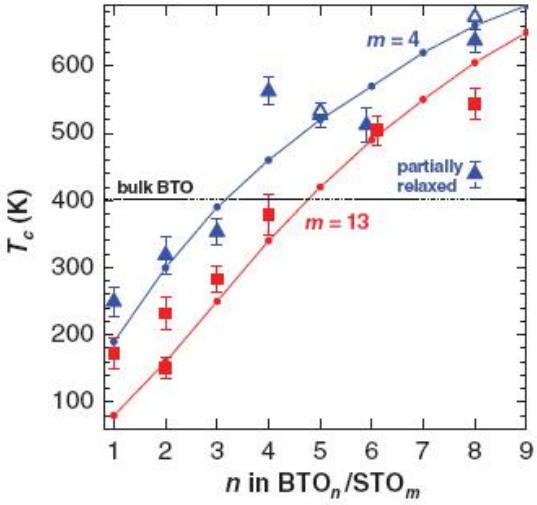

FIG. 1.17. The dependence of T_c on n and m in $(BaTiO_3)_n/(SrTiO_3)_m$ superlattices. The blue symbols are for m=4 and red symbols are for m=13.

The layered heterostructures including buffered layers, multilayers and superlattices are not all the forms of strain controllable oxide thin films. Epitaxial heterostructured nanocomposite thin films in vertically aligned architectures are also being explored recently by pulsed laser deposition. Those include epitaxial pillars of magnetic oxides in a thin film matrix and in-plane checkerboard nanocomposite thin films.[68,99] Most of the heterostructures are being explored in ferroelectric system to enhance the magnetic coupling between ferroelectric and magnetic oxides.

1.4 Vertically aligned nanocomposite (VAN) thin films

1.4.1 Current research overview

VAN thin films are a novel thin film architecture where two phases are self-assembled heteroepitaxially grown on given substrate and form a nano-checkerboard structure in-plane. Both phases in VAN thin films grow alternatively as columns with lattice matching next to each other (out-of-plane, vertical grain boundaries) and on substrate (in-plane, film-substrate interface. The column width is around 20~50nm and the VAN film thickness can reach up to several um. Figure 1.18 shows a schematic diagram of a standard VAN thin film and $BiFeO_3$:Sm_2O_3 VAN thin film.[100]

VAN thin film systems exhibit many interesting physical properties because of its unique microstructure. There are two types of strains in VAN thin films: the substrate induced horizontal strain on the film-substrate interface and the interfacial strain along the vertical phases interface. In VAN thin films, the strain can be controlled by the higher-modulus phase and maintained throughout much thicker epitaxial films (>500nm). The VAN thin films are also interesting to achieve multifunctionalities and have the potential to enhance a single functionality through manipulating the strain in one of the phase by another. It is a smart system that can control or improve material functionalities at nano-scale in thin films with existing processing techniques. The VAN thin films can also be a promising template for developing various nanostructures such as nanoporoes, nanowires, nanorods and ultra high density nanocapacitor

arrays.[101,102,103] However, the VAN growth mechanism is not yet clear and the current VAN structures are limited to oxides.

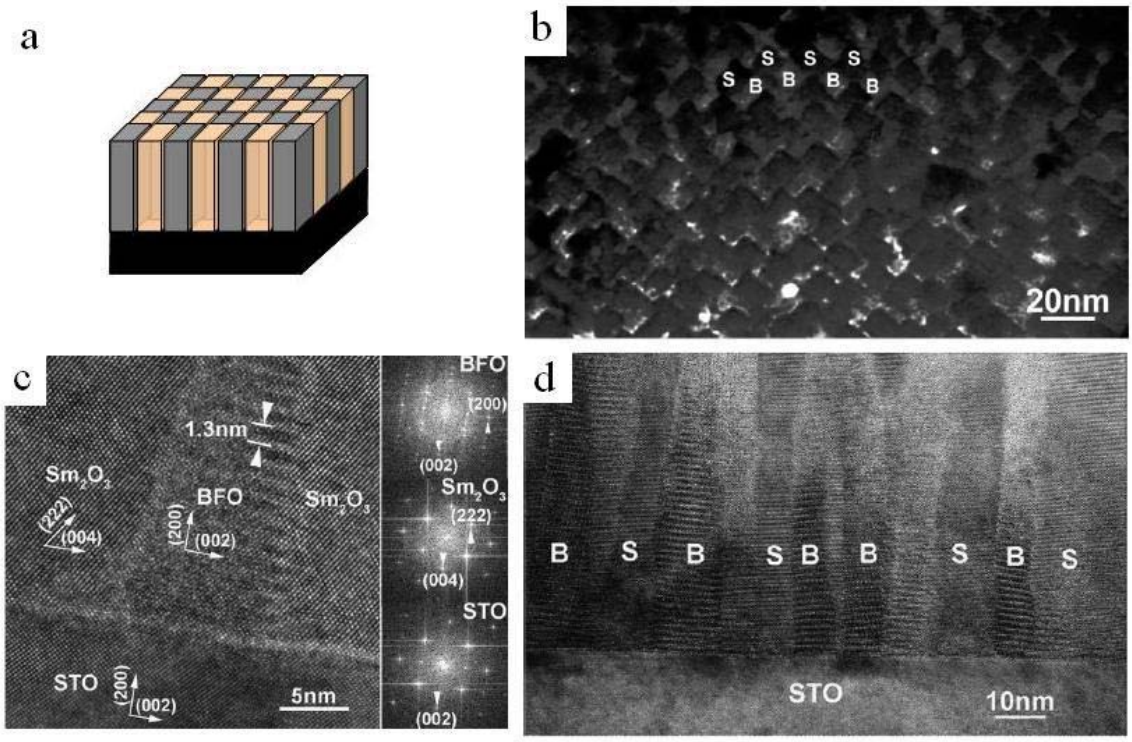

FIG. 1.18. (a)Schematic diagram of a standard vertically aligned nanocomposite thin films; (b)plan-view TEM image of $BiFeO_3$:Sm_2O_3 VAN thin film; (c) high resolution TEM image shows clearly volumnar structure and lattice matching between phases; (d) cross-section TEM image of $BiFeO_3$:Sm_2O_3 VAN thin film shows alternatively aligned columnar growth of both phases.

Much work has been done on self-assembly co-growth of organic system such as copolymers and metal alloys such as Co-Pt alloys in the past decades.[104,105] Desired microstructures can be achieved in those systems by a careful tuning on the thermodynamic parameters to control the overall energy in the systems. However, the investigation on self-assembly of inorganic structures, for example, vertically aligned nanocomposite metal-oxides just started several years ago.[36] Combining metal-oxides in VAN system will lead a range of new interface-coupled thin film functionalities and more experimental and theoretical understandings of VAN are coming with the developments of multiferroics study as well as the materials magnetotransport investigations include colossal magnetoresistance (CMR) and low field magnetoresistance (LFMR).

The first well established VAN system is $La_{0.67}Ca_{0.33}MnO_3$:MgO (LCMO:MgO) thin films by Lebedev *et al.* in 2002.[36] The VAN thin films were grown by a solution based technique called metal-organic aerosol deposition (MAD) and the initial objectives are to demonstrate the phase transition and tunable magnetotranport properties in the LCMO phase. Later, magnetostrictive spinel $CoFe_2O_4$ nanopillars embedded randomly in a piezoelectric $BaTiO_3$ matrix were demonstrated by pulsed laser deposition (PLD).[68] Till now, more other VAN systems have been developed to achieve tunable material functionalities or better physical properties. Table 1.3 gives a summary of developed VAN systems with different crystal structures and deposition methods.

Table 1.3. Diverse VAN systems developed by various deposition methods.

VAN system	Crystal structure	Film grown method	Reference
$La_{0.7}Ca_{0.3}MnO_3$:MgO	Perovsite-Rocksalt	MOAD	36
$La_{0.7}Sr_{0.3}MnO_3$:MgO	Perovsite-Rocksalt	MOAD, PLD	106,107
$BaTiO_3$:$CoFe_2O_4$	Perovsite-Spinel	PLD	68,108
$BiFeO_3$:$CoFe_2O_4$	Perovsite-Spinel	PLD	109
$PbTiO_3$:$CoFe_2O_4$	Perovsite-Spinel	PLD	70,110
$Pb(Zr,Ti)O_3$:$CoFe_2O_4$	Perovsite-Spinel	PLD	111
$Pb(Zr,Ti)O_3$:$NiFe_2O_4$	Perovsite-Spinel	PLD	112
$BaTiO_3$:$NiFe_2O_4$	Perovsite-Spinel	PAD	113
$BiFeO_3$:Sm_2O_3	Perovsite-Rocksalt	PLD	114
$BaTiO_3$:Sm_2O_3	Perovsite-Rocksalt	PLD	115
$La_{0.7}Sr_{0.3}MnO_3$:ZnO	Perovskite-Wurzite	PLD	100,37
$La_{0.7}Sr_{0.3}MnO_3$:Mn_3O_4	Perovsite-Spinel	PLD	38

Most of the candidates materials as we can find from above table are include perovskites and second oxide compounds. Perovskite materials are a branch of outstanding metal-oxides and rich in magnetism, ferroelectric and multiferroics. The VAN thin films can be grown by solution based technique MAD as well as physical vapor deposition mainly in pulsed laser deposition (PLD). PLD usually provide a good stoichiometry between the targets and deposited thin films and with higher film growth rate. In general, there are several rules need to be taken considerations to growth well-order VAN architectured thin films: (a) the chosen phases should both epitaxial grown on the given substrate; (b) the growth kinetics of both phases should be similar that they can both grow with sufficient crystallinity in parallel; (c) the cations of both

phases should with sufficient differences of ionic radii to minimize the intermixing of two phases; (d) it is preferred to have two phases with different elastic constants that they can build effective strain control of one phase by another; (e) the two phases are preferred to be the most thermaldynamic stabled at certain growth condition that they can be easily grown and without obvious phases contamination.[100]

1.4.2 The growth of VAN architecture

The concept of spontaneous nanostructure formations has been extensively studied in metals and semiconductor systems.[116,117,118,119] Much research has been conducted on the self-organization of nanostructures on semiconductor surfaces through epitaxial growth. However, the mechanism of in-plane self-assembly grown is not yet clear and it is still a challenge to synthesize nanostructures in complex oxides.

The growth of heteroepitaxial VAN thin films does not obey classical thin film growth modes. There are three major thin films growth modes: (1) Volmer-Weber or island growth, (2) Frank-Van der Merwe or layer-by-layer growth, and (3) Stranski-Krastanov growth.[4] The first island growth demonstrates a case that atoms or molecules nucleate on substrate and grow in three dimensional as islands. This mode can explain stronger bonding between deposited atoms as compared with those to the substrate. The second layer-by-layer growth mode reveals a two dimensions planar growth of adatoms with the smallest nucleus. In this mode, the deposited atoms are more strongly bonded to the substrate than to each other. A typical example of layer-

by-layer growth is the epitaxial growth of oxide thin films. The last mode is a combination of the layer-by-layer and island growth. In this mode, islands will begin to occur after forming one or several monolayers in a layer-by-layer growth. This growth is very common due to the energetically instability during the film growth.

Actually the growth modes of single phase heteroepitaxial thin films can be also described with thermodynamic models for the nucleation process. That will involve the discussion on surface energies of materials and droplet theory of nucleation. Figure 1.19 shows a model that describes the atomistic nucleation process of adatoms on substrate surface during a vapor deposition process.[5] The equilibrium among the horizontal components of the interfacial tensions between the constitutive phases yields Young's equation:

$$\gamma_{sv} = \gamma_{fs} + \gamma_{fv} \cos\theta \qquad (1.6)$$

where γ represents the interfacial energy, subscripts s, f, and v stand for substrate, film and vapor respectively, θ is the wetting angle. The Young's equation can better distinguish between three different growth modes. For island growth, $\theta > 0$ and it suggests the island growth occurs only the surface tension of the film exceeds that of the substrate. In layer-by-layer growth, the film wets the substrate and so $\theta = 0$. The heteroepitaxial growth of oxide thin films requires a layer-by-layer growth with similar film and substrate surface energy. It should be pointed out that the nucleation during oxide thin film growth can occur in many ways including step edges, defects etc. The growth of nucleus can also vary after the critical nucleus size been reached.

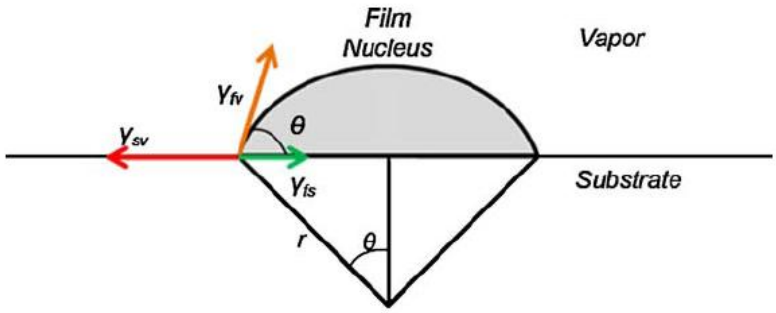

FIG. 1.19. Schematic diagram of the atomistic nucleation process during a vapor deposition process.

A basic schematic diagram flow of the vertically aligned nanocomposite thin films growth is shown in Figure 1.20. The growth of VAN thin film mainly involves two stages, the clusters nucleation and film growth. At the very early stage of composite film growth, different adatoms will arrive at the substrate surface in parallel. Same phase molecules will accumulate since they have same surface energy and nucleate to minimum the total system free energy. For the phases which with similar lattice parameters to the substrate will grow as layer-by-layer mode. Multiple phases will either get in contact and form the initial monolayer on substrate or nucleate as islands first and then grown as continued layers. The phase column widths are determined by the adatoms diffusion as a competition on the substrates. The following film growth will perform as heteroepitaxial mode and same phase adatoms will locate on the same column region of the bottom layer defined by the energy minima and to reduce the

lattice mismatch.[120] Functional properties of VAN thin films are in deep related to the microstructures which could be enormously various due to different material properties and film growth conditions. As shown in Figure 1.20, the in-plane nano-checkerboard architecture is not the only format that exists in the VAN thin films.

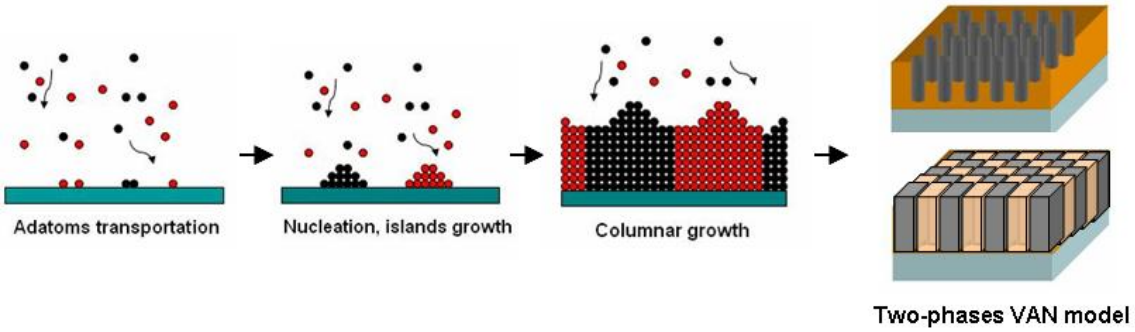

FIG. 1.20. Schematic diagrams flow of the vertically aligned nanocomposite thin films growth.

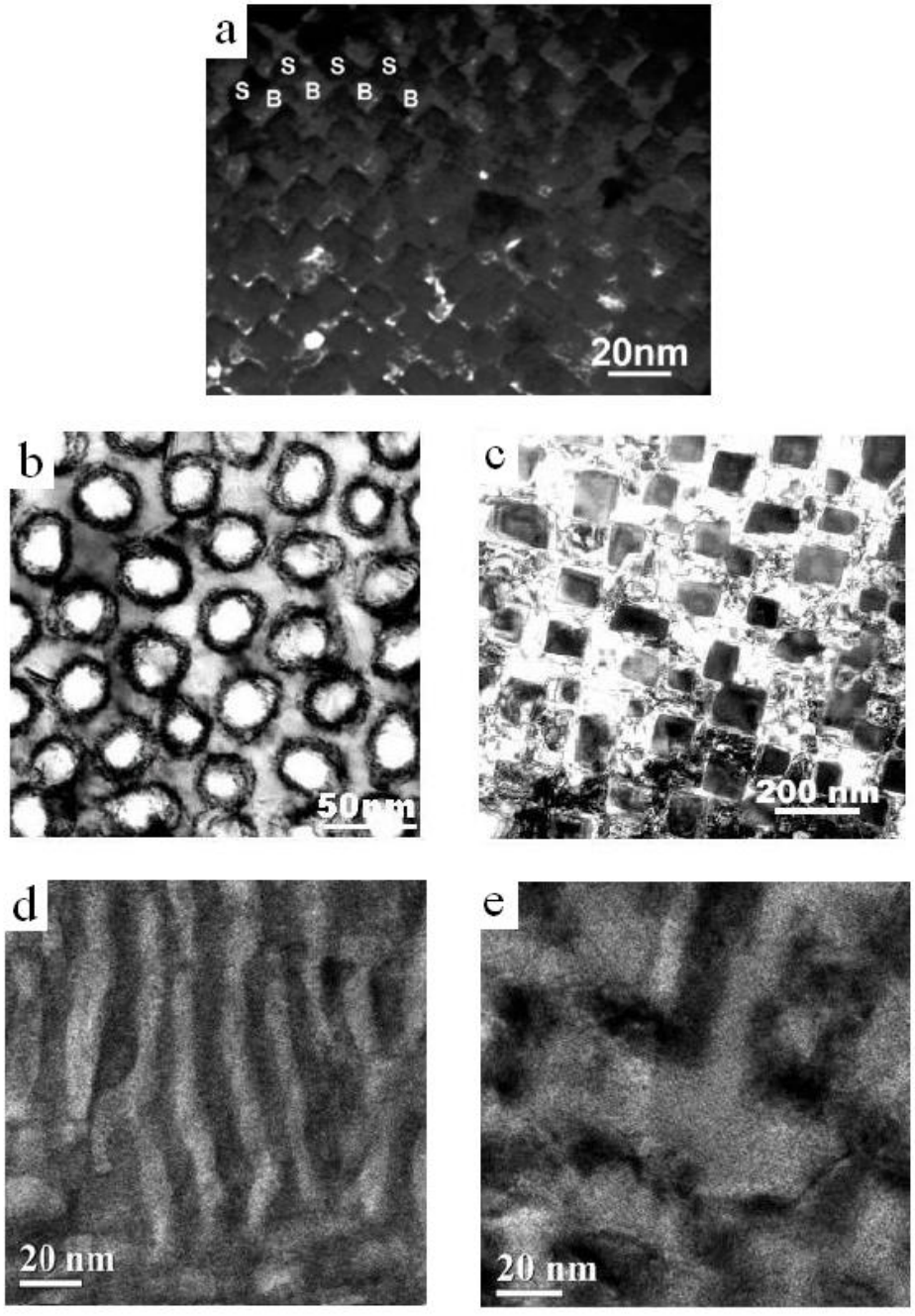

FIG. 1.21. Plan-view TEM images of VAN thin films with various architectures. (a) Checkerboard structure; (b) circular nanopillar structure; (c) rectangular nanopillar structure; (d) domain walls structure and (e) biaxial domain structure.

Figure 1.21 compares different in-plane architectures in VAN thin films. A perfect checkerboard morphology needs very carefully experimental control and only for specific systems.[121] As a matter of fact, a more general case in VAN growth is the doped nanopillars formed in continued thin film matrix and that can be identified as VAN-derived structure. Either circular, rectangular or T shape columns can be formed in VAN films depending on the strain relaxation and the various phase nucleation mechanisms. Another interesting architecture in VAN thin films is the biaxial domain walls structure which requires two phases have competitive growth kinetics and a specific film composition.

1.4.3 Strain control in VAN thin films

The vertically aligned heteroepitaxial growth of multiple phases in VAN thin films provides novel ways of engineering the strain in functional oxide materials. Overall, there are two types of strain in VAN thin films: the substrate induced horizontal strain on the film-substrate interface and the vertical interfacial strain along the phase boundaries. Figure 1.22 shows two different strain controls in $BiFeO_3$:Sm_2O_3 (BFO:SmO) VAN thin films. BFO is a distorted rhombohedral perovskite, it can easily epitaxially grow on STO (001) substrate with similar lattice parameter (a=3.96Å) as that of the STO substrate (a=3.91Å) (shown in Figure 1.22a).

The second phase SmO is a typical rare earth (RE) oxide with cubic crystal structure, and epitaxial growth can be achieved after 45° in-plane rotation of SmO crystals on STO substrates as shown in Figure 1.22b. In a pure epitaxial film, the phase is simply strained to the isostructural substrate. The substrate stain control is quite similar to epitaxial pure film growth with film thickness less than 100nm. In substrate strain control, the BFO phase will maintain compression in-plane and tension out-of-plane, and the SmO phase will maintain tension in-plane and tension out-of-plane, respectively. This estimation is based on epitaxial film-substrate lattice matching and Poisson's effect. The vertical interfacial strain control is an opposite status where vertical lattice matching on the phases/columnar interface plays a dominant role overall. BFO phase will maintain tension in-plane and compression out-of-plane, and SmO phase will maintain compression in-plane and tension out-of-plane.

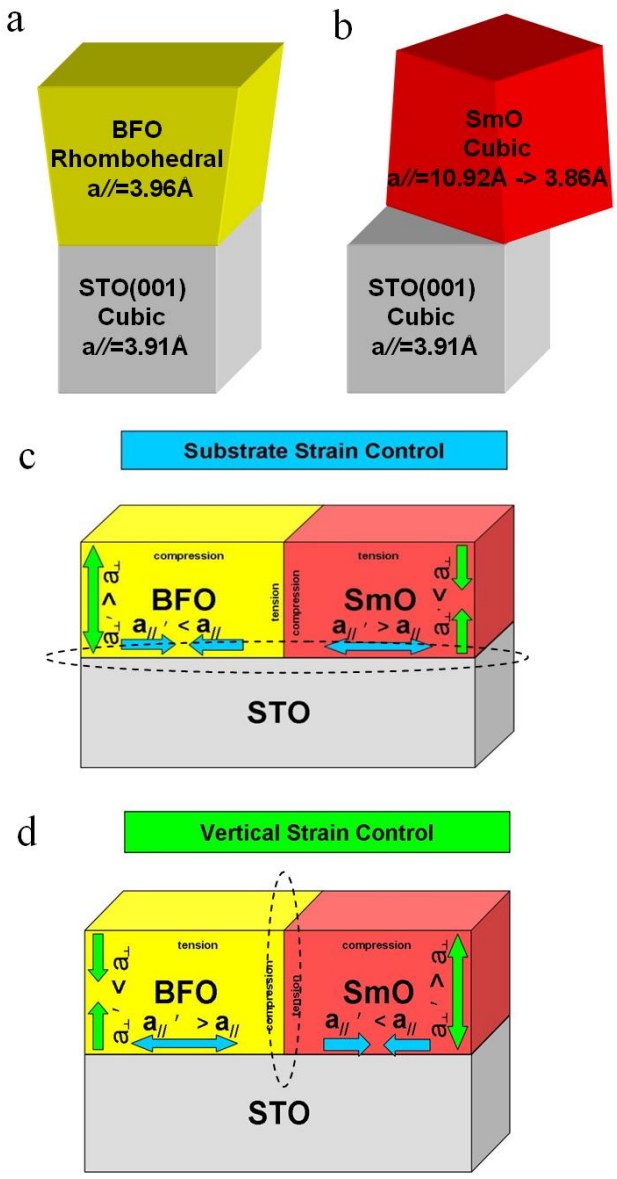

FIG. 1.22. Schematic diagrams of strain control in $BiFeO_3$:Sm_2O_3 VAN thin films. (a) Lattice matching of $BiFeO_3$ on $SrTiO_3$ (001)substrate; (b) lattice matching of Sm_2O_3 on $SrTiO_3$ (001)substrate; (c) the horizontal substrate strain control in BFO:SmO thin films; (d) the vertical interfacial strain control in BFO:SmO thin films.

The vertically aligned nanocomposite thin film systems have enormous potential to control the vertical interfacial strain in much thicker films with its correspondingly large volume. In VAN thin films, the vertical column width are relative small (10~50nm) that the substrate induced strain can not fully relax. The strain in the lower-modulus phase is controlled by that in the higher-modulus phase which mainly caused by the vertical strain and the strain can be maintained throughout much thicker epitaxial films (>500nm). It is the interfacial lattice matching further more the competition of those two strains that made the VAN thin films so interesting to achieve multifunctionalities and have the potential to enhance a single functionality through manipulating the strain in one of the phase by another.

Strain in VAN thin films exist not only on the substrate/film interface due to epitaxy film growth, but also the vertical interfacial phase boundaries with lattice matching between phases. Electron microscopy analysis demonstrated the lattice matching in $BiFeO_3$:$NiFe_2O_4$ VAN thin films as shown in Figure 1.23.[122] The 5% lattice mismatch can relax on the vertical interface given from both cross-section and plan-view orientations. High resolution TEM image also reveals the structural continuity occurs across the vertical phase interface. To reduce the interface energy, a structure continuity was maximized from the [Ni,Fe]O_2 layer to $BiFeO_3$.

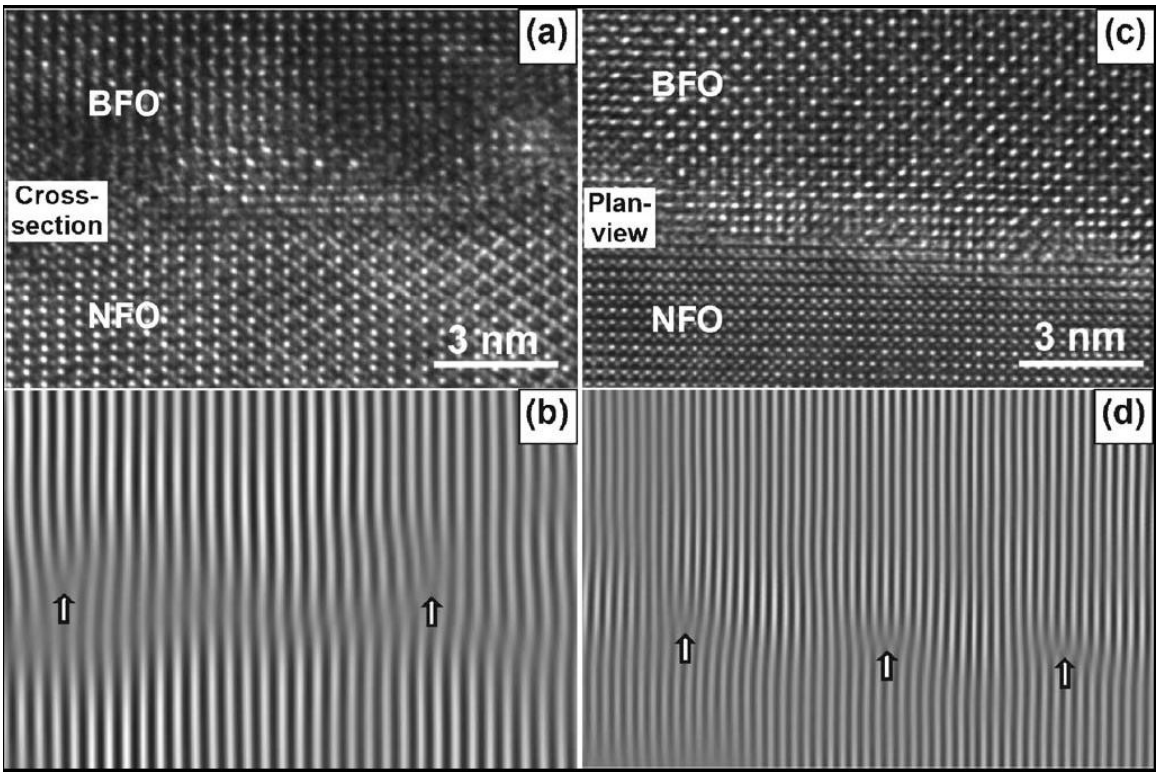

FIG. 1.23. High resolution TEM images of $BiFeO_3$-$NiFe_2O_4$ interface with zone axis along (a) [110] cross-section orientation and (c) (001) plan-view orientation. (b) and (d) are the corresponding Fourier filtered images that reveal the lattice mismatch.

1.4.4 Novel physical properties in VAN thin films

VAN thin film systems exhibit many interesting physical properties because of its unique microstructure. Those novel physical properties including multiferroics and

exchange bias are based on the specific strain control in VAN architectures and the interface effects in between vertical phase columns.

1.4.4.1 Multiferroics in VAN thin films

Multiferroics refers to a class of materials which maintain ferroelectricity, ferromagnetism and ferroelasticity simultaneously. The multiferroic materials exhibit both polarizations and magnetizations with external electric field and magnetic field, respectively. In multiferroic materials, the magnetic ordering is governed by the exchange interaction of the electron spins and the ferroelectric ordering is governed by the redistribution of charge density in the lattice.

The architecture of vertically aligned nanocomposite can be implemented to achieve simultaneous ferroelectric and ferromagnetic properties.[123,124,125] VAN thin films can be grown as consisting of ferroelectric phase and ferromagnetic phase while have good phase separation and lattice matching. The coupling between the two ordering parameters is though the stress mediation. For example, a magnetic field will induce a distortion of the magnetostrictive phase, which in turn distorts the piezoelectric phase in which the electric field will be generated. The composite could be considered as a new multiferroic material. There are several advantages of multiferroic composites over the single phase multiferroics.[121] First of all, the physical properties of the composite materials can be adjusted by the selection of different constituent phases as well as the volume ratio to meet specific applications. Second, a

higher magnetoelectric coupling can be achieved as compared to that of single phase multiferroics.

VAN multiferroic materials in thin film form offer a broadway to achieve high material quality and to investigate the structure-property relationships. Zheng *et al.* reported their initial work on creating VAN thin films consisting of $CoFe_2O_4$ pillars embedded in $BaTiO_3$ matrix as shown in Figure 1.24.[68] There is a large difference in lattice parameter between those two phases that leads to the formation of pillars with column width around tens of nm. This VAN system consists of ferroelectric $BaTiO_3$ phase and ferromagnetic $CoFe_2O_4$ phase, and the magnetoelectric coupling effect is through the stress mediation. In addition, the substrate clamping is largely reduced and it exhibits strong magnetoelectric coupling between the phases due to a high interface-to-volume ratio. The temperature dependent magnetic measurements illustrate the coupling between the two ordering parameters, which is manifested as a change in magnetization at Curie temperature.

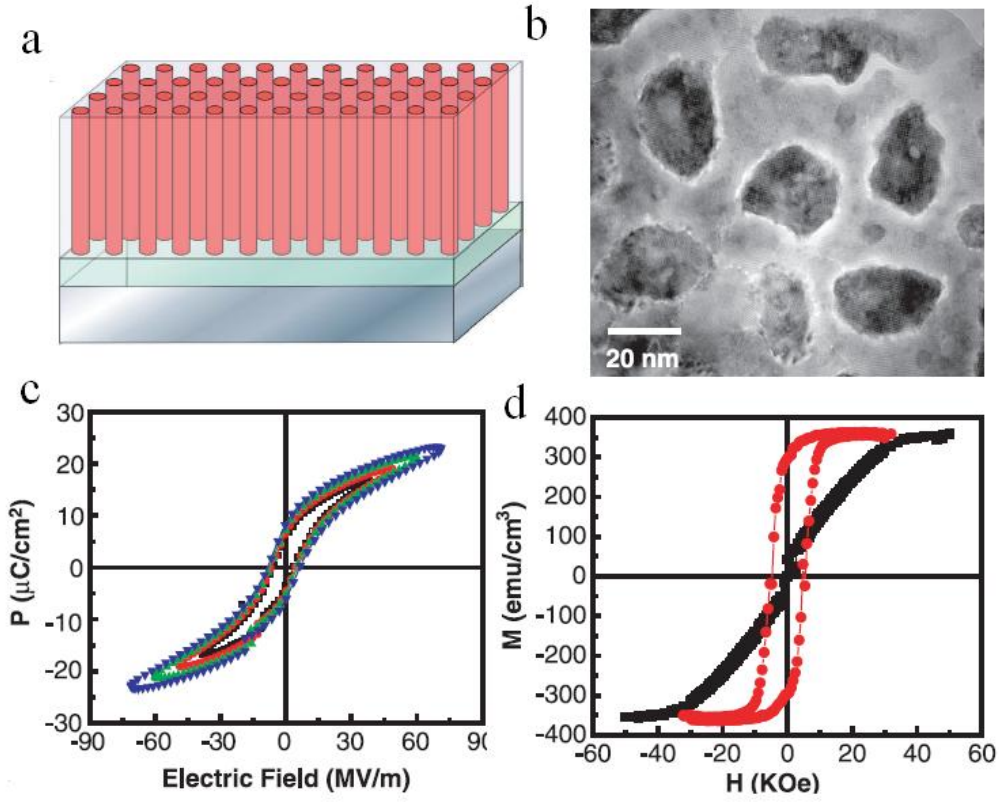

FIG. 1.24. (a) Schematic illustration of a vertically aligned nanocomposite $BaTiO_3$:$CoFe_2O_4$ thin film. (b) TEM planar view image shows the $CoFe_2O_4$ nanopillars in the $BaTiO_3$ matrix. (c) and (d) show a simultaneous ferroelectric and ferromagnetism in $BaTiO_3$:$CoFe_2O_4$ VAN thin film.

Following research work has been conducted on several other perovskite-spinel systems. Novel multiferroic VAN systems with conbination of a number of perovskite (eg. $BaTiO_3$, $PbTiO_3$ and $BiFeO_3$)[69,126,122] and spinel (eg. $CoFe_2O_4$, $NiFe_2O_4$, and Fe_2O_3)[71,122,127] structures have been investigated. Zavaliche *et al.* reported $\Delta E/\Delta H=100$

V/cm Oe at room temperature in a $BiFeO_3$:$CoFe_2O_4$ VAN thin film.[128] The magnetic force microscopy scans the samples before and after electric field poling and shows a significant number of CFO pillars switch their magnetic state from a downward direction to an upward direction under applied electric field.[129] The VAN architecture has also been demonstrated to be very versatile and offer an excellent opportunity for electrically controlled magnetic storage.

1.4.4.2 Exchange bias in VAN thin films

Exchange bias usually occurs in bilayers or multilayers of magnetic materials where the hard magnetization behavior of an antiferromagnetic thin film causes a shift in the soft magnetization curve of a ferromagnetic film. This phenomenon is of tremendous utility in magnetic recording, where it is used to pin the state of readback heads of hard disk drives at exactly the point of maximum sensitivity, as called bias.

The basic physics of exchange bias is the exchange interaction between the antiferromagnet and ferromagnet at the interface as shown in Figure 1.25. Since antiferromagnets have a small or no net magnetization, their spin orientation is only weakly influenced by an externally applied magnetic field. A soft ferromagnetic film which is strongly exchange-coupled to the antiferromagnet will have its interfacial spins pinned.[130] Reversal of the ferromagnet's moment will have an added energetic cost corresponding to the energy necessary to create a Néel domain wall within the ferromagnetic film.[131] The added energy term implies a shift in the switching field of

the ferromagnet. Thus the magnetization curve of an exchange-biased ferromagnetic film looks like that of the normal ferromagnet except that is shifted away from the H=0 axis by an amount H_b.

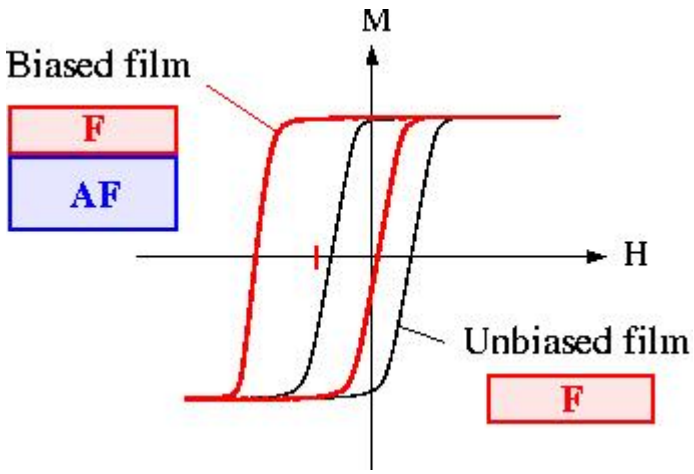

FIG. 1.25. Schematics illustrating that the exchange bias occurs at the interface between the antiferromagnet and ferromagnet phases.

Exchange bias can be achieved by coupling an antiferromagnetic (AFM) phase with a ferromagnetic phase. This effect has been shown in many bi-layer systems, and also in particulate composites, but never in vertical structures. Vertical aligned nanocomposite thin films are of increasing interests to offer significant advances for

applications such as exchange bias and related strain control. To achieve exchange bias the ratio of interfacial area to the volume of the FM phase must be as high as possible. For a bi-layer structure, this means that there is a limit to the film thickness – typically around 10-30nm. For a vertical composite the interfacial area increases with the thickness, so the limit does not apply and the key dimension will be the column width. Figure 1.26a compared the typical design of a bi-layer composite for exchange bias with the design of the equivalent vertical composite.

Exchange bias has been reported in $BiFeO_3$:Fe_3O_4 VAN films with careful control of both the constituent phases and the microstructure of the composite.[132,99] Films of 10% Fe_3O_4 – 90% BFO VAN thin films were grown under optimum deposition conditions, as shown in Figure 1.26b and c. Exchange bias was set by field cooling from 680 K with an out-of-plane field of 10 kOe. Figure 1.26d shows room temperature magnetic measurements, with the field applied in the out-of-plane direction. A shift of the hysteresis loop is clearly visible, with an exchange field H_{ex} of 60 Oe. This is the first ever example of exchange bias in a vertical nanocomposite.

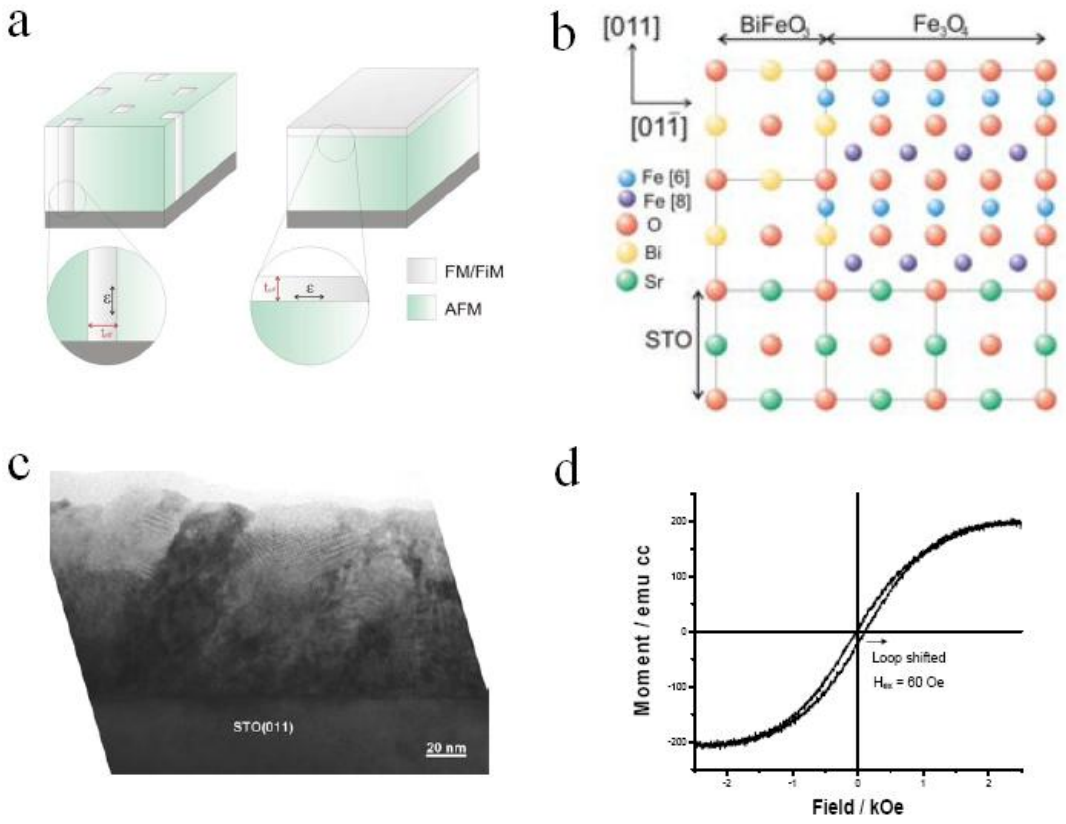

FIG. 1.26. (a) Geometries for exchange bias in vertical composites and bi-layers; (b) simulated lattice matching of BFO-Fe_3O_4 heteroepitaxial growth; (c) cross-section TEM micrograph shows columnar growth of alternatively ordered phases; (d) room temperature magnetic measurements taken at room temperature shows an exchange field of 60 Oe.

1.5 Material engineering in VAN oxide thin films

1.5.1 Structure control of VAN architecture

To grow high quality VAN thin films, the deposition process need to be carefully controlled and several points need to be considered.[121] First is to obtain high quality epitaxial two-phase structure while maintaining the chemical stoichiometry of both phases and eliminating the impurity phases. The second is to achieve clear sharp interfaces between the phases and avoid any inter-diffusion. In the $BiFeO_3$:Sm_2O_3 VAN thin films, it has a quaternary Bi-Fe-Sm-O system and many possible phases including $BiFeO_3$, Bi_2O_3, α-Fe_2O_3, γ-Fe_2O_3 and Sm_2O_3 could be formed during film growth. It has been reported that by varying the deposition oxygen pressure, the dominant phase formed in the nanocomposite thin films continuously changes from ferroelectric $BiFeO_3$ to a mixture of α -Fe_2O_3 and ferromagnetic γ -Fe_2O_3.[127] The parasitic phases will affect further the magnetic and electrical properties of the films. The unidirectional solidification process during the film growth requires high temperature and a critical control over the composition and unexpected third phases, to obtain regular eutectic phases/structures under steady state conditions.

Different growth kinetics will lead to various microstructures and further tune the physical performance of VAN thin films. In the growth of oxide thin films, material kinetics can be affected by growth temperature, deposition rate and molecular surface diffusion. Zheng have studied the growth of $BaTiO_3$:$CoFe_2O_4$ VAN thin films under different growth conditions.[121] Figure 1.27 shows that the column width of $CoFe_2O_4$

nanopillars increases systematically as the growth temperature increases and a higher film growth rate will decrease the phase crystallinity. Also the phase separation is directed by surface diffusion which is the main contribution in the formation of $BaTiO_3$:$CoFe_2O_4$ VAN thin films. It was also concluded that the antiphase domain boundaries (ADBs) provide both nucleation sites and diffusion paths for the growth of multiphases in VAN thin films. ADB is the boundary that separates two domains and it usually results from lattice distortion, low growth temperature and high growth rate. ADBs are in general non-equilibrium state and have a positive excess free energy. They can migrate to reduce the total amount of boundaries through a thermodynamic driving force.

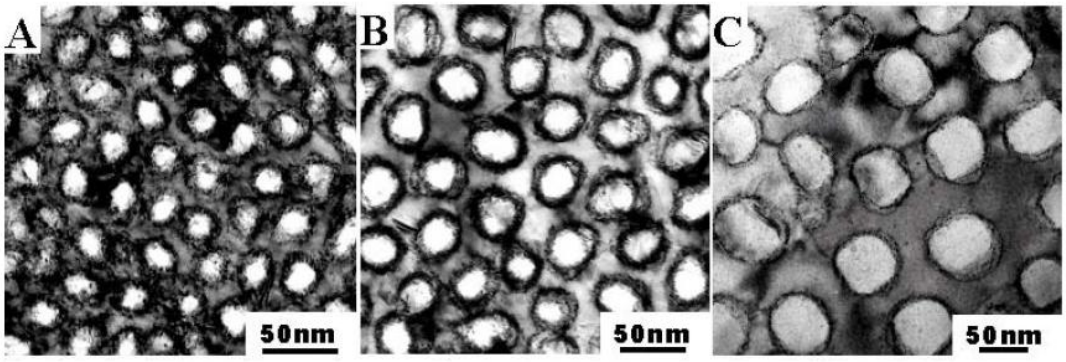

FIG. 1.27. Plan-view TEM images of BTO-CFO nanocomposite thin films. The CFO pillars were doped in BTO continued film matrix and its column width increases as increasing the deposition temperature from (a) 850°C to (b) 900°C and (c) 950°C.

The surface morphology of VAN thin films is highly related to the nucleation of deposited adatoms on a given substrate. That can be affected by several energy terms including the substrate surface energy, interface energy and surface energy of the crystalline phase. A systematic study has been conducted on $BiFeO_3$:$CoFe_2O_4$ VAN thin films on different oriented $SrTiO_3$ substrates.[109] Most perovskite phases including $BiFeO_3$ have the lowest energy surfaces of {001} surfaces with a corresponding equilibrium shape cube with six {100} facets. The second phase $CoFe_2O_4$ is characterized by the lowest surface energy of {111} surfaces and an equilibrium shape of octahedron with right {111} facets. The Winterbottom construction theory has been used to build the possible configuration of crystalline nucleus on the substrates with different surface energies.[133] When the $SrTiO_3$ substrate orientation is parallel to the lowest energy surface of either phase, one phase will form continued epitaxial film matrix by the definition of energy minima and the other phase will form doped nanopillars. With the case of the substrate orientation is not parallel to either phase, both BFO and CFO will have competition of wetting configurations with island growth modes. Figure 1.28 shows different surface morphologies of BFO:CFO nanocomposite thin films grown on $SrTiO_3$ substrates with various orientations.[109] It reveals that the large difference in the surface energy anisotropy of the multiple phases results in the different nucleation modes on the substrate. With paralleled substrate orientation, the wetting phase will form a continued film matrix which covers a larger area of the substrate and with the other phase form islands at the initial nucleation stage. With unparalleled substrate orientation, the wetting conditions of both phases as well as the

area fraction/nucleation sites will be similar. The columnar structure and column widths are established at the initial stage of composite film growth and there is no distinct change of microstructures within the film thickness.

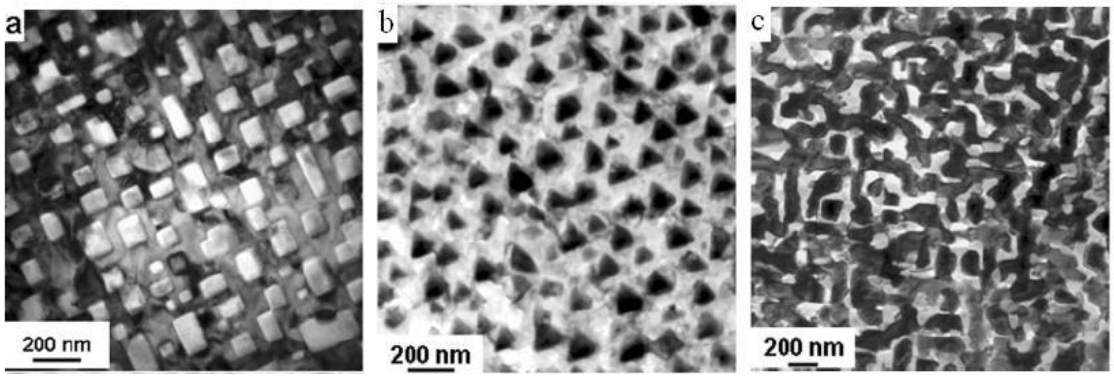

FIG. 1.28. TEM plan-view micrographs of $BiFeO_3$:$CoFe_2O_4$ VAN thin films grown on $SrTiO_3$ substrates with (a) (001), (b) (111) and (c) (110) orientations.

It is interesting to see the volume fraction of two phases does not change the mode of the VAN thin films growth in BFO-CFO system. However, that is not true in the $BiFeO_3$:Sm_2O_3 VAN thin film system. Figure 1.29 shows the BFO:SmO nanocomposite thin films grown on $SrTiO_3$ (001) substrates with different film compositions. It is clearly to see a dramatic morphology change as a function of film compositions. With the same molar ration of two phases, SmO grow as nanopillars

doped in continued BFO thin film matrix. While adjusting the mole ratio of BFO:SmO to 60%:40%, both phase shows strong biaxial domain wall shape growth. The nucleus/island growth prefers to go along the (100) and (010) substrate strain directions in-plane. With more BFO composition in the film as 75%:25%, SmO phase grows as T shape columns doped in the BFO continued film matrix. This plotting reveals that the anisotropic surface energy is not always the first priority concern for a steady-state growth of the multicomponent nanostructures. The volume ratio drived biaxial strain may also affect the microstructure of VAN thin films.

The microstructure of the embedded columns related to the balance of the relative interfacial and elastic strain energies.[134] The microfaceting presented in the cylindrical shape pillars has much finer scale and smaller dimension.[135] A smaller and cylindrical pillar can minimize the surface energy and highly faceted rectangular pillars minimize the elastic strain energy. The $BaTiO_3$:$CoFe_2O_4$ and $BiFeO_3$:$CoFe_2O_4$ nanocomposite thin films show a minor microstructure variation on the doped CFO nanopillars. As shown in Figure 1.30, CFO nucleates as cylindrical rather than rectangular in BTO and BFO matrix, respectively.[121] As compared with the lattice parameter of $CoFe_2O_4$ (a/2=4.13Å), $BiFeO_3$ (a=3.93Å) has a larger lattice misfit than that of the $BaTiO_3$ (a=4.00Å) film matrix. This can explain the more faceted islands of $CoFe_2O_4$ column in $BaTiO_3$ because there is more strain energy need to be accommodated.

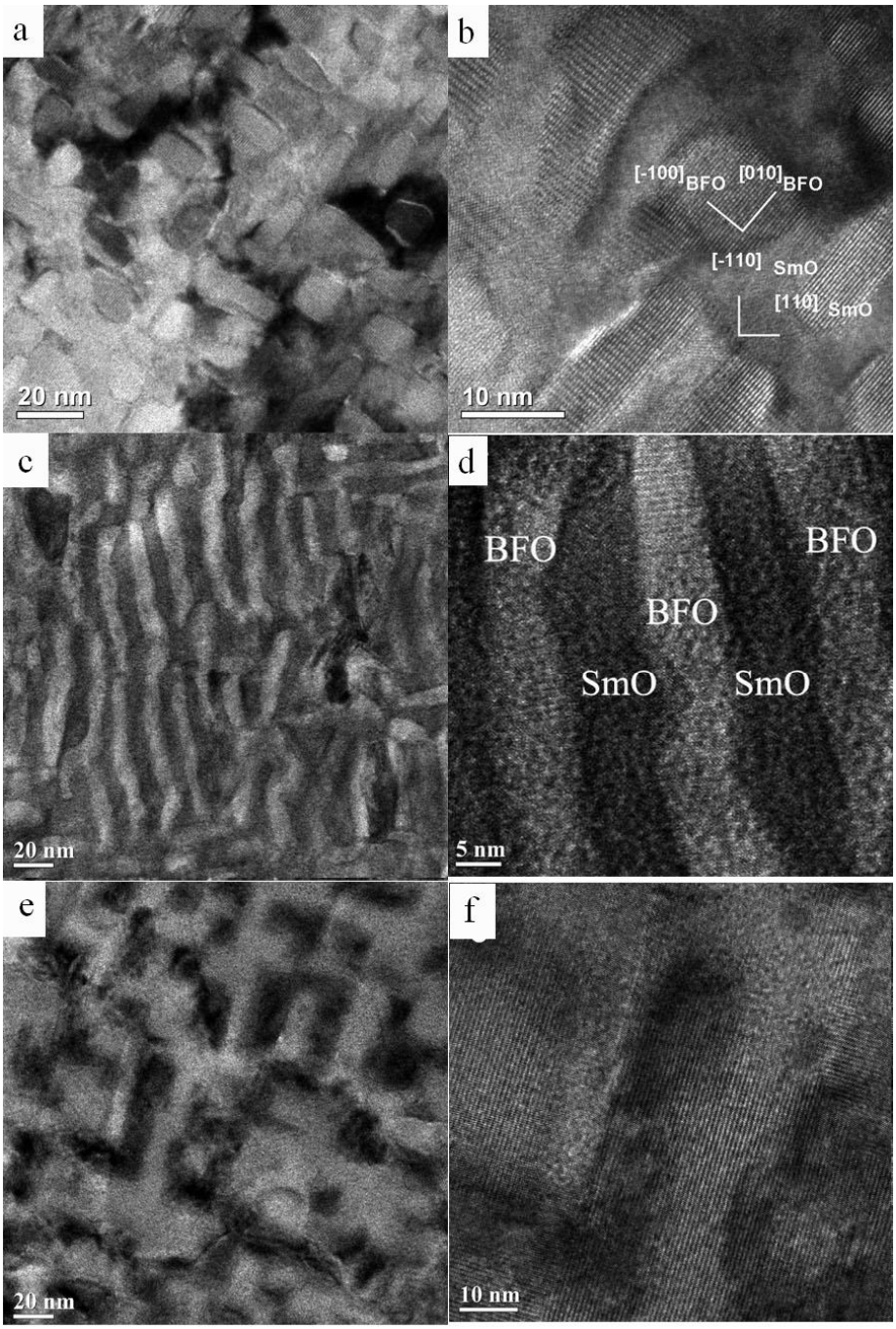

FIG. 1.29. Plan-view TEM images show the surface morphologies of $BiFeO_3$:Sm_2O_3 VAN thin film grown on $SrTiO_3$(001) substrate with different film compositions. (a) 50:50, (b) 60:40 and (c) 75:25.

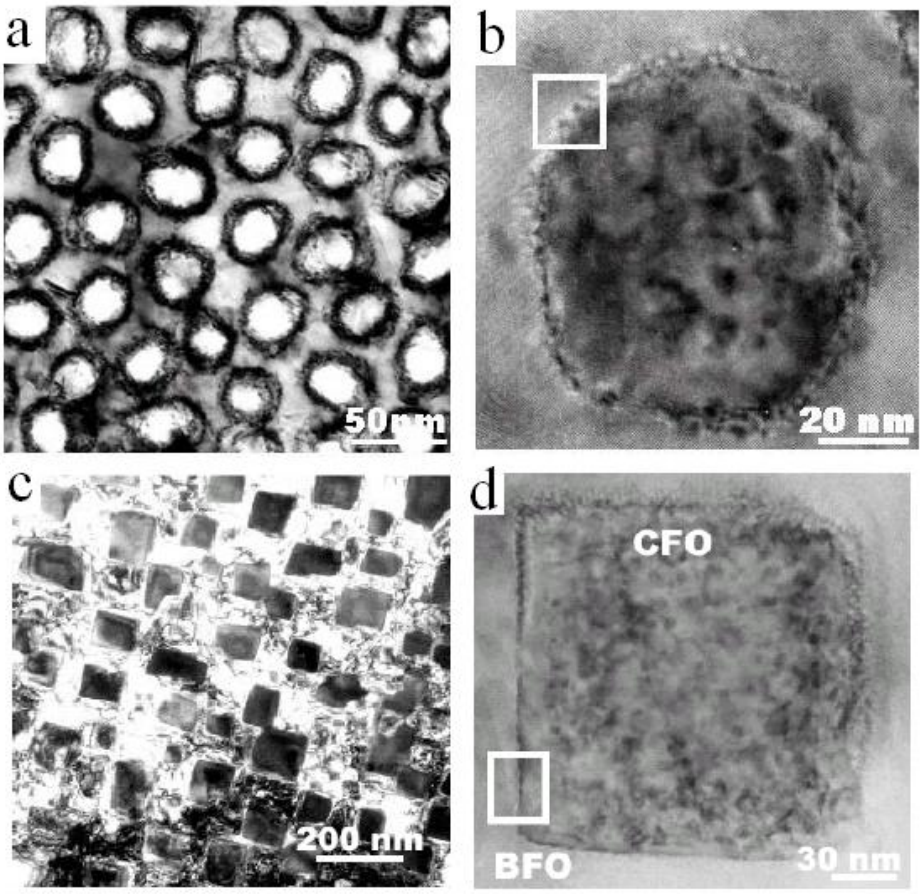

FIG. 1.30. Plan-view TEM images of $BaTiO_3$:$CoFe_2O_4$ (a and b) and $BiFeO_3$:$CoFe_2O_4$ (c and d) nanocomposite thin films, respectively. CFO phases were doped as nanopilars in the nanocomposite films for all cases.

The main challenge of VAN thin film growth is to create the vertically aligned columnar structure well and maintain good phase qualities. Since the VAN composites heavily rely on phase separation, it is important to carefully select proper materials and

build the VAN system. Furthermore, accurate control on the kinetic and thermodynamic parameters during the film growth may also be helpful.

1.5.2 Strain tuning in VAN thin films

Tunable strain can be achieved in VAN thin films through material selections as well as experimental parameter control. The effectiveness of the vertical strain depends on the quality of the columnar interfaces, and their area density is related to that of the film-substrate interface.[100] Figure 1.31 demonstrates the tunable strain control in VAN thin films as a function of film thickness and compared with that of bulk materials. The incorporation of ZnO phase switched the vertical strain state of LSMO phase from compression (substrate strain control) to tension (vertical strain control), as shown in Figure 1.30a. The investigation on BFO:SmO VAN system reveals that the in-plane SmO strain state is switched from compression to tension by the presence of BFO. The transition occurs at a thickness (around 20nm) similar to the column width. Those samples demonstrated the tunable strain states can be achieved by varying the film thickness in VAN thin films.

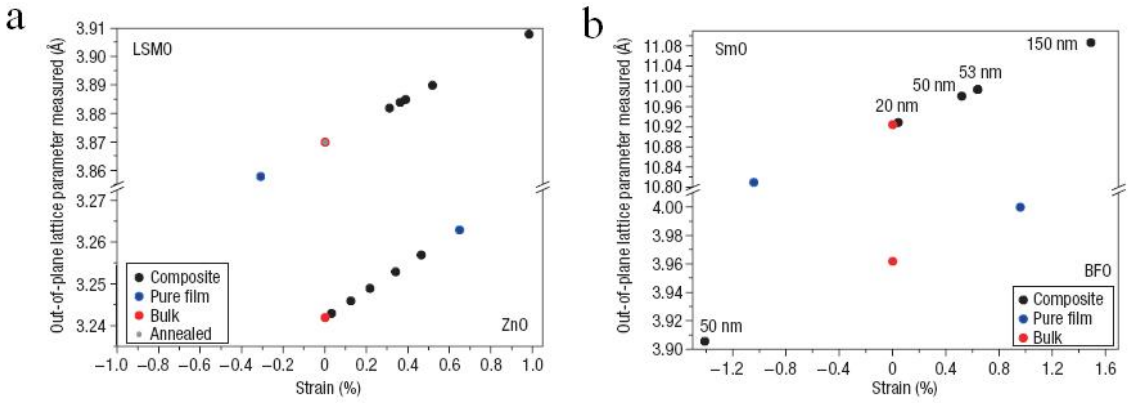

FIG. 1.31. Tunable strain control in LSMO:ZnO and BFO:SmO VAN thin films. (a) out-of-plane lattice constants of LSMO versus calculated vertical interfacial strain in LSMO:ZnO VAN thin films; (b) out-of-plane lattice constants of BFO versus calculated vertical interfacial strain in BFO:SmO VAN thin films.

Besides the VAN films thickness, the vertical interfacial strain area density can also be tuned by adjusting the column width with different composite film composition and deposition parameters.[114] Detailed study will be conducted later in Chapter III.

1.5.3 Interfacial effects in VAN thin films

Novel electron systems can be generated at well-defined interfaces in complex oxides. Much progress has been achieved in exploring the fundamental properties of oxide interfaces, and it is clear that those electron systems offer great potential for

possible future device applications. Those phenomena that arise in oxide interfaces include spaced ions interacting with electrons, the unique electronic character of oxygen ions and interactions among the electron. Oxide interfaces make them all deviate from free-particle behaviors. And many oxide interfaces will become electronically active by altering the hybridization of the ionic orbital and by modifying the orbital and spin ordering to couple the lattice structure.

The VAN thin films provide nice interfaces both on horizontal and vertically between phases. There is a possibility to translate the unexpected interface-induced novel properties observed in multilayers to VAN structures since the latter one can provide much larger interfacial areas and give much larger signals. The effect of vertical interface on the physical properties of metal oxide is profound and can be used to tune the physical properties of materials. Yang *et al.* reported the electrical properties study of the vertical interface effect in $BiFeO_3$:Sm_2O_3 VAN thin films.[103] As shown in Figure 1.32, the dielectric loss and the leakage current density of the $BiFeO_3$:Sm_2O_3 nanocomposite are all much lower than that of pure BFO films.[103] Considering the nature of the leakage current of nanocomposites is controlled by the major phase and the much lower leakage current density implies a much larger interfacial area of BFO phase. On the other words, it is the larger vertical interfacial area in BFO:SmO nanocomposite that contribute to the reduction of leakage current density of the BFO phase. This work represents a novel way of enhancing functionalities of oxide films by both strain coupling and interfacial area increasing in VAN architecture.

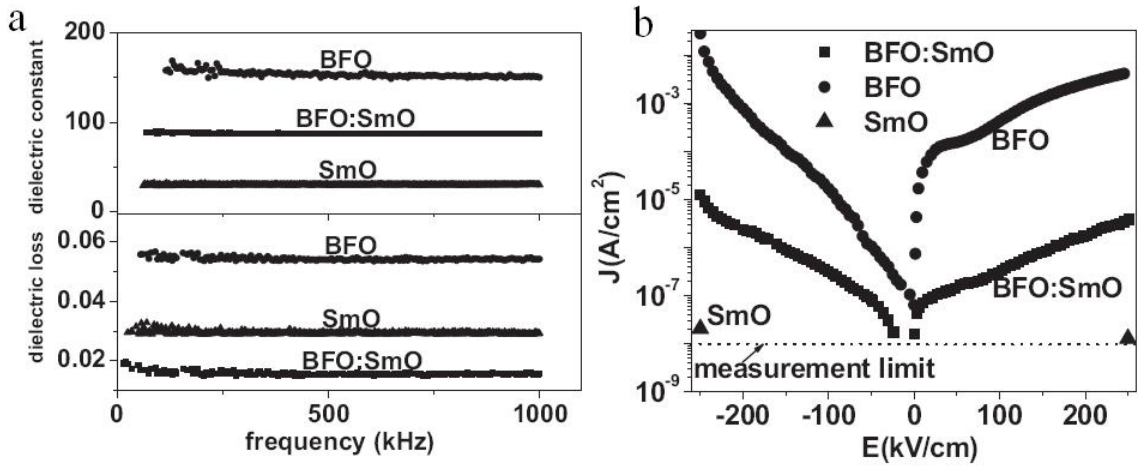

FIG. 1.32. (a) Dielectric constants and dielectric loss of BFO:SmO, BFO and SmO thin films; (b) leakage current density versus electric field characteristics of BFO:SmO, BFO and SmO thin films.

The enhancement in the properties of VAN thin films results primarily from the interaction between the component phases. The structure of VAN thin films formed by perovskite and spinel phases ($BiFeO_3$:$NiFe_2O_4$) has been investigated at nano-scale using advanced transmission electron microscopy (TEM) techniques.[122] As shown in Figure 1.33, the BiFeO layer in $BiFeO_3$ matrix was found to bond to the [Ni,Fe]O_2 layers of the $NiFe_2O_4$, giving a minimized interface charging and a maximized structure continuity across the interface, which result in a stronger elastic coupling.

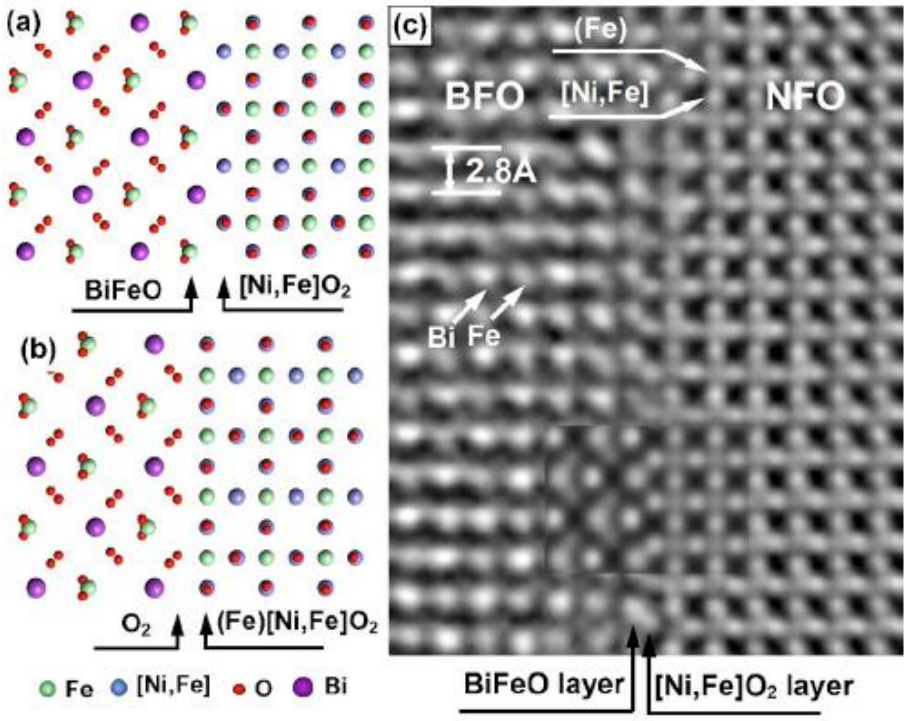

FIG. 1.33. (a) and (b) Structure models of the $BiFeO_3$:$NiFe_2O_4$ interface; (c) the phase of the electron exit wave along [001] zone axis.

The vertical interfaces in VAN thin films also has the potential to tune the magnetrotransport properties of materials including colossal magnetoresistance (CMR) and further more the low field magnetoresistance properties (LFMR). It has been demonstrated that the enhanced magnetotransport occurred at the grain boundaries (GBs) in polycrystalline perovskite manganites, where the magnetic spin alignment is obstructed and the spin-polarized tunneling happened.[103] Much work can be done to

increase the interfacial GB areal density or the disordered regions at the GBs by incorportating an insultiong oxide phase with perovskite manganite into VAN thin films. A improved LFMR of ~12% was reported at an external magnetic field of H=1T at 77K in $La_{0.7}Sr_{0.3}MnO_3$:ZnO VAN thin films. It is highly possible due to the enhanced GBs effect at the vertical interface between phases.[37]

1.5.4 Nanostructures achieved from VAN thin films

In nanostructured materials and related devices, scaling sizes down to tens of nanometers is appealing for device miniaturization and giving the opportunity of exploring novel phenomena raised from nanometer-size effects. The device miniaturization will pose not only technological challenges but also new architecture design at nanoscale.[103] To fabricate nanostrucres, classical top-down patterning processing always starts with a thin film, fabricating structures of desired geometry out of it by photolithography and etching, as shown in Figure 1.34a. This flow shows the process of high density $Pb(Zr_{0.2}Ti_{0.8})O_3$ (PZT) nanocapacitors using anodized aluminium oxide (AAO) mask as the growth template.[101] Main drawback of this process is that the etching of the perovskite oxides is complex and usually renders a damaged region at the rim of the patterned structures.[103]

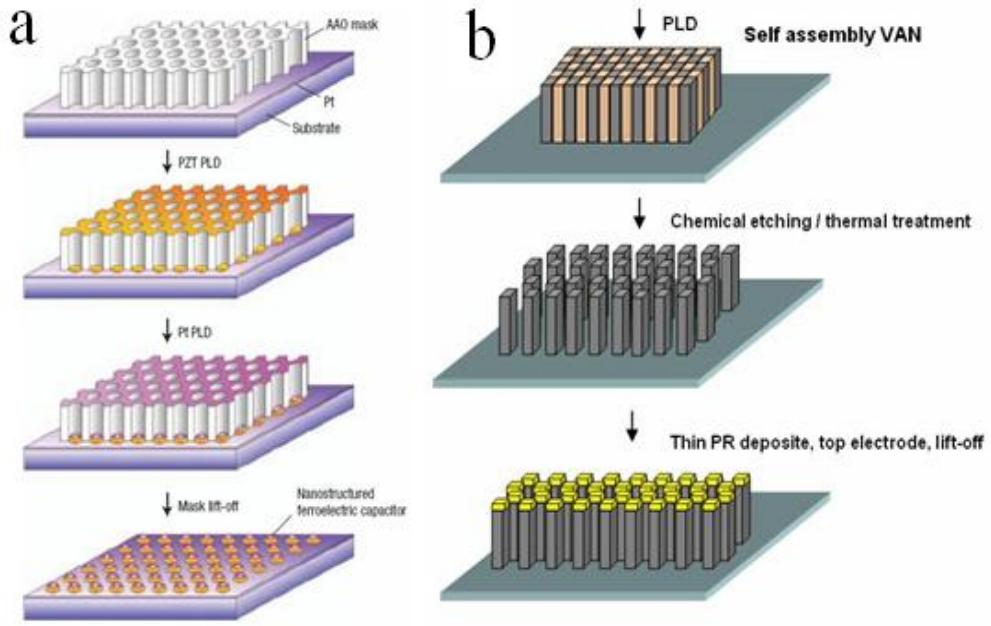

FIG. 1.34. (a) The top-down process flow of fabricating PZT nanocapacitor arrays by AAO template; (b) self-assembly growth of nanocapacitor arrays by VAN thin films and followed etching and lift-off procedures.

VAN architecture could work as a growth template to process self-assembly nanostructures, which would allow to pattern large area arrays of high-quality, epitaxial nanostructures with lateral dimensions in a range below 100nm. Figure 1.34b reveals a proposed self-assembled growth of ultra high density nanocapacitors. Well ordered VAN thin films can be grown on a large substrate by physical vapor deposition such as pulsed laser deposition. One of the phases will be following splitted out either by chemical method such as chemical etching and reactive ion etching, or physical

methods such as thermal treatment on components with different melting temperatures. The final top electrodes can be selectively deposited by photoresist-assisted lift-off process. Column widths as well as the dimension of single nanocapacitor in the self-assembly grown arrays are much finer as compared to the reported records of the one processed by traditional top-down techniques and will lead to a much higher storage density (1Tb $inch^{-2}$).

Based on the self-assembly growth of nanoisland arrays as mentioned above, the VAN architecture can also lead to other nanostructures such as nanowire, nanorods and nanopores.[103] The key aspects of the work will be material selection in VAN thin films and the proper selective etching to eliminate one of the composite phases.

CHAPTER II

RESEARCH METHODOLOGY

2.1 Pulsed laser deposition

Laser is an acronym for "Light Amplification by Stimulated Emission of Radiation". Basically， three key elements, resonance structure, gain medium and pumping source are needed to be combined together in a system and generate a very collimated, monochromatic and coherent beam of laser. In the pulsed laser mode, the output of a laser varies with respect to time, typically taking the form of alternated 'on' and 'off' periods. The laser has been with great popularity in divers and broad applications in many areas such as military, medical, metallurgy and semiconductor manufacturing. As an outstanding representative, the pulsed laser deposition (PLD) has achieved significant development in the past 30 years and becoming a broadly applicable technique for thin film deposition.[103,136]

Physical vapor deposition (PVD) is a variety of thin film deposition methods with the condensation of vaporized materials from the target onto various surfaces in a vacuum chamber. PLD is one of the standard PVD techniques with very simple system setup. As shown in Figure 2.1, a PLD system basically consists a target holder and a substrate holder in a vacuum chamber which maintained by a second level turbomolecular pump.[137] The bulk ceramic target is oriented at an angle of 45º to the incident laser beam and right confront to the substrate holder. A high power pulsed

laser will be used as external energy that shot onto the target surface which will vaporize the material and have the material transported onto the substrate surface. The distance between the target and deposited substrate is usually maintained at 4 - 5cm. The substrate holder can be heated up to 1200℃ and a precisely temperature control can be achieved with embedded computer controlled thermal couples. With proper film grown parameters including the substrate temperature, laser energy density, pulse repetition rate and proper working gas, high quality thin film can be deposited.

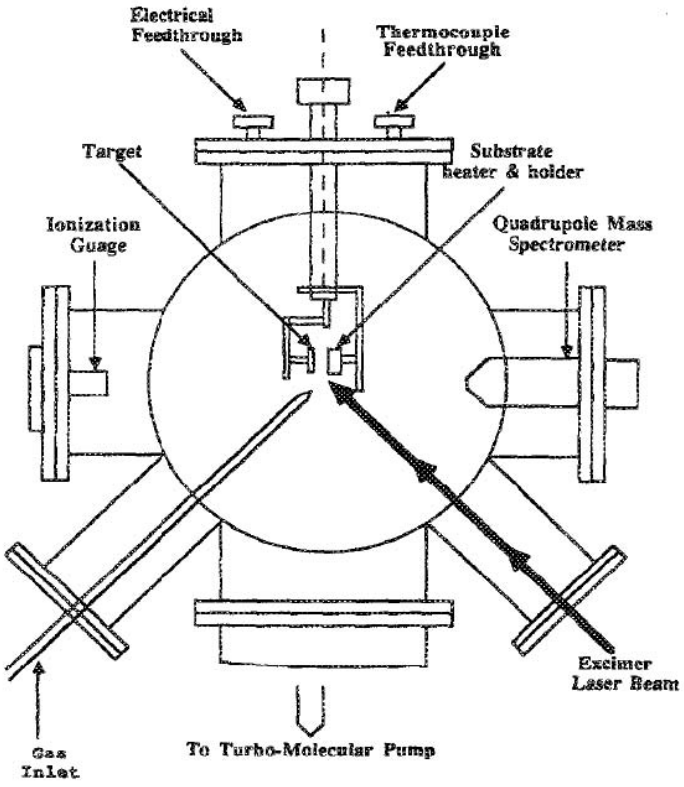

FIG 2.1. Schematic of a single target pulsed laser deposition system.

In general, the useful range of laser wavelengths for thin film growth in PLD is between 200nm and 400nm. Most of the works have been done by PLD were using excimer laser and Nd^{3+}:YAG lasers as the deposition source. Yttrium aluminum garnet (YAG) lasers are solid-state systems which generate high output laser energies by using two YAG rods in an oscillation modes. The excimer is a gas laser system in which the excimer molecules are formed by mixture their component gases. KrF is one of the highest gain systems for electrically discharged excimer lasers with 248nm wavelength and has been used in this work. A set of optical components including lenses, apertures and mirrors are placed in between the output of laser and the deposition chamber in order to steer and focus the beam. The beam splitters can split the laser beam into two or more separate beams. It can help build multiple deposition systems with multiple chambers but sharing with only one laser source.

PLD is an extremely versatile technique that can be used to prepare a wide range of materials in thin film. Different to its simple experimental setup, the PLD technique is quite a complex physical phenomenon. The theoretical descriptions including the laser-target interaction, the interaction of laser beam with evaporated materials and adiabatic plasma expansion, and it combines both equilibrium and nonequilibrium processes. When a laser beam was absorbed by a target surface, the electromagnetic energy of the incident laser will first converted into electronic excitation and then into thermal, chemical and mechanical energy. These energy transactions will cause material evaporation, ablation, excitation, plasma formation and exfoliation. A plume will formed by the material evaporation and consists of a mixture of energetic species

including small particles, molted globules, clusters, molecules, atoms, ions, and even electrons.

In 1990, R. K. Singh and J. Narayan systematically descripted the basic PLD physical principles in the following subsections.[138] The physical stages in PLD are the laser-target interactions during the laser radiation and the after, which can be separated as three separate regimes. Those three regimes are including: 1) the interaction of the laser beam and the target material which results the evaporation of the surface layers, 2) the interaction of the evaporated material with the incident laser beam which results an isothermal plasma formation and expansion, and 3) the anisotropic adiabatic expansion of the plasma which leads to the characteristic nature of the laser deposition process. The first two regimes happen at the start of laser radiation and through the laser pulse duration (about 25 ns duration), and the last adiabatic expansion happens right after the laser pulse terminates. Figure 2.2 shows the first laser-target interaction regime during the pulsed laser period.[138]

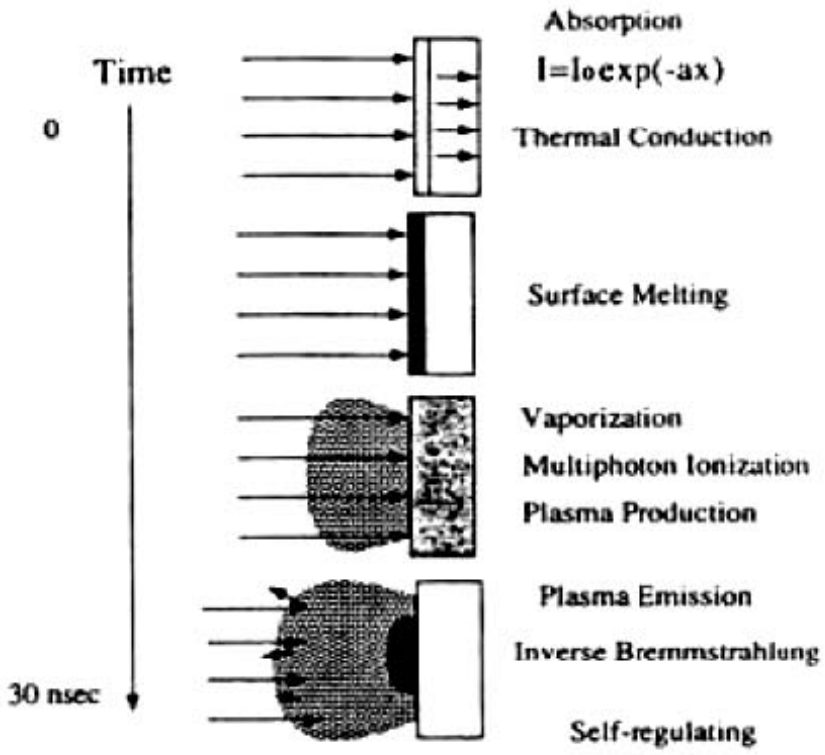

FIG 2.2. Representation of the laser target interaction stages during the short pulsed laser period.

The interaction between high power laser pulses and the target results in the melting and evaporation of the surface layers. Both the pulsed laser and target material properties will affect the interaction. With appropriate boundary conditions, a one-dimensional heat flow equation can simulate the case of three-dimensional heat flow to address the heating and melting process. The equation is given by:

$$\frac{\rho_i(T)C_p(T)\alpha T_i(x,t)}{\alpha_t} = \frac{\alpha(\frac{K_i(T)\alpha T_i(x,t)}{\alpha_x})}{\alpha_t} + I_0(t)\{1-R(T)\}e^{-\alpha(T)x} \qquad (2.1)$$

where x is the direction perpendicular to the sample, t is the time, i refers to the solid and liquid interfaces, $\rho_i(T)$ is the temperature dependent density, $C_p(T)$ is the thermal heat capacity, $R(T)$ is the temperature dependent reflectivity, $a(T)$ is the absorption coefficient, $I_0(t)$ is the time dependent incident laser intensity and K_i is the thermal conductivities of solid and liquid phases at the interface. This equation can provide accurate numerical solutions by the finite difference method to characterize the properties of pulsed laser irradiated material.

The high-power pulsed laser beam irradiation on target surface will cause a high temperature (>2000K) which will further lead to an emission of the positive ions and electrons out of the surface. The emission of electrons can be described in exponential increasing as a function of the temperature from the Richardson's equation. And the thermal emission of ions can be calculated from the Langmuir-Saha equation as show below:

$$\frac{i_+}{i_0} = \frac{g_+}{g_0} e^{(\phi - I)KT} \qquad (2.2)$$

where i_+ and i_0 are the positive and neutral ion fluxes respectively, g_+ and g_0 are the statistical weight of the positive ionic and neutral states respectively, ϕ is the electron work function, and I is the ionization potential of the evaporated material.

While the plasma regime is being constantly augmented at the inner edge by the evaporated materials, ions with higher density will be produced near the surface of the

target. The outer edge of the plasma regime is transparent to the laser beam and the target surface will continually absorb energy from laser radiation. A schematic diagram in Figure 2.3 shows that during the incidence of the laser, there are totally four different regions could be distinguished as: 1) the unaffected bulk target, 2) the evaporating target surface, 3) the area near the surface absorbing laser beam energy and 4) the rapidly expanding outer edge which is transparent to the laser beam.[138]

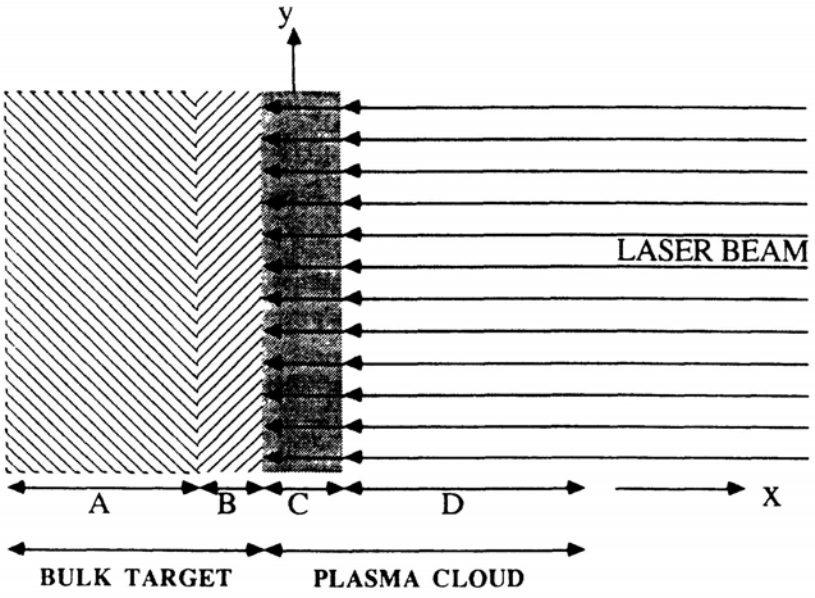

FIG 2.3. Schematic diagram shows the different phases presented during the laser-target interaction.

After the plasma formation and its initial isothermal expansion, the adiabatic expansion of the plasma in vacuum working chamber will give rise to the laser-deposition process. In this regime, the thermal energy is converted to kinetic energy, and the velocity of the plasma will increase as the thermal energy of the plasma will decrease. Mainly there are two points can help address the slowly temperature drop. First of all, the cooling will be balanced by the energy regain from ions recombination processes. Secondly, the plasma will only expand in one direction since the initial dimensions are much larger than the transverse directions in an order of 10s. The last stage of PLD is the deposition of ablated materials onto the substrate, its nucleation and growth as thin film on the substrate surface. This stage is important to determine the quality of the deposited thin film. The ejected species by laser-target interaction always with high energy and may induce various damages to the substrate. The energetic species will sputter the substrate surface atoms and form a collision region between the incident flux flow and the sputtered atoms. When the condensation rate is higher than that of the flux, a thermal equilibrium condition can be reached and film starts to grow on the substrate.[139]

The future development of the PLD technique will be always equipped with other techniques. For example, with the introduction of high-pressure reflection high-energy electron diffraction (RHEED) in PLD, the growth rate control on an atomic level and a in situ growth studies can become possible.[140] And the development of ultrafast laser ($<10^{-11}$/s pulses) can help product a fully atomized continuous flow of the ablated material, which can results in films with super quality. Given the recent results

obtained with coated-conductor systems by PLD, it is apparent that PLD would be able to coat large size substrates (>200mm). And new products and PLD equipment for both R&D and production are being commercialized at a steady pace.[136]

2.2 Thin film microstructure and crystalline characterizations

The characterization of deposited thin films in this dissertation including using non-destructive and destructive techniques which allows the determination of microstructure, crystalline quality, defect and impurities presence, etc.

2.2.1 X-ray diffraction (XRD)

X-ray diffraction (XRD) is a very convenient, versatile and non-destructive technique that reveals detailed information about the chemical composition and crystallographic structure of natural and manufactured materials. When a monochromatic X-ray beam strikes on a crystal, it will diffract into different specific directions. From the angles and the intensities of the diffracted beams, a three-dimensional plotting of the crystal can be simulated. Not only an effective way to determine the orientation of a single crystal or grain, the XRD can also help find the crystal structure of an unknown material or measure the size, shape and internal stress of small crystalline regions.[141]

As the most fundamental formula to address the effect of XRD, Bragg's Law refers to the simple equation as below:

$$n\lambda = 2d\sin\theta \qquad (2.3)$$

It explains why the cleavage faces of crystals appear to reflect X-ray beams at certain angles of incidence (ɵ, λ). As shown in Figure 2.4, the variable d is the distance between atomic layers in a crystal, and the variable lambda is the wavelength of the incident X-ray beam; n is an integer.[142]

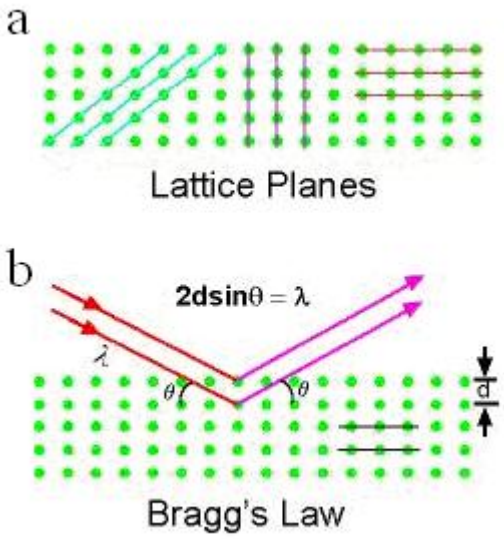

FIG 2.4. (a) A two dimensional periodic array of atoms that forms different planes in the crystal, (b) diffraction for a set of planes with inter-plane distance d which is conditioned to Bragg's Law.

By varying the angle theta, the Bragg's Law conditions are satisfied by different d-spacings in polycrystalline materials. Plotting the angular positions and intensities of the resultant diffracted peaks of radiation produces a pattern, which is characteristic of the sample. Where a mixture of different phases is present, the resultant diffractogram is formed by addition of the individual patterns. Although Bragg's Law was used to explain the interference pattern of X-rays scattered by crystals, diffraction has been developed to study the structure of all states of matter with any beam, e.g., ions, electrons, neutrons, and protons, with a wavelength similar to the distance between the atomic or molecular structures of interest.

Thin film diffraction does not mean a specific technique but it refers to a collection of x-ray diffraction techniques that used to characterize thin film samples. These materials have important technological applications in microelectronic and optoelectronic devices, where high quality epitaxial films are critical for device performance. Several special points needed to be taken consideration before using x-ray diffraction to characterize thin film samples. First, reflection geometry is used for these measurements but the substrates are generally too thick for transmission. Second, high angular resolution is required because the peaks from semiconductor materials are sharp due to very low defect densities in the material. As a result, multiple bounce crystal monochromators are used to provide a highly collimated x-ray beam for these measurements. Besides the traditional precisely lattice constants measurement, several other measurements are also very important and can be done on thin film samples by x-ray diffraction.[143] Those measurements include x-ray reflectivity, glancing angle x-ray

diffraction, high resolution x-ray diffraction, residual stresses analysis, texture analysis and rocking curve measurements.

2.2.2 Transmission electron microscopy (TEM)

Transmission electron microscopy (TEM) is one of the most efficient and versatile tools for materials characterization. Historically, TEMs were developed because of the limited image resolution in traditional optical microscopes which imposed by the wavelength of visible light. In this dissertation, extensive TEM works have been conducted to characterize the morphology, crystallography as well as chemical informations of nanocomposite thin films. TEM facilities in this work include the JEOL 2010 analytical microscope (200KV, LaB_6 filament with 0.23nm point resolution) and FEI Tecnai F20 analytical microscope (200KV, ZrO_2/W Schottky firld emitter with 0.27 point resolution, Z-contrast dark-field STEM imaging using the HAADF detector). In addition to the regular single-tilt and double-tilt holders, heating stage (up to 1200 °C) and Be double-tilt holder have also been used for in situ-heating and Energy Dispersive X-ray Spectrometer (EDX) experiments, respectively.

As shown in Figure 2.5, a typical TEM system contains four parts: the electron source, electromagnetic lens system, sample stage and imaging systems which all combined in a vacuum column.[144] The electron source consists of a cathode and an anode. The cathode will emit electrons when being heated. A negative cap confines the electrons into a loosely focused beam. The beam is then accelerated towards the specimen by the positive anode. Electrons at the rim of the beam will fall onto the anode while the others at the center will pass through the small hole of the anode. After leaving the electron source, the electron beam is tightly focused using electromagnetic lens and metal apertures. The system only allows electrons within a small energy range to pass through, so the electrons in the electron beam will have a well-defined energy. The imaging system consists of another electromagnetic lens system and a screen. The electromagnetic lens system contains two lens systems, one for refocusing the electrons after they pass through the specimen, and the other for enlarging the image and projecting it onto the screen. The screen has a phosphorescent plate which glows when being hit by electrons.

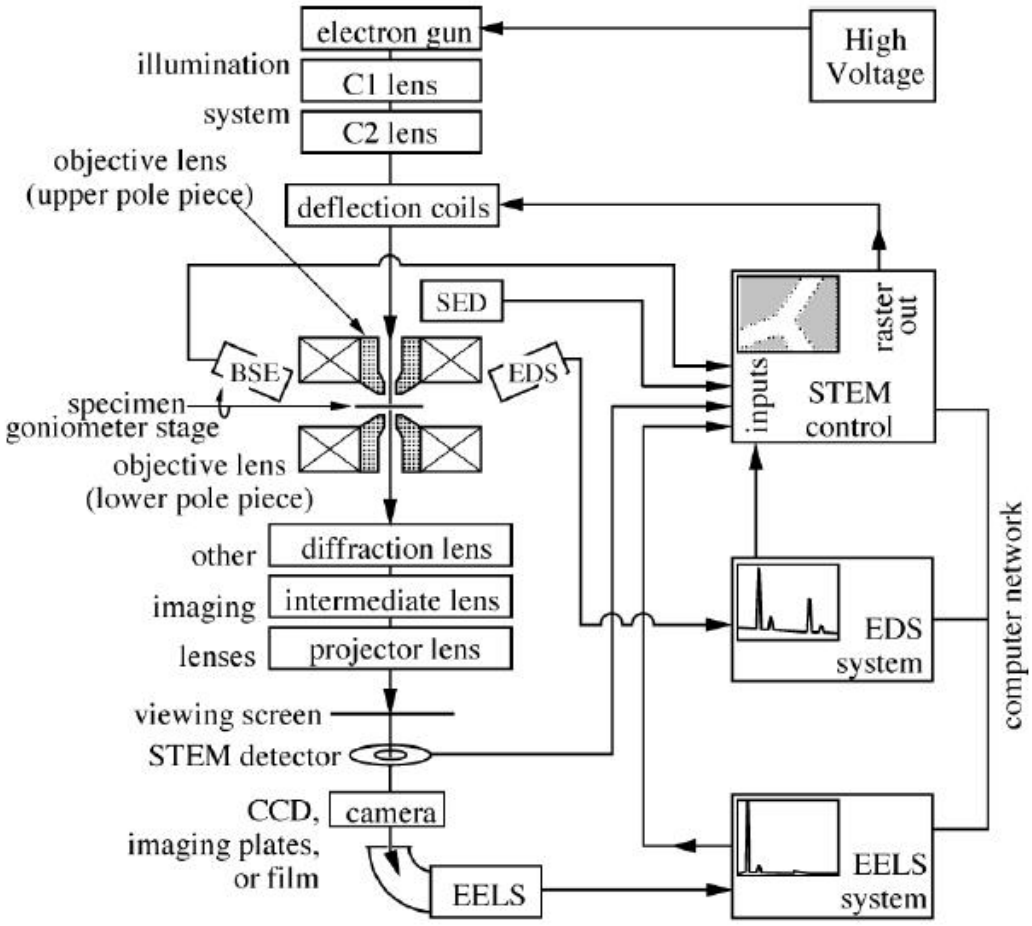

FIG 2.5. The block diagram of a typical TEM system with analytical capabilities.

The resolving power of TEM can be defined as the closest spacing of two points which can clearly be seen through the microscope to be distinguished as separate entities. The diffraction effect limits the resolution of a microscope because the light from a very small point in the object suffers diffraction, particularly by the objective aperture, and even an infinitesimally small point becomes a small Airy disc in the

image. In order to make this disc as small as possible, the aperture must be as large as is feasible. Rayleigh proposed a criterion which works well in most cases and has been used extensively ever since; when the maximum intensity of an Airy disc coincides with the first minimum of the second, then the two points can be distinguished. Figure 2.6 illustrates that the resolution limit is $d_1/2$.[145] Microscopes apertures are normally referred to in terms of the semi-angle, α, which subtends the specimen. Then, it is possible to derive from diffraction theory an expression for the resolution,

$$r = \frac{0.61\lambda}{n\sin\alpha} \qquad (2.4)$$

where λ is the wavelength of the radiation, *n* is the refractive index of the medium between the object and the lenses, and α is the semi-angle of collection of the magnifying lens. The $nsin\alpha$ is usually called the numerical aperture (NA).

Not only the high resolution images can be achieved with short wavelength of electrons, but also the further magnification of the images can be adjusted by the lenses in TEM. Magnification refers to the degree of enlargement of the diameter of a final image compared to the original. In practice, magnification equals a distance measured between two points on an image divided by the distance measured between these same two points on the original object. There are at least three magnifying lenses in an electron microscope: the objective, intermediate, and projector lenses. The final magnification is calculated as the product of the individual magnifying powers of all of the lenses in the system.[145]

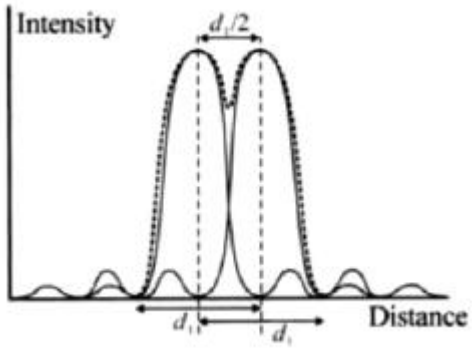

FIG 2.6. The intensity of the Airy rings from two neighboring pinholes. The intensity distributions from each of the pinholes separately and the maximum intensity from one pinholes coincides with the first minimum from the other giving a resolution limit of $d_1/2$.

There are two basic operation modes of the TEM system: the diffraction mode and imaging mode as shown in Figure 2.7. By changing the focal length of the intermediate lens, diffraction mode and imaging mode can be easily obtained in the TEM. In the diffraction mode, the image plane coincides with the back focal plane of the objective lens; while in the image mode, the image plane coincides with the image plane of the objective lens. In the simple imaging mode, the specimen always shows little contrast. To increase the contrast objective apertures are inserted at the back focal plane of the objective lens in the conventional imaging mode, which is called diffraction contrast. When the aperture is positioned to allow only the transmitted (undiffracted) electrons

to pass, a bright-field (BF) image will be formed. When the aperture is positioned to allow only some diffracted electrons to pass, a dark-field (DF) image will be formed.

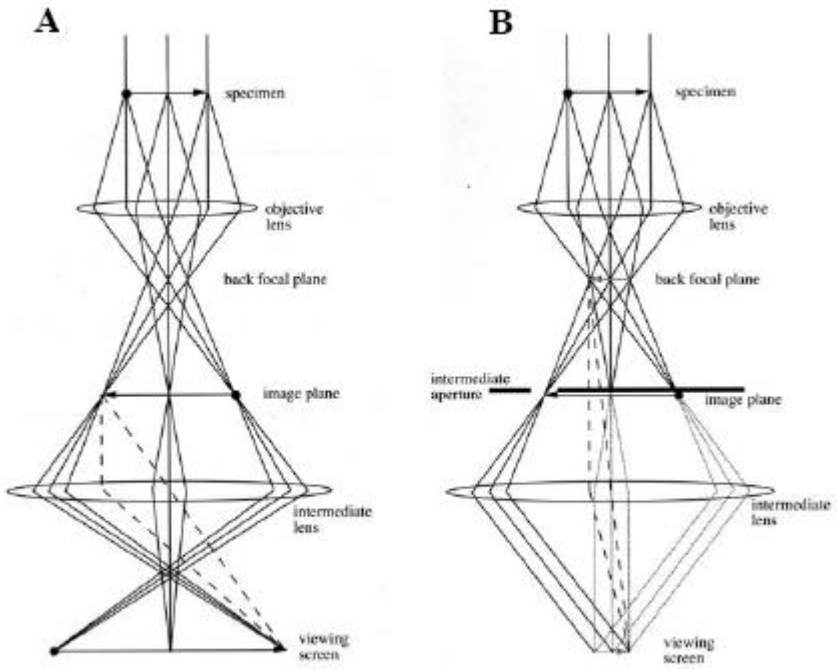

FIG 2.7. Two basic operation modes of TEM system: (a) the diffraction mode and (b) the imaging mode.

High resolution TEM is an imaging mode of the TEM that allows the imaging of the crystallographic structure of a sample at an atomic scale. Because of the high

resolution, it is an invaluable tool to study nanoscale properties of crystalline material such as semiconductors, metals and complex oxides. To achieve HRTEM, there are several aspects and related simulation work need to be satisfied. The objective lens should be adjusted to give the shortest possible focal length and the proper specimen holders must be used. Adjustments need to be done carefully, such as the use of higher accelerating voltages, will results in higher resolution. Chromatic aberration may be further lessened by using field emission guns since the energy spread of electrons generated from such guns is considerably narrower. For most specimens, larger objective lens apertures should be used to minimize diffraction effects. If contrast is too low due to the larger objective aperture, smaller apertures may be used but resolution will be diminished. In addition, they must be kept clean since dirt will have a more pronounced effect on astigmatism. Small condenser lens apertures will diminish spherical aberration, but this will be at the expense of overall illumination. Specimen preparation techniques may also enhance the resolution capability. Extremely thin sections, for instance, will diminish chromatic aberration.

In HRTEM images, the image contrast are largely depends on the parameters of the microscope and the specimen. Simple interpretations of image contrast in terms of columns of atoms are possible only for a narrow range of experimental conditions. Multislice method is a dynamical calculation of diffracted amplitudes of electron beams and can help to simulate the beam-specimen interaction as shown in Figure 2.8.[146] The effect of the first slice on the phase of the incident wavefront is calculated, and the resulting wavefunction is then propagated through free space to the next slice.

This process is repeated until the desired specimen thickness is achieved. The method is highly accurate, assuming Δz is sufficiently small.

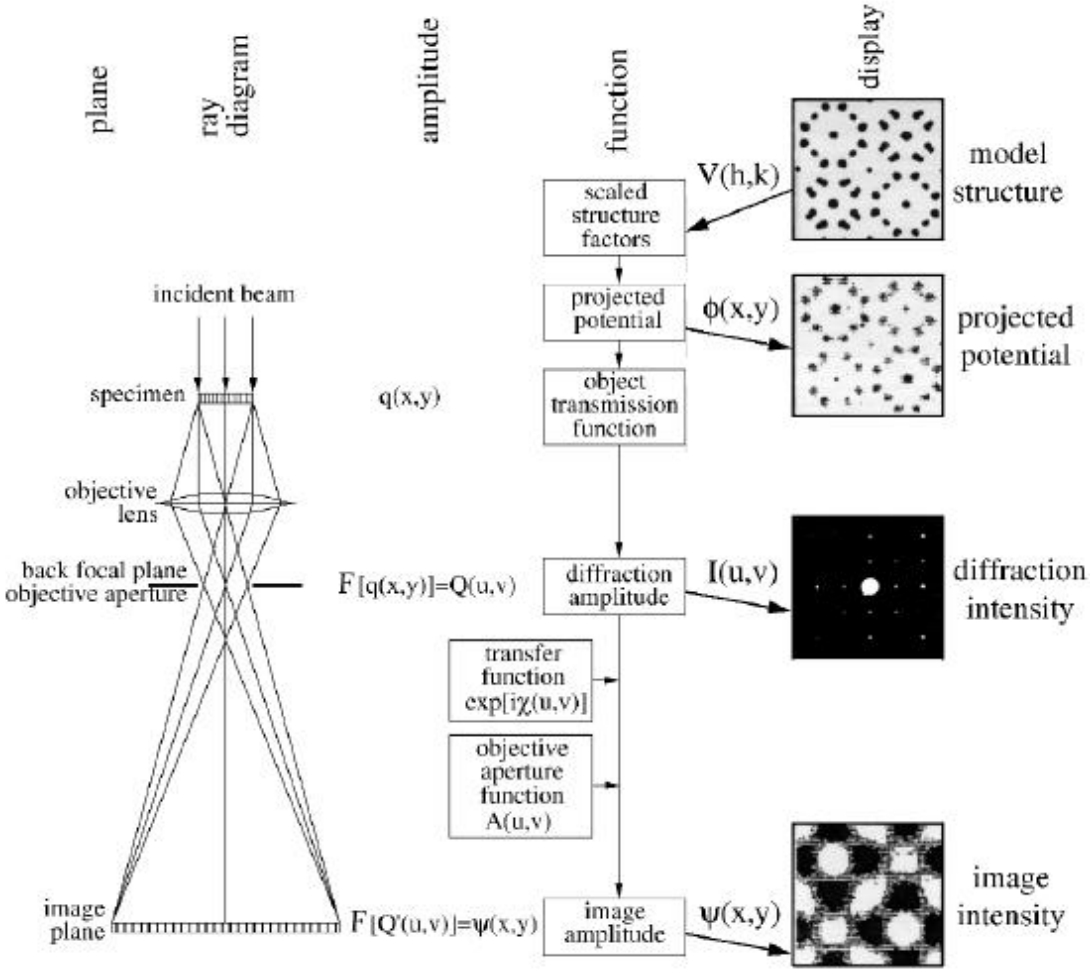

FIG 2.8. Multiple steps in the calculation of a high-resolution TEM image by the multislice method.

The scanning transmission electron microscope (STEM) is one of the working modes of TEM where the beam scan parallel to the optic axis at all times so that it mimics the parallel beam in parallel to its scanning. Figure 2.9 shows the schematics of scanning the convergent probe for STEM images.[147] The double-defection process ensures that the probe remains parallel to the optics axis as it scan across the specimen surface. The rastering of the beam across the sample makes these microscopes suitable for analysis techniques such as mapping by energy dispersive X-ray (EDX) spectroscopy, electron energy loss spectroscopy (EELS) and annular dark-field imaging (ADF). These signals can be obtained simultaneously, allowing direct correlation of image and quantitative data. By using a STEM and a high-angle detector, it is possible to form atomic resolution images where the contrast is directly related to the atomic number (Z-contrast image). The directly interpretable z-contrast image makes STEM imaging with a high-angle detector appealing. This is in contrast to the conventional high resolution electron microscopy technique, which uses phase-contrast, and therefore produces results which need interpretation by simulation.

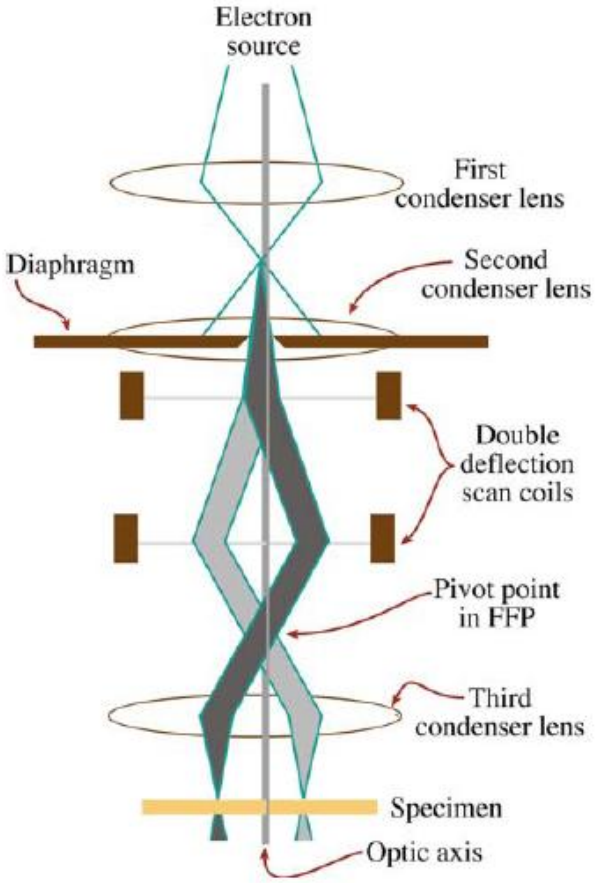

FIG 2.9. Schemadic diagram of the scanning of convergent probe for STEM imaging.

TEM specimen preparation is a very broad subject. The main challenge of this work is finally achieving a thin region less than 100nm in the sample to get electron transparency. Certain selection of specimen preparation methods depends on the material information you are looking for and the material features. For complex oxide thin films studied in this dissertation, we usually prepare cross-section TEM specimen

to see the film-substrate interface and plan-view TEM specimen to see the nanocomposite films growth morphologies. Manually, the thin films specimen can be paocessed as the following steps: (1) thin slice cutting from bulk sample; (2) slices glue and prethinning; (3) final thinning of the disks and (4) final grinding. The prethinning can be down by tripod polisher which has been used for many decades with the help of diamond lapping films and diamond polishing paste. The final thinning can be done by either electropolishing or ion-milling. Ion-milling is a powderful tool to finally thin the sample down to 100nm scale. Various factors can be adjusted include ion energy, angle of incidence, vacuum, initial surface topology, ion orientation and beam energy. Another TEM specimen preparation method that has been rapidly adopted by the semiconductor industry is FIB assisted method. In a FIB-SEM dual system, the ion gun produces well-controlled beam of Ga ions. Two staircases can be cut on either side to leave a thin wall. The ion-polish can get the wall really thin as required in TEM and finally the wall will be attached to a probe for lift out and place it on a supporting film.

2.3 Magnetism and magnetotransport properties measurement

Thin films magnetism and magnetotransport properties in this dissertation were measured by a Physics Property Measurement System (PPMS) (EverCool, Quantum Design, Inc) combined a vibrating sample magnetometer (VSM) head. The PPMS provides a flexible, automated workstation that can perform a variety of experiments requiring thermal control including magnetic and electro-transport measurements. The

control of PPMS sample environment includes magnetic fields up to ±9 T and a 1.9 - 400K temperature range. The temperature can be varied with full sweep capability and slew rates from 0.01 K/min up to 12K/min. The system thermometer is located at the bottom of the sample chamber. There is another thermometer on the rotator which is used for temperature control of loaded samples. Since it is very adjacent to the sample, superior temperature controlling is achieved. The temperature is stabilized within ±2 mk during measurements.

The AC transport measurement option in PPMS incorporates a precision current source and a precision voltmeter in a package platform. Measurements are typically made by passing a known current through the sample and measuring the voltage drop across the sample direction. The ACT option supports four-terminal alternating current resistivity measurements. In this mode, two leads pass a current through the sample, two separate leads are used to measure the potential drop across the sample, and Ohm's law is used to calculate the sample resistivity. Figure 2.10 shows the sample rod used for transport properties measurements in PPMS. The samples are mounted on easily removable printed circuit boards. Each board provides gold pads for up to eight electrical connections in either 4-wire or 5-wire configurations. The samples were connected to external measurement circuits through 25-μm-thick gold wires with indium directly pressed on the contacting pads. For each data point of all measurements, averaging of three times was applied to reduce measurement noise.

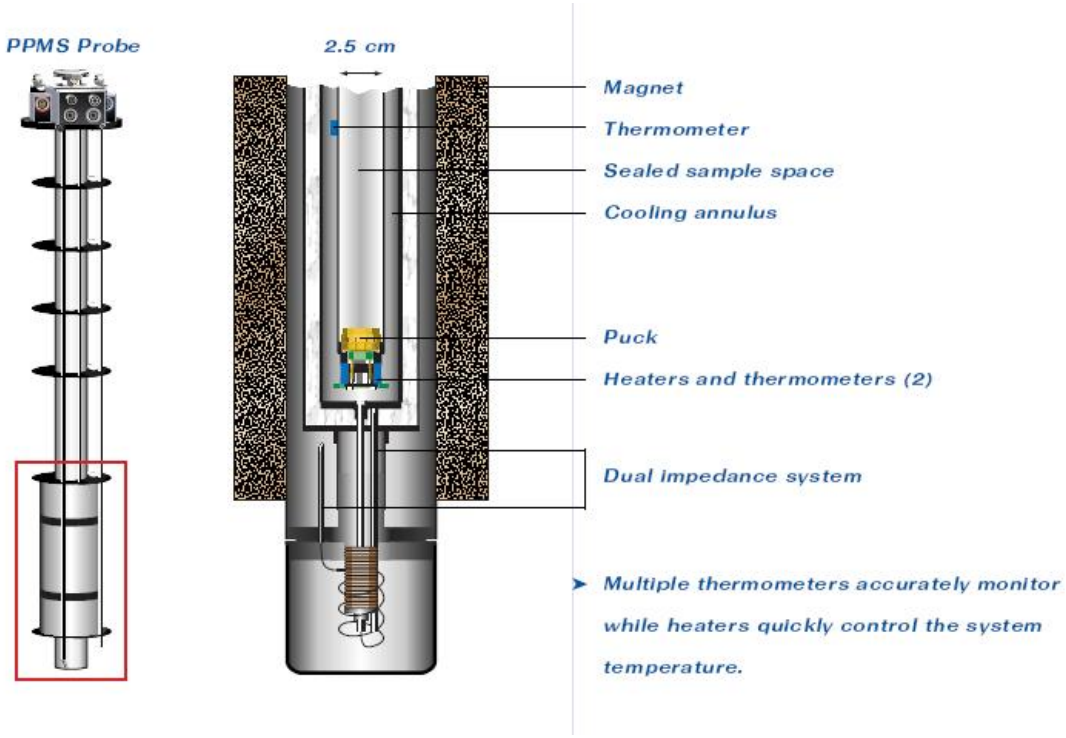

FIG 2.10. Schematics of the sample rod and puck setup in the dewar of the PPMS.

The combined VSM option in PPMS is a fast and sensitive DC magnetometer. The basic measurement is accomplished by oscillating the sample near a detection coil and synchronously detecting the voltage induced. This VSM linear motor transport uses a uniquely designed linear motor to vibrate the sample and the large range of motion enables the VSM system to perform rapid, completely automated centering operations.

2.4 Dielectric properties measurement

The dielectric properties of a material are permittivity and permeability, and represent its ability of storing energy when an external electric field is applied. As shown in Figure 2.11, when a DC voltage source is placed across a parallel plate capacitor, the dielectric material increases the storage capacity of the capacitor by neutralizing charges at the electrodes. The capacitance with the dielectric material is related to dielectric constant, and both of them can change with frequency, temperature, orientation, pressure and molecular structure of the material. The dielectric constant (k) is equivalent to relative permittivity or the absolute permittivity.

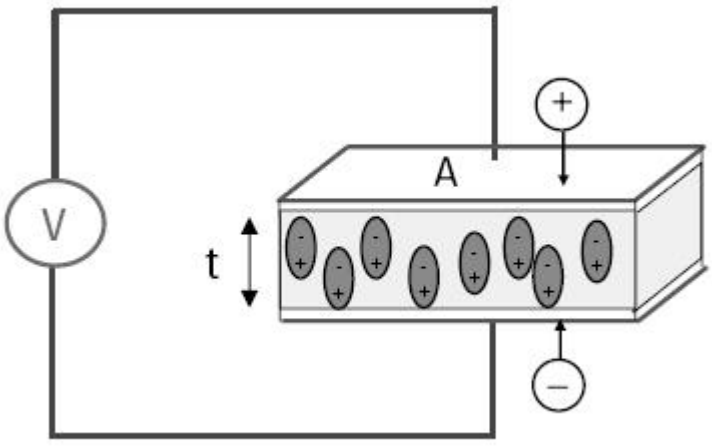

FIG 2.11. Schematic of a DC parallel plate capacitor.

A material may have several dielectric mechanisms or polarization effects that contribute to its overall permittivity. A dielectric material has an arrangement of electric charge carriers that can be displaced by an electric field. The charges become polarized to compensate for the electric field such that the positive and negative charges move in opposite directions.

The frequency-dependent capacitance and dielectric loss of device configurations of nanocomposite thin films in this dissertation were measured using an HP4194A impedance analyzer. The samples are stimulated with an AC source and the actual voltage across the material is monitored. Material test parameters are derived by knowing the dimensions of the material and by measuring its capacitance and dissipation factor.

2.5 Lift-off technique

The lift-off process in microstructuring technology is a method of creating structures (patterning) of a target material on a surface of a substrate using a sacrificial material. In this dissertation, we use lift-off process to grow Au patterns on top of nanocomposite thin films for electrical measurements. Figure 2.12 shows a processing sequence utilizing a positive resist. In order to reverse the tone of the image in the positive resist so that it functions as a negative resist, a so-called image reversal method is used in which after exposure the resist layer is subjected to amine vapors. The amine diffuses through the resist, and reacts with the dissolution enhancer

(carboxylic acid) photoproduct in the exposed areas. The process is conducted in a vacuum bake chamber, which allows the amine vapors to be uniformly delivered to the resist, and for the temperature to be uniformly controlled. Following the vapor treatment, the resist is flood exposed by UV light, and developed in a conventional manner.

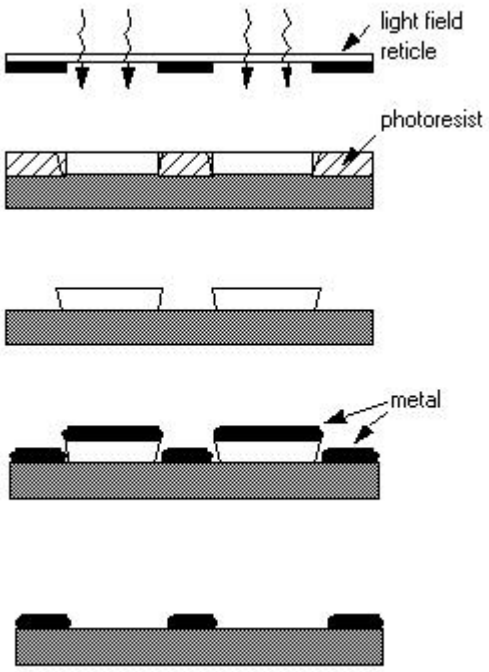

FIG 2.12. The lift-off process sequence utilizing positive photoresist.

The experimental facilities involved in the lift-off process include a spin processor (Laurell WS-650S) and a contact lithography printer (Quintel Q4000MA mask aligner). 3 um positive photoresist SC1827 will be first of all coated on nanocomposite thin films in the spin coater with a setting of 3000rpm, 60 seconds and 1000rpm acceleration speed. After 1min soft bake at 115°C, the sample is moved to the mask aligner and get contact to the chrome mask. Exposure will be done in the UV light with energy density of 350 mw/cm^2 for 7 seconds. The final top Au patterns can be deposited in the magnetron sputter with thickness around 80nm. The left photoresist can be removed with MF-319 photoresist developer for 60 seconds.

CHAPTER III

TUNABLE LATTICE STRAIN IN VERTICALLY ALIGNED NANOCOMPOSITE $(BiFeO_3)_x$:$(Sm_2O_3)_{1-x}$ THIN FILMS*

3.1 Overview

A unique epitaxial two-phase vertically aligned nanocomposite (VAN) $(BiFeO_3)_x$:$(Sm_2O_3)_{1-x}$ thin films were deposited on $SrTiO_3$ (001) substrates by pulsed laser deposition (PLD). The VAN thin films exhibit a highly ordered vertical columnar structure with high epitaxial quality. We demonstrate that the strains of the two phases in both out-of-plane and in-plane directions can be tuned by the deposition parameters during growth, e.g. deposition frequency and film composition of the nanocomposite. The strain tunability is found to be directly related to the systematic variation of the column widths in the nanocomposite. The dielectric property measurement shows that increasing vertical strain control will lead to a systematic dielectric loss reduction in the VAN thin films. This study suggests a promising avenue in achieving tunable strain in functional oxide thin films by using VAN structures.

*This chapter is reprinted with permission from "Tunable lattice strain in vertically aligned nanocomposite $(BiFeO_3)x$:$(Sm_2O_3)_{1-x}$ thin films" by Z. Bi, J. Lee, H. Yang, Q. Jia, J. L. Driscoll and H. Wang, Journal of Applied Physics 106, 094309 (2009). Copyright 2009 by American Institute of Physics.

3.2 Introduction

Nanocompositing two-phase structures have been recently introduced to achieve better materials functionality or multifunctionalities.[36,68,109] For example, vertical nanopillar structures were first demonstrated in $La_{0.7}Ca_{0.3}MnO_3$(LCMO):MgO system.[36] Following that, several nanocomposite structures with either nanolayers in $BaTiO_3$(BTO):$CoFe_2O_4$(CFO) system or nanopillars in BFO:CFO system were reported.[68,109] More interestingly, through vertically aligned nanocomposite (VAN) structure, unique vertical strain control was demonstrated in two-phase $BiFeO_3$ (BFO):Sm_2O_3 (SmO) nanocomposite systems.[100] BFO itself has attracted wide research interests recently because of its unique physical properties and potential applications in advanced memory and magnetoelectric devices.[109,7,148] This non-centrosymmetric rhombohedral perovskite shows the coexistence of ferroelectricity and antiferromagnetism, thus called multiferroic.[149,150] Because of the possible coupling between the magnetic and ferroelectric order parameters in BFO, the magnetization could be switched by applying an electric field, and the ferroelectric polarization can be switched by applying a magnetic field. Further more, polycrystalline BFO thin films have attracted extensive attentions recently due to its low cost and comparable properties.[151,152] Epitaxial BFO thin films have been successfully fabricated via various deposition techniques. [153,154,101,155] The film structure, especially the film strain in BFO films has been reported to be quite different, which results in a large variation in the physical properties of the films. For example, Cruz *et al.* reported that a film-substrate

misfit strain may result in a drastically different domain wall stability in epitaxial BFO(110) films by PLD and Lee *et al*. reported that electric fields can be used to control the populations of the equivalent magnetic domains in BFO single crystals via field-induced strain by neutron scattering. [156,157]

To maintain a good control of the strain in the BFO films, two-phase vertically aligned nanocomposites (VAN) architectures were introduced. VAN structures are interesting for achieving multifunctionality and also have the potential for enhancing a single functionality through manipulating the strain of one of the phases by another. As a secondary phase, SmO is introduced mainly because of its cubic structure with a bulk lattice parameter of 10.92Å. It is also an attractive candidate as the gate dielectric material in the CMOS devices [158,159] because of its high dielectric constant (7-15) and high chemical and thermal stability with Si. The vertical strain control in two-phase VAN structures has been demonstrated.[100] However, the fundamental growth mechanisms of the self-assembled VAN structures are not clear and the ways to effectively tune the vertical strain in the system have not yet been discovered.

In this work, we processed $(BFO)_x$:$(SmO)_{1-x}$ two-phase VAN thin films with different compositions x (A=0.5; B=0.6; and C=0.75) and deposition frequencies (Sample Set 1 at 1Hz; Set 2 at 2Hz; Set 3 at 5 Hz; and Set 4 at 10Hz), one of the most important deposition parameters during PLD growth. We conducted a detailed strain analysis in these VAN nanocomposite films as functions of film composition and deposition frequency, and correlated the strain with the two-phase domain structures. A

detailed dielectric property measurement was performed to explore the physical property variation as a function of the film strain.

3.3 Experimental

$(BFO)_x$:$(SmO)_{1-x}$ thin films were deposited on single crystal STO(001) substrates in a PLD system with a KrF excimer laser (Lambda Physik Compex Pro 205, λ= 248 nm). The laser beam was focused to obtain an energy density (1 Jcm^{-2}) at an incidence angle of 45°. The $(BFO)_x$:$(SmO)_{1-x}$ (with x=0.5, 0.6, and 0.75, indexed as A, B, and C, respectively) targets were prepared by a conventional powder mixing method. An optimized substrate temperature (650 ± 5°C) and an oxygen pressure of 0.2 torr were maintained during deposition. For this study, we control the film thickness around 40-60 nm to exclude the thickness effect on the VAN structure. Following deposition, the films were cooled down to room temperature in an oxygen pressure of 60 torr without any further thermal treatment.

The strain and microstructure of the as-deposited films were characterized by X-ray diffraction (XRD) (BRUKER D8 powder X-ray diffractometer), transmission electron microscopy (TEM) (JEOL 2010 analytical microscope with a point-to-point resolution of 0.23 nm) and scanning transmission electron microscopy (STEM) (FEI Tecnai G2 F20). A standard cross-section TEM sample preparation including manual grinding and thinning of sample with a final ion milling step (PIPS 691 precision ion polishing system, 3.7 KeV), was used. For transport property measurements, Pt electrodes with an area of 1×10^{-4} cm^2, defined by a standard lift-off lithograph process,

were deposited by sputtering. The frequency-dependent capacitance and dielectric loss of capacitors of device configurations Pt/BFO:SmO/Nb:STO were measured using an HP4194A impedance analyzer.

3.4 Results and discussion

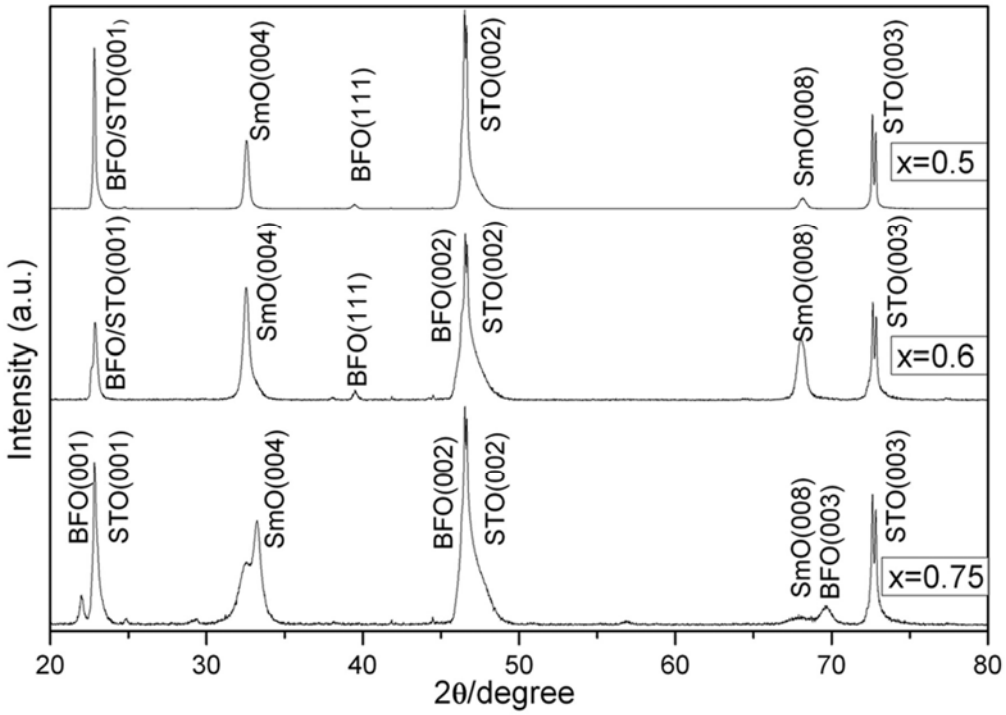

FIG. 3.1. XRD θ~2θ scans of $(BFO)_x$:$(SmO)_{1-x}$ thin films with different compositions (all deposited at 2Hz).

Figure 3.1 shows the XRD θ~2θ scans of samples A2, B2 and C2 all deposited at 2Hz. It is obvious that, for all cases, both BFO and SmO phases have grown highly textured along (00*l*) direction. For A2 (x=0.5) and B2 (x=0.6), all the BFO(00*l*) peaks overlap with STO(00*l*) peaks and a small BFO(111) peak is also present. For C2 (x=0.75), BFO(001) peak appears instead of overlapping with STO(001) peak as shown for the cases of A2 and B2. It is clear that, with higher BFO content, higher order of the BFO(00*l*) peaks start to show up following the decrease of SmO(008) peak. For example, for B2 (x=0.6) and C2 (x=0.75), BFO(002) and (003) peaks are clearly observed in Figure 3.1.

Based on the peak positions observed, the out-of-plane lattice parameters of BFO and SmO are calculated. The lattice parameters of BFO and SmO are 3.96Å and 10.92Å in bulk,[158,159] and, 4.05 Å and 10.87 Å in pure films deposited at our lab, respectively. In comparison, for all the x=0.5 and 0.6 films, BFO is in compression and SmO is in tension out-of-plane. If only the substrate lattice strain control (a_{STO}=3.91Å) was considered, BFO should be in compression in-plane and in tension out-of-plane, while SmO is expected to be in tension in plane (after 45° rotation) and in compression out-of-plane. The results are exactly opposite which suggests that the vertical strain control between the BFO and SmO phases is playing a dominant role in the binary VAN structures rather than the strain control from the underlying substrate.

More interestingly, the out-of-plane lattice parameter / strain is sensitive to the composition x and deposition frequency. Figure 3.2 a and c compare the local XRD pattern of BFO(001) as functions of BFO content for samples deposited at 2Hz and of

the deposition frequency for samples with x=0.5, respectively. It is obvious that BFO(001) peaks separated from STO(001) peak in most of the cases with either higher BFO contents or lower deposition frequencies. At lower BFO contents or higher deposition frequencies, BFO(00l) peak tends to overlap with STO(001). This suggests that, BFO (001) peak shifts towards lower angle, i.e., higher out-of-plane lattice parameter and closer to the bulk value, with either higher BFO content or at lower frequency. This also shows that the vertical compressive strain in BFO decreases and the BFO is more relaxed with either higher BFO content or at lower frequency. Figure 3.2 b and d compare the local scans of SmO(004) peak as functions of the BFO content and deposition frequency. For samples with x=0.75, as the frequency decreases, SmO(004) peak shifts towards higher angle, i.e., lower out-of-plane lattice parameter. However, there is no obvious SmO(004) peaks shifting with different deposition frequencies.

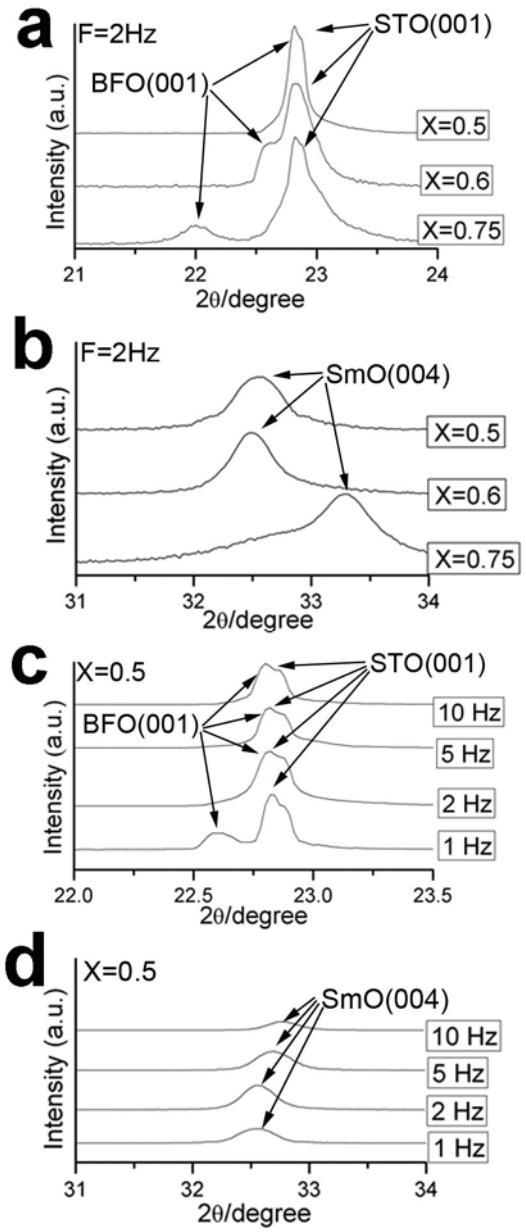

FIG. 3.2. Local XRD θ~2θ scans of a) BFO(001) peak and b)SmO(004) peak as a function of BFO content x; c)BFO(001) peak and d) SmO(004) peak as a function of deposition frequency.

To summarize above observations, we plot the out-of-plane lattice parameters of these two phases and the film strain (%) as a function of deposition frequency, and compare them with the bulk values in Figure 3.3 a and b, respectively. In all the films with x=0.5 and 0.6, they show obvious vertical strain control, i.e., BFO is in compression and SmO is in tension out-of-plane. The out-of-plane lattice parameter of BFO increases as the deposition frequency decreases, the out-of-plane lattice parameter of SmO keeps relatively constant possibly resulted by its rigid structure. However, in the films with x=0.75, only the ones deposited at higher frequencies (5Hz and 10Hz) shows the vertical strain control. The strain switches from vertical strain control to substrate strain control and approaches to the pure film value as the deposition frequency decreases. The overall trend is that, as the deposition frequency decreases or the BFO content increases, the out-of-plane lattice parameter of BFO increases and the strain switches from vertical strain control (in compression) (x=0.5 and 0.6) to substrate strain control (in tension) (x=0.75). On the other hand, the out-of-plane lattice parameter of SmO decreases and the strain switches from vertical strain control (tensile) (x=0.5 and 0.6) to substrate strain control (compression) (x=0.75). This suggests that both film composition and deposition frequency play a very important role in the overall strain control. When the film composition is in the neighborhood of x=0.5 or with higher deposition frequency, the strain in the VAN films is dominated by the vertical interface rather than the interface between the substrate and the film. However when the composition reaches a certain limit (e.g., x=0.75) or with lower deposition

frequency, the VAN structure lost its vertical strain control and the substrate strain control dominates the overall film strain.

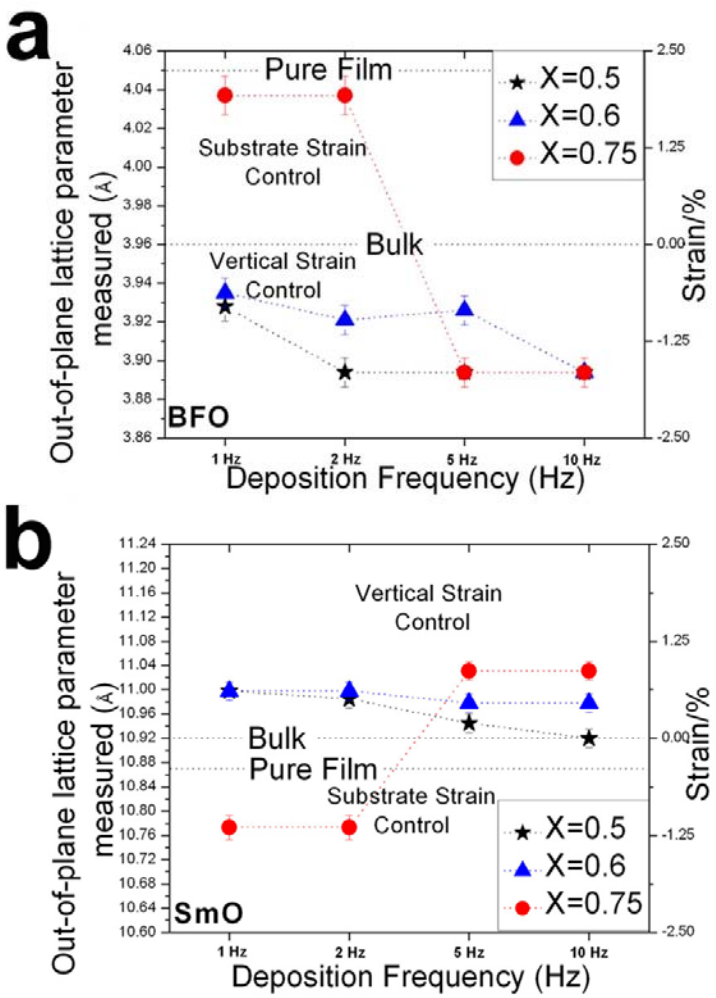

FIG. 3.3. Calculated out-of-plane lattice constants and out-of-plane strain versus deposition frequency for a) BFO and b) SmO, with different BFO contents in comparison with bulk lattice parameters.

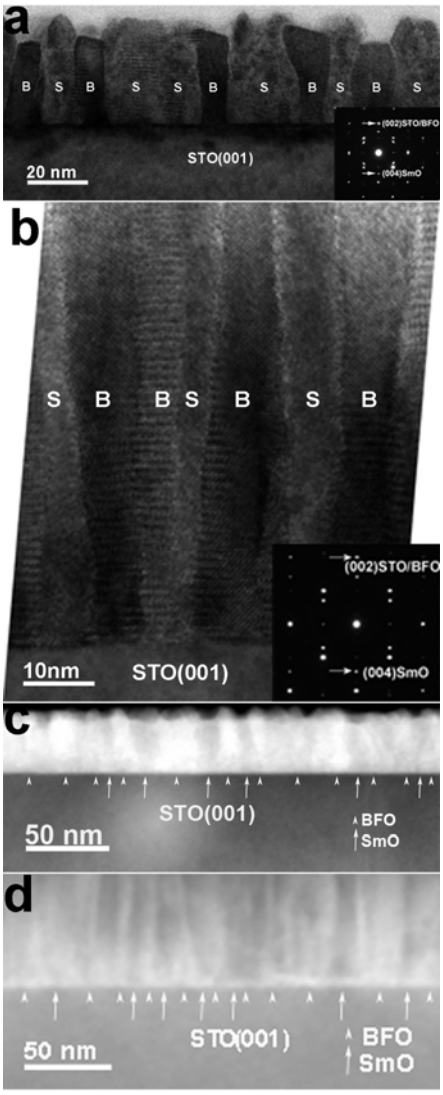

FIG. 3.4. Cross-section TEM images of (a) $(BFO)_{0.5}$:$(SmO)_{0.5}$ thin film(A1, deposited at 1Hz) and (b) $(BFO)_{0.6}$:$(SmO)_{0.4}$ thin film(B4, deposited at 10Hz) on STO(001) substrate. Insets are the corresponding selected-area diffraction patterns from both the film and the substrate. Cross-section STEM (Z-contrast) images of (c) $(BFO)_{0.5}$:$(SmO)_{0.5}$ thin film(A1, deposited at 1Hz) and (d) $(BFO)_{0.6}$:$(SmO)_{0.4}$ thin film(B4, deposited at 10 Hz) on STO(001) substrate. Columns with brighter contrast are BFO and columns with darker contrast are SmO.

The systematic variations in the VAN film strain is most likely related to the microstructure of the VAN structure. We conducted a detailed cross-section TEM investigation on all the samples deposited to fully understand the strain control in VAN structures. Figure 3.4 a and b show the cross-section TEM images of sample A1 (1Hz, x=0.5) and B4 (10Hz, x=0.6) respectively. In both cases, a clear vertically aligned columnar structure was observed. BFO and SmO phases/columns are alternating with each other. Both phases have grown epitaxially on STO substrate, evidenced by the distinguished diffraction dots from BFO and SmO phases in the corresponding selected area diffraction (SAD) patterns (as inset). The orientation relationships are determined to be BFO(002)// SmO(004) // STO(002) and BFO(200)// SmO(220)// STO(200).

One obvious difference between A1 (Figure 3.4 a) and B4 (Figure 3.4 b) is the VAN column/domain size. A1 has much wider column width than B4. This could be mainly due to the difference in deposition frequency. To systematically study the column/domain size variation over a large area, we conducted a detailed scanning transmission electron microscopy (STEM) study on all the samples. STEM under the high angle annular dark field (HAADF) condition, is also called Z-contrast imaging, where the contrast is approximately proportional to the square of the atomic number ($Z^{1.7}$).[160] Figure 3.4 c and d show the Z-contrast images of BFO/SmO VAN structures for A1 and B4, respectively. The most striking feature is the bright/dark columns that align alternatively in the lateral direction, indicating the presence of vertically aligned BFO and SmO columns. The BFO columns are much brighter than the SmO columns as the Z number of Bi (Z=83) is higher than that of Sm (Z=62). All the nanocolumns

are grown vertically through the film thickness without obvious column tilting. No obvious interface mixing was observed in the view areas. We also conducted detailed energy dispersive x-ray spectroscopy (EDX) mapping for both samples (not shown here) and confirmed the growth of BFO/SmO nanocomposites with the film composition predicted. No obvious intermixing between the BFO and SmO phases was detected by EDX scans (within the detection limits of EDX).

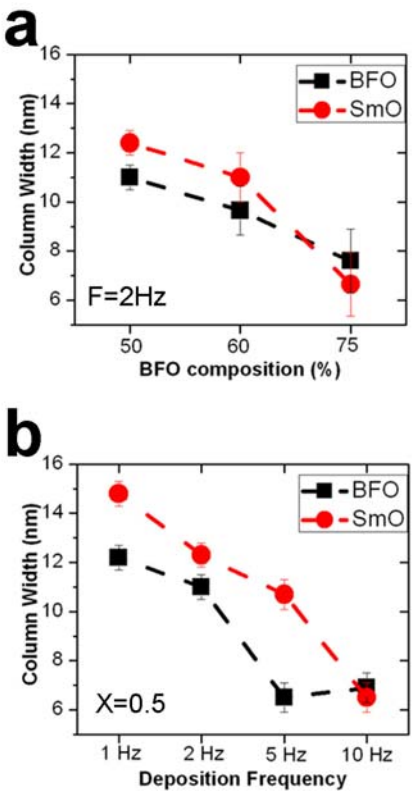

FIG. 3.5. Column width of $(BFO)_x$:$(SmO)_{1-x}$ composite thin films with different BFO contents and deposition frequencies. (a) F=2Hz; (b) x=0.5.

Based on both the TEM and STEM observations, we estimated the column/domain sizes for all the VAN samples. Figure 3.5 a and b plot the average column/domain size of BFO (black squares) and SmO (red circles), as functions of the BFO content and deposition frequency, respectively. We averaged the column size based on multiple low magnification TEM images and STEM images over large view areas. For Figure 3.5 a and b, it is clear that both BFO and SmO column widths increase as the BFO content increases or as the deposition frequency decreases. This can be understood through thin film growth kinetics. Lower deposition frequency results in longer resting time in between laser pulses and longer atomic diffusion path on top of substrate. This will cause larger nucleation island, i.e., larger column width. This observation can also explain the systematic variation of the out-of-plane compressive strain in BFO. As the frequency reduces, the BFO column width increases and the total amount of the vertical column boundaries reduces. These will cause the reduction in the vertical strain control in between BFO and SmO columns and therefore the out-of-plane compressive strain of BFO reduces.

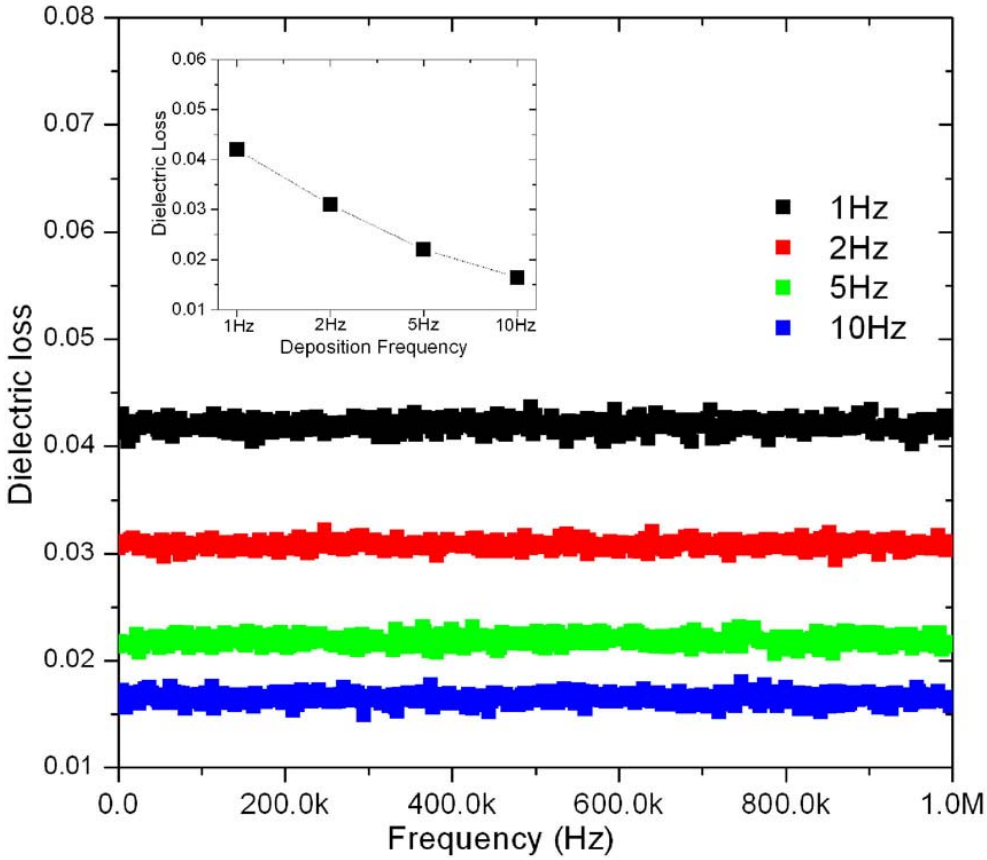

FIG. 3.6. Dielectric loss of $(BFO)_{0.5}$:$(SmO)_{0.5}$ thin films grown on conductive Nb-doped STO (Nb:STO) with different deposition frequencies.

More interestingly, a systematic variation in the physical properties of VAN structures was observed. As plotted in Figure 3.6, the dielectric loss of $(BFO)_{0.5}$:$(SmO)_{0.5}$ nanocomposites systematically decrease from 0.042 to 0.016 as the deposition frequency increases from 1Hz to 10Hz. The dielectric loss of pure BFO and

pure SmO films are around 0.055 and 0.03, respectively.[4] The dielectric loss for the BFO/SmO nanocomposite is mainly controlled by the BFO phase which has a higher dielectric loss. First, the BFO phase in all the nanocomposite films has lower dielectric loss than the pure BFO film which indicates that the vertical strain control has improved the overall dielectric properties. Second, the systematic reduction in the dielectric loss is believed to be attributed to the increase of the vertical strain control in the system. As the deposition frequency increases, the BFO columns are narrower and the vertical compressive strain in BFO phase increases, that result in the systematic reduction of the dielectric loss. This is the first demonstration on systematically tunning the physical properties of one phase using vertical strain control in VAN nanocomposites.

3.5 Conclusions

We have processed highly ordered epitaxial $(BFO)_x$:$(SmO)_{1-x}$ VAN thin films with various compositions and deposition frequencies on STO(001) substrates. In the films with x=0.5 and 0.6, they show obvious vertical strain control, i.e., BFO is in compression and SmO is in tension out-of-plane, at all deposition frequencies. However in the films with x=0.75, only the ones deposited at higher frequencies (5Hz and 10Hz) show the vertical strain control. The column width as well as the vertical strain can be varied systematically as functions of deposition frequency and film composition. As the deposition frequency decreases, the column/domain size increases

and the vertical strain control in both BFO and SmO decreases, i.e., the lattices of both phases approach their bulk values. As the BFO content increases, the column/domain size decreases and the vertical strain control in both BFO and SmO decreases. A systematic reduction in the dielectric loss of the BFO/SmO nanocomposites was observed as the deposition frequency increases, i.e., the column width decreases and the vertical strain control increases. All of the observations above suggest that the VAN structures have great potential in precise control of the overall film strain as well as the resulted materials functionalities.

CHAPTER IV

MICROSTRUCTURE AND MAGNETIC PROPERTIES OF $La_{0.7}Sr_{0.3}MnO_3$:Mn_3O_4 NANOCOMPOSITE THIN FILMS*

4.1 Overview

Epitaxial $(La_{0.7}Sr_{0.3}MnO_3)_{0.7}$:$(Mn_3O_4)_{0.3}$ (LSMO:Mn_3O_4) nanocomposite thin films were grown on $SrTiO_3$ (001) substrate by a pulsed laser deposition (PLD) technique. The nanocomposite structures vary from triangular domains, to vertically aligned columns, and finally to smaller spherical domains as the deposition frequency varies from 1 Hz, 5 Hz to 10 Hz, respectively. The strain in LSMO is systematically tuned but that of the Mn_3O_4 phase is relatively stable as the deposition frequency increases. The tunable strain is found directly related to the different domain and grain boundary (GB) structures. Physical properties including saturation magnetization, Curie temperature (T_c), magnetoresistance and metal-insulator transition temperature (T_{MI}), all show systematic trends as the deposition frequency varies. This study reveals that the domain/GBs tunability achieved in nanocomposite thin films can affect the lattice strain and further tune their ferromagnetic properties.

---

*This chapter is reprinted with permission from "Microstructural and magnetic properties of $(La_{0.7}Sr_{0.3}MnO_3)_{0.7}$:$(Mn_3O_4)_{0.3}$ nanocomposite thin films" by Z. Bi, E. Weal, H. Luo, A. Chen, J. L. Driscoll, Q. Jia, and H. Wang, Journal of Applied Physics 109, 054302 (2011). Copyright 2011 by American Institute of Physics.

4.2 Introduction

Mixed-valence perovskite manganites $R_{1-x}A_xMnO_3$ (R is rare earth and A is divalent cation) have attracted great research interests in the past decades.[161-163] Their intrinsic colossal magnetoresistance (CMR) and further more the low field magnetoresistance (LFMR) give great promises in device applications that require a large and temperature-independent magnetoresistance under small applied magnetic fields.[27,28,164] It has been demonstrated that the enhanced magnetotransport occurred at the grain boundaries (GBs) in polycrystalline perovskite manganites, where the magnetic spin alignment is obstructed and the spin-polarized tunneling happened.[165,166] Much work has been done to increase the GB areal density or the disordered regions at the GBs by incorporating an insulating oxide secondary phase.[167-172] However, the approaches on bulk composite samples usually comes with ion diffusion, large porosity and poor grain connectivity, and it is difficult to control the GBs.[167,173] Well-oriented nanocomposite thin films give more uniform properties as compared with that of polycrystalline films and bulk samples.[135,174] The reduced dimensionality in nanocomposite thin films provides a better control on the GBs and a great opportunity in tuning the GBs systematically. In addition, the magnetotransport in perovskite manganites, such as ferromagnetic $La_{0.7}Sr_{0.3}MnO_3$, is also strongly influenced by the microstructure and lattice distortion.[94,126,175,176] Little attention has been paid on the strain tuning of the manganite phase with different domain/GBs structures in the

composite, and the prior studies have mainly focused on either increasing the areal density of GBs or varying the composition of the secondary phase.

Certain unique nanostructured composite thin films can also achieve better material functionality or multifunctionalities.[68,106] As one of the outstanding representatives which has been extensively studied recently, vertically aligned nanocomposite (VAN) thin films provide a unique vertical strain control in two-phase nanocomposite thin films. In those systems, a single material functionality can be systematically enhanced through manipulating the strain of one of the phases by another.[100,103,114] The morphology and microstructure of the nanocomposite thin films, as well as their strain and material functionalities, can be varied by modifying the phase ratio, substrate orientation or deposition conditions.[177]

In this work, epitaxial $(La_{0.7}Sr_{0.3}MnO_3)_{0.7}$:$(Mn_3O_4)_{0.3}$ (LSMO:Mn_3O_4) nanocomposite thin films have been processed by pulsed laser deposition (PLD). Various nanocomposite structures have been achieved by adjusting the deposition frequency from 1Hz, 2Hz, 5Hz to 10Hz during PLD. Mn_3O_4 is a ferrimagnetic insulating oxide with much lower T_c as compared with that of LSMO thin film. We selected Mn_3O_4 as the secondary phase because it is chemically compatible with LSMO and will not affect the stoichiometry of the manganite phase in the nanocomposite thin film. On the other hand, placing a ferrimagnetic material in contact with the ferromagnetic phase may modify the magnetic behavior of the later one from the interaction at the ferromagnet-ferrimagnet interface. The magnetic and

magnetotransport properties of $(LSMO)_{0.7}$:$(Mn_3O_4)_{0.3}$ nanocomposite thin films were measured and compared based on their different domain and GBs structures.

4.3 Experimental

$(LSMO)_{0.7}$:$(Mn_3O_4)_{0.3}$ nanocomposite thin films were deposited on $SrTiO_3$ (STO) (001) substrates in a PLD system with a KrF excimer laser (Lambda Physik Compex Pro 205, λ=248nm). The laser beam was focused to obtain an energy density of 4 $J \cdot cm^{-2}$ at an incidence angle of 45°. The $(LSMO)_{0.7}$:$(Mn_3O_4)_{0.3}$ ceramic target was made by mixing La_2O_3, Mn_2O_3 and Sr_2O_3 powders (99.99%) in proper ratios and following multiple steps of standard solid state reaction processes. An optimized substrate temperature of 750°C and an oxygen gas pressure of 200 mtorr were maintained during the deposition. The film thickness was maintained at 120 nm in this study. The deposition frequency was varied from 1Hz, 2Hz, 5Hz to 10Hz. The microstructure of the films was examined using X-ray diffraction (XRD) (BRUKER D8 X-ray diffractometer), transmission electron microscopy (TEM) (JEOL 2010 analytical microscope) and scanning transmission electron microscopy (STEM) (FEI Tecnai F20 analytical microscope). The magnetization and magnetoresistance of $(LSMO)_{0.7}$:$(Mn_3O_4)_{0.3}$ nanocomposite thin films were measured using a vibration sample magnetometer (VSM) (Princeton Measurement Corporation) and a physical properties measurement system (PPMS) (Quantum Design, Inc.), respectively.

4.4 Results and discussion

Figure 4.1a shows the XRD θ-2θ scans for the $(LSMO)_{0.7}$:$(Mn_3O_4)_{0.3}$ nanocoposite thin films deposited at different frequencies. Both phases have grown highly textured on STO(001) substrates. The LSMO(002) peak shows up at higher deposition frequencies (5Hz and 10Hz) instead of overlapping with the STO(002) K_β substrate peak as the samples deposited at lower deposition frequencies (1Hz and 2Hz). As the deposition frequency increases, the LSMO(002) peak shifts to higher 2θ positions and the out-of-plane lattice parameter of LSMO phase decreases as seen in Figure 4.1b and c, respectively. The secondary cubic Mn_3O_4 phase was stable and no obvious peak shifting was observed as the deposition frequency varies. Different from other epitaxial LSMO films grown by PLD,[173,176,178] above XRD result reveals that a systematic lattice distortion can be achieved by adjusting the deposition frequency while having the secondary phase stable in the nanocomposite thin films.

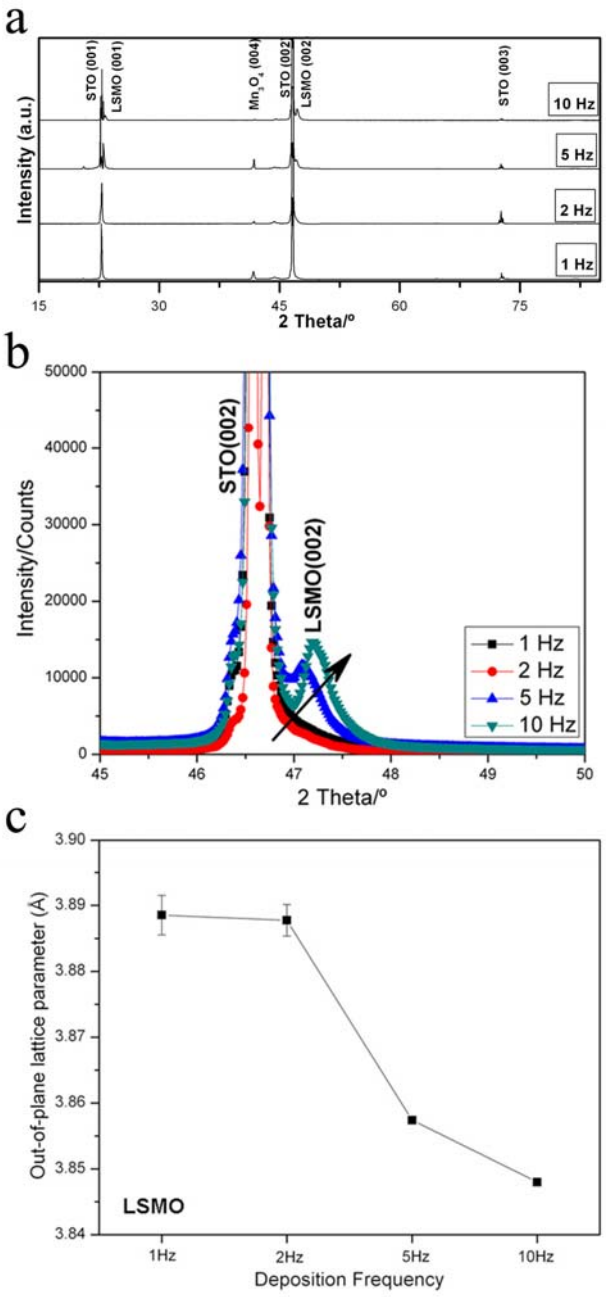

FIG. 4.1. a) XRD θ-2θ scans of $(LSMO)_{0.7}$:$(Mn_3O_4)_{0.3}$ thin films with different deposition frequencies. b) Local XRD θ-2θ scans show LSMO (002) peak shifting from lower to higher 2θ angles. c) Out-of-plane lattice parameter of LSMO phases varies as a function of the deposition frequency.

Further microstructure analysis and phase structure identification of $(LSMO)_{0.7}$:$(Mn_3O_4)_{0.3}$ nanocomposite thin films have been performed using cross-section high resolution TEM (Figure 4.2) and STEM (Figure 4.3). The composition of LSMO and Mn_3O_4 phases in the deposited thin films with different deposition frequencies was maintained at 70:30 verified by the energy dispersive X-ray (EDX) in TEM (not shown here). In PLD, the deposition frequency has been demonstrated to be an important factor that affects the microstructures of nanocomposite films.[114] The sample deposited at 1Hz shows reversed alternating triangular LSMO domains with the zig-zag Mn_3O_4 phases embedded in between with a width of 5 nm (Figure 4.2a and b). While with a higher deposition frequency of 2Hz, both phases form smaller domain structures and start to lose their original domain shapes at 1Hz. It is interesting to see that at a higher deposition frequency of 5Hz, both LSMO and Mn_3O_4 phases show vertically aligned columnar domain structure. Two phases are alternating with each other and the column widths are around 20 nm and 5 nm, respectively (Figure 4.2d).

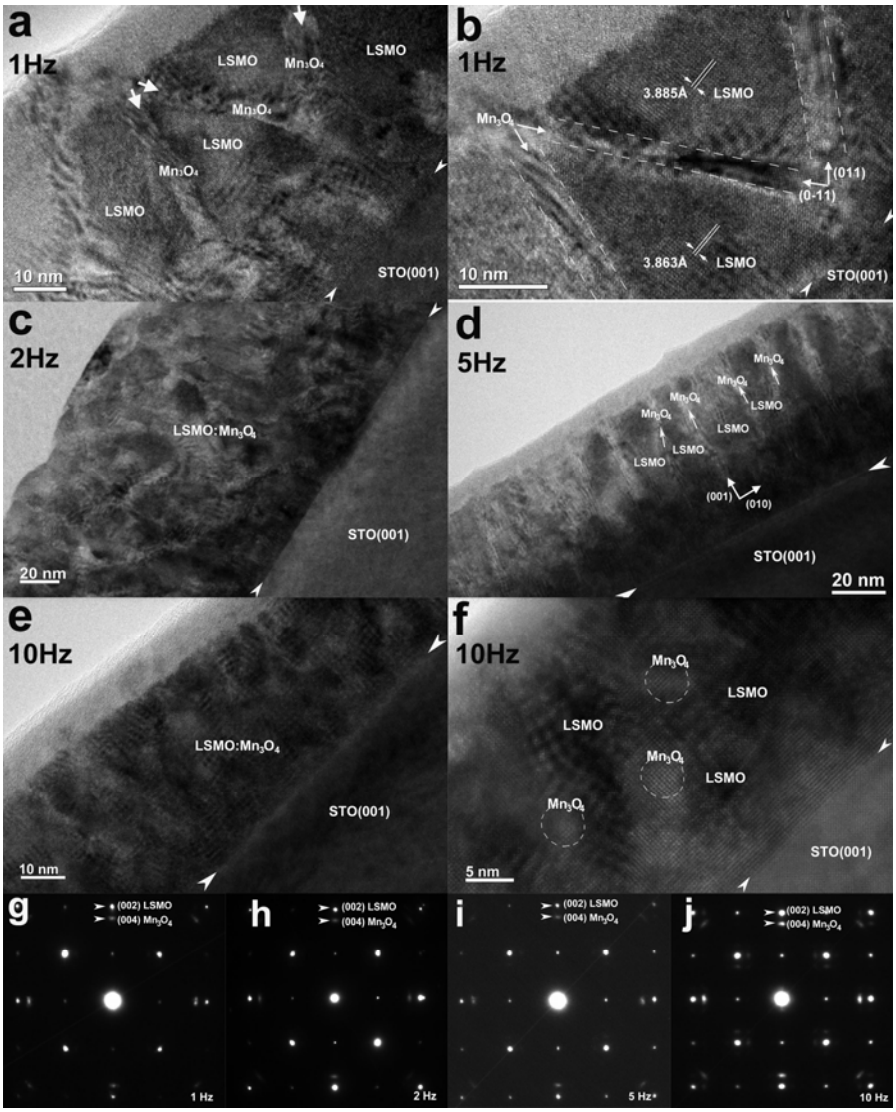

FIG. 4.2. Cross-section TEM images of $(LSMO)_{0.7}$:$(Mn_3O_4)_{0.3}$ nanocomposites. a) and b)1Hz deposited sample with triangular domains; c) 2Hz deposited sample shows distorted structure; d) 5Hz deposited sample shows vertically aligned columnar growth of both phases; e) and f) 10Hz deposited sample shows spherical shape Mn_3O_4 domains embedded in LSMO thin film. g) to j) selected area diffraction patterns (from the film only region) for 1Hz, 2Hz, 5Hz and 10Hz deposited $(LSMO)_{0.7}$:$(Mn_3O_4)_{0.3}$ nanocomposite samples, respectively.

Figure 4.2e and f show that the 10Hz deposited sample has lost its former vertically aligned columnar structure and the Mn_3O_4 phase grows as spherical shape domains embedded in the LSMO epitaxial thin film matrix. The secondary Mn_3O_4 phase only shows cubic lattice structure instead of the hausmannite structure on single crystal STO substrate which reveals a weaker substrate strain control of the nanocomposite film.[179] Regardless of the deposition frequency, all the samples have grown highly epitaxially on STO substrate evidenced from the distinguished diffraction dots in the selected area diffraction (SAD) patterns (Figure 4.2 j to i) taken from the film region for all the samples. The nanocomposite thin film and substrate orientation relationships are determined to be LSMO(002)//Mn_3O_4(004)//STO(002) and LSMO(020)//Mn_3O_4(220)//STO(020) for all the samples.

To further confirm the phase distribution in nanocomposite thin films, we conducted a detailed STEM study on the 1Hz and 5Hz deposited samples as shown in Figure 4.3 a and b, respectively. In STEM (also called Z-contrast imaging), LSMO shows a brighter contrast (Z_{La}=57) and Mn_3O_4 shows a darker contrast (Z_{Mn}=25) due to their different atomic numbers. The triangular LSMO and zig-zag shaped Mn_3O_4 domains for the 1 Hz sample, and the vertically columnar growth of both phases for the 5 Hz sample can be clearly distinguished from Figure 4.3a and b, respectively. Further more, the EDX line scan across the LSMO and Mn_3O_4 domains shows obvious oscillations in intensities for La and Sr, suggesting La and Sr-rich and deficient regions, but stable intensities for Mn and O. This confirms the compositions of the triangular domain structure and zig-zag GBs shape, which are also consistent with TEM results.

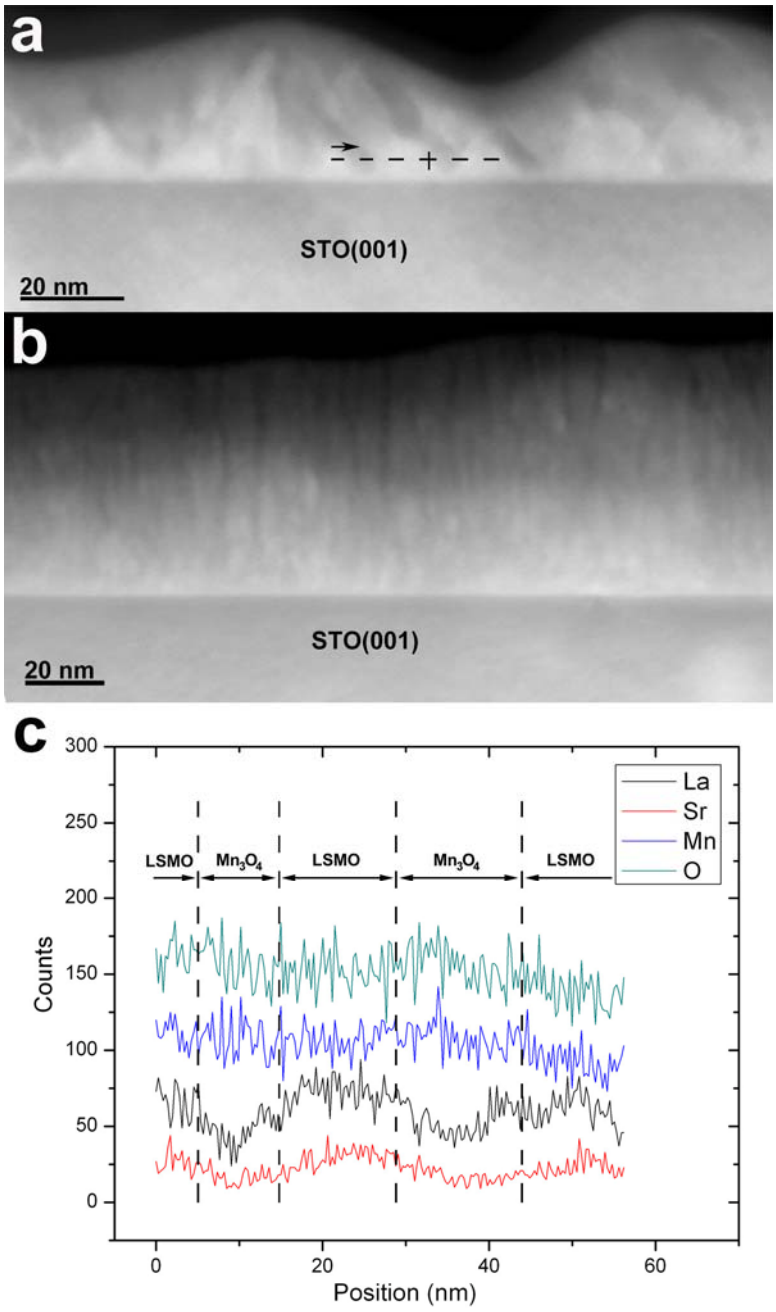

FIG. 4.3. Cross-section STEM images of a)1Hz and b)5Hz deposited $(LSMO)_{0.7}$:$(Mn_3O_4)_{0.3}$ nanocomposite thin films, respectively. c) EDX line scan across the LSMO and Mn_3O_4 domains in 1Hz deposited sample, the oscillating La- and Sr-profiles demonstrate the elemental intensity variations at different regions.

The above electron microscopy study on the nanocomposite thin films demonstrates that the film microstructure as well as the GB shape can be varied by tuning the deposition frequency during growth. The deposition frequency corresponds to the flux density of adatoms arriving on top of the substrate, and adjusting it could cause a competition between the film growth kinetics and the thermodynamic limitations. For pure LSMO thin films, the lattice parameter is a_{LSMO}=3.86Å, and if only the substrate lattice strain control (a_{STO}=3.91 Å) was considered, pure LSMO should be in tension in plane and in compression out of plane. In this work, the strain tuning of LSMO in the $(LSMO)_{0.7}$:$(Mn_3O_4)_{0.3}$ nanocomposite thin films is mainly caused by different domain structures with various deposition frequencies. As shown in Figure 4.2b, with lower deposition frequency at 1Hz, the out-of-plane lattice matching between LSMO and Mn_3O_4 phases prefer to be along the [011] directions where the domain interfaces lie in. The substrate-induced strain control only exists in the upright triangular LSMO domains on the bottom but not the inverted ones on top. Figure 4.2b demonstrates that the top inverted triangular LSMO domains do not show obvious substrate induced tension in-plane and less out-of-plane lattice distortions (c=3.885Å) as compared with that of the bottom ones (c=3.863Å). With higher deposition frequency at 5Hz, both LSMO and Mn_3O_4 phases grow epitaxially on STO(001) substrate as vertically aligned columns. In this case, the substrate induced strain in LSMO plays a more effective role than the 1Hz case, which results in an enhanced out-of-plane compression and a peak shift in the XRD pattern. The 10Hz deposited sample is very similar to the case of an epitaxial LSMO film but with Mn_3O_4 sphere domains

embedded in. It shows a stronger substrate strain control as compared with samples deposited at lower frequencies. Meanwhile, different GBs shapes, the domain boundary switching from [011] to [001] directions and further to the spherical shapes, may also introduce an extra compression out-of-plane to the LSMO phase with different lattice matching between LSMO and Mn_3O_4 phases.

The temperature dependence of magnetization for nanocomposite thin films deposited at different frequencies is shown in Figure 4.4a. Epitaxial pure LSMO film is ferromagnetic with Curie temperature (T_c) around 340K ~ 360K depending on different substrates and the T_c of pure Mn_3O_4 film is around 50K.[94,180] The hybrid nanocomposite manganites show the decreased T_c from 360K to 330K as the deposition frequency increases. As shown in the inset, the splitting of field cooling (FC) and zero field cooling (ZFC) curve at 50K for the 1Hz (in black) and 2Hz (in red) films suggests that the secondary Mn_3O_4 phase will only play a role at lower temperature regimes (T<50K). However the splitting is not observed in the highly strained films (deposited at 5Hz and 10Hz), and this may be correlated to the strain relaxation in nanocomposites deposited at lower frequencies. Similar to pure LSMO thin film, the $(LSMO)_{0.7}$:$(Mn_3O_4)_{0.3}$ nanocomposite thin films reveal magnetic anisotropy evidenced by hysteresis loop of 1Hz deposited nanocomposite in Figure 4.4b. It shows in-plane preferred magnetization as compared with that of out-of-plane. The magnetization of the nanocomposite is calculated based on the volume of the nanocomposite thin film.

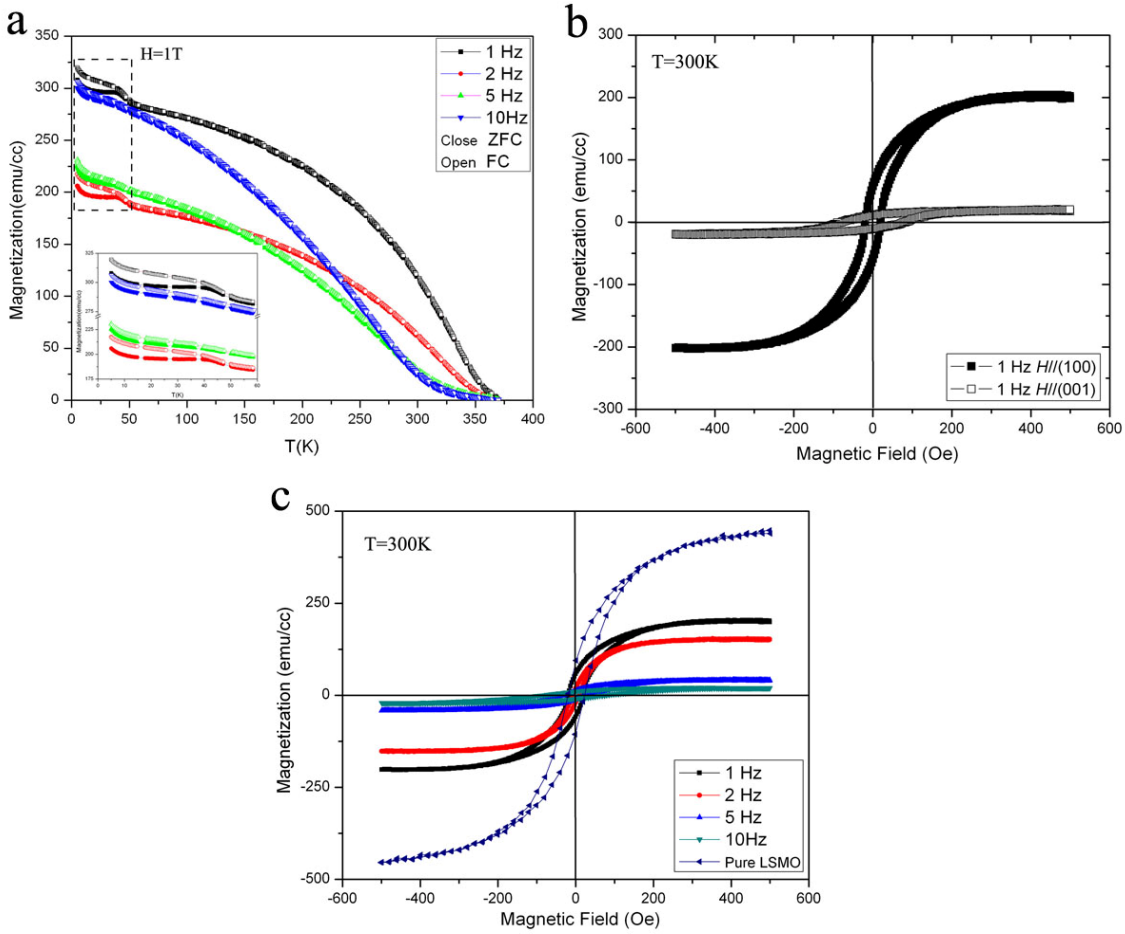

FIG. 4.4. a) The ZFC (close symbols) and FC (open symbols) magnetization vs. temperature for $(LSMO)_{0.7}:(Mn_3O_4)_{0.3}$ nanocomposites deposited at different deposition frequencies. The measurements were under a magnetic field of 1T applied along [100] direction; b) the hysteresis loop for the 1Hz deposited $(LSMO)_{0.7}:(Mn_3O_4)_{0.3}$ nanocomposite along [001] and [100] directions; c) hysteresis loops recorded at 300K for nanocomposite samples deposited at different frequencies, with field along [100] direction.

Figure 4.4c plots the magnetic hysteresis loops at 300K for the pure LSMO film and the $(LSMO)_{0.7}$:$(Mn_3O_4)_{0.3}$ nanocomposites deposited at different frequencies. It is interesting to note that the 1Hz deposited nanocomposite sample shows a compatible saturation magnetization as compared with that of the pure LSMO film if the LSMO composition is considered. More importantly, a systematic decrease in the saturation magnetization is observed as the deposition frequency increases. The magnetic properties of perovskite manganites can be strongly influenced by the microstructure and lattice distortion.[2,17,18] The systematic tuning in the saturation magnetization of the $(LSMO)_{0.7}$:$(Mn_3O_4)_{0.3}$ nanocomposites is believed to be attributed to the enhanced substrate strain control in the LSMO phase and the decreased LSMO domain size as the deposition frequency increases. With the relaxation of out-of-plane compression strain in LSMO as the deposition frequency decreases, the center MnO_6 octahedra in LSMO will be elongated which results in a tetragonal distortion of the lattice.[161,162,181] This distortion will cause longer (Mn-O) bond lengths and smaller (O-Mn-O) bond angles in the pervoskite, which will further affect the electron transport properties in manganites such as saturation magnetization. Second, following with the domain structure changes from triangular shape, vertically aligned columns to spherical shape as increasing the deposition frequency, the LSMO domain size decreases as seen in Figure 4.2. Smaller LSMO magnetic domains can be easily aligned parallel to the external magnetic field as compared with the larger ones deposited at lower frequencies. The systematic decrease of domain size also contributes to a smaller saturation magnetization in the nanocomposite thin films.

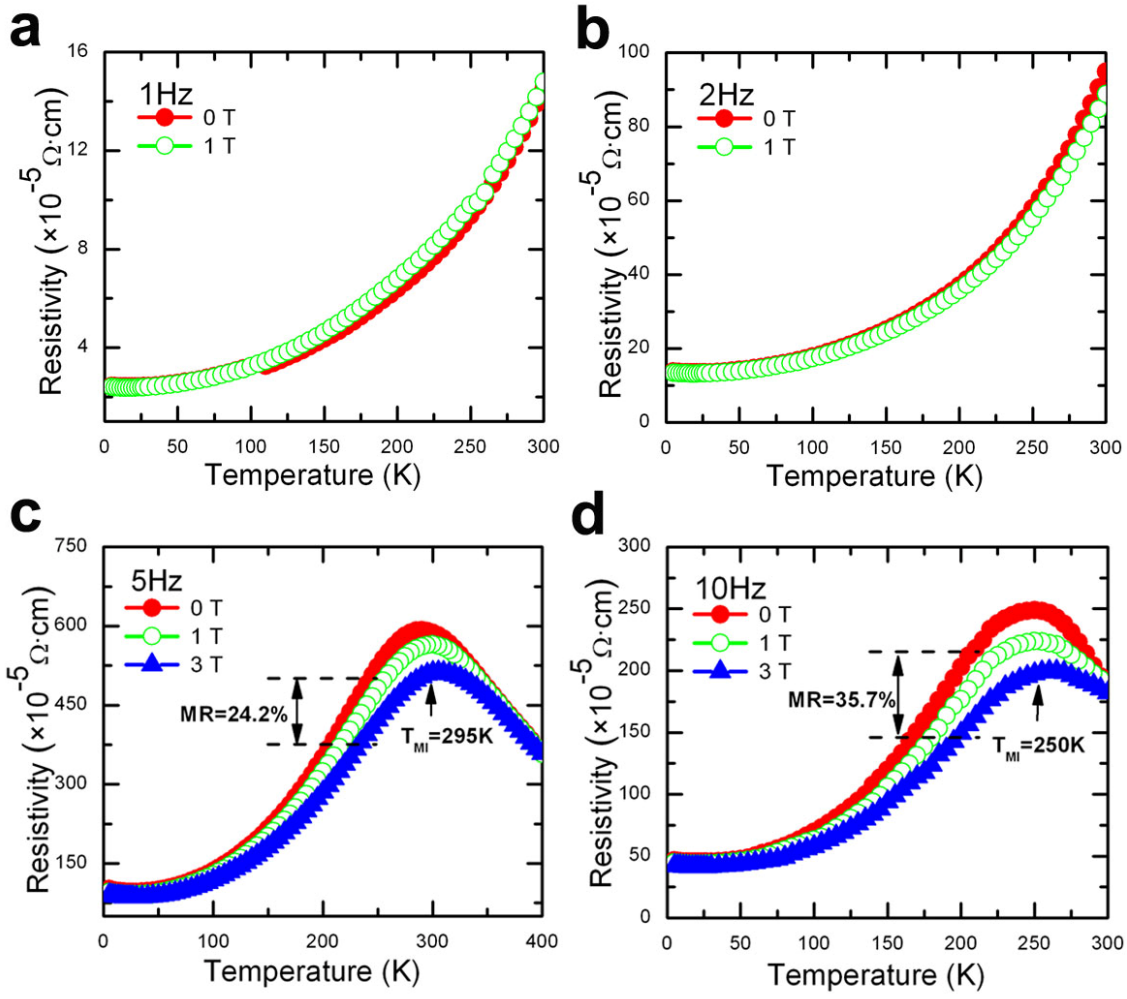

FIG. 4.5. Magnetoresistivity measurement on $(LSMO)_{0.7}$:$(Mn_3O_4)_{0.3}$ nanocomposite thin films with different deposition frequencies. a)1Hz; b)2Hz; c)5Hz; d)10Hz. The applied magnetic filed is up to 3T.

To investigate the lattice distortion and GB effect on the magnetotransport properties, the temperature dependence of in-plane resistivity for nanocomposite thin

films has been measured under magnetic field up to 3T as shown in Figure 4.5. LFMR was not observed in the well-crystallized LSMO:Mn_3O_4 nanocomposites since it always associated with wide angle grain boundaries which usually do not exist in epitaxial thin films.[177,181] First of all, the resistivity of the LSMO:Mn_3O_4 nanocomposite thin films is compatible with pure LSMO thin films ($10^{-3}\Omega\cdot$cm) and related to different secondary insulators in the nanocomposites (eg. LCMO:MgO~$10^{-3}\Omega\cdot$cm; LSMO:ZnO~$10^{-1}\Omega\cdot$cm).[36,37] Second, the increased resistivity (~$10^{-5}\Omega\cdot$cm for 1Hz and 2Hz; ~$10^{-3}\Omega\cdot$cm for 5Hz and 10Hz) as increasing the deposition frequency would be attributed to the different domain structures. The zig-zag Mn_3O_4 domain shape at lower deposition frequencies (1Hz and 2Hz) yields broader current flowing paths, as compared with that of the columnar domains at higher deposition frequency (5Hz) which build a network of two phases with columnar separation. The metal-insulator transition temperature (T_{MI}) for pure LSMO thin film grown on STO can reach up to 350K.[181] In general, the T_{MI} of the manganite-insulator composite will not coupled to T_c and is much lower than that of the pure LSMO film due to the obstructed magnetic spin alignment near the GBs and static disorder. Figure 4.5a and b show the temperature dependence of resistivity for samples deposited at 1Hz and 2Hz, respectively. Under the applied magnetic field of 1T, there is no obvious magnetoresistance and metal-insulator transition below 300K for both samples. For samples deposited at 5Hz and 10Hz (Figure 4.5c and d), increased magnetoresistance (MR) of 24.2% (5Hz) and 35.7% (10Hz) was observed under the magnetic field of 3T, accompanied by a decrease of the T_{MI} at 295K and 250K, respectively. The systematic

tuning on MR and T_{MI} is attributed to the lattice distortion of LSMO as the deposition frequency varies. On the other hand, the insulating Mn_3O_4 near GBs obstructs magnetic spin alignment and the enhanced MR is also correlated to the increased GB areal density in the nanocomposite thin films as the GB shape changed from zig-zag ones (1Hz) to vertically columnar ones (5Hz) and to spherical ones (10Hz).

4.5 Conclusions

In summary, epitaxial $(LSMO)_{0.7}$:$(Mn_3O_4)_{0.3}$ nanocomposite thin films have been grown on STO(001) substrates by PLD. Deposition frequency has been demonstrated to play an important role in the nanocomposite film microstructure and domain shapes. As the domains changed from triangular shape, to vertically columnar structure, and to spherical shape, the areal density of GBs increased and the out-of-plane compression strain increased in the perovskite LSMO phase. Different domain and GBs structures cause the lattice distortion in the LSMO phase, which systematically tunes the magnetic properties of the $(LSMO)_{0.7}$:$(Mn_3O_4)_{0.3}$ nanocomposite thin films. Meanwhile, different areal density of GBs also affects the magnetotransport properties in the nanocomposite thin films.

CHAPTER V

MICROSTRUCTURAL AND MAGNETIC PROPERTIES OF Mn_3O_4 THIN FILMS

5.1 Overview

Epitaxial and highly textured Mn_3O_4 thin films were grown on $SrTiO_3$ (STO) (001) single crystal substrates by pulsed laser deposition. In this work, we varied the oxygen pressure from vacuum to 200 mtorr to explore its effects on film microstructure, crystallinity, ferromagnetic response, as well as the competition between thin film growth kinetics and thermodynamic limitations. The film crystallinity and microstructure were characterized by transmission electron microscopy (TEM), scanning electron microscopy (SEM) and X-ray diffraction (XRD). X-ray photoelectron spectra (XPS) and vibrating sample magnetometer (VSM) in a physical properties measurement system (PPMS) were used to characterize the phase composition/ionic states and magnetic properties, respectively. It is found that Mn_3O_4 thin films deposited at 50 mtorr oxygen pressure show better crystallinity, higher Curie temperature (T_c) at 50K and similar saturation magnetization of 200emu/cc as compared with earlier literature reports.

5.2 Introduction

Recently Mn_3O_4 has attracted increasing research interests for its growing applications in electronic and magnetic related areas such as electrochemistry, molecular adsorption, catalyst and soft magnetic materials.[182-185] The stable room-temperature crystal structure of Mn_3O_4 is identified as c-axis distorted tetragonal hausmanite (space group 141/amdZ(141)) while crystallized as a spinel structure.[186] With the Manganese oxide ions close packed as cubic structure, Mn^{2+} ions occupy the tetrahedral sites, and Mn^{3+} ions occupy the octahedral sites. It is the Mn^{3+} ions that induce microdistortion to the cubic spinel structure by a cooperative Jahn-Teller effect at higher temperature.[187,188] As a model of spinel structure for experimental and theoretical investigations, Mn_3O_4 thin films, which can be essentially different from the bulk material, have shown many unique properties because of substrate-induced strain, structural defects, interface, and morphological effects.[189,190] With different ionic states (Mn^{2+}, Mn^{3+} and Mn^{4+}), various film stoichiometries (e.g., MnO, MnO_2, Mn_2O_3 and Mn_3O_4) and different crystal structures are resulted. Therefore the variation in thin film deposition parameters may lead to large differences in film qualities and physical properties. For example, oxygen pressure is one of the key factors in epitaxial oxide thin film growth due to its strong impacts on film microstructure, crystallinity, film composition and surface morphology. It has been demonstrated that the surface morphology of Al-doped ZnO(AZO, 2 wt%) thin films varied from a uniform layer to nanorod structure by simply controlling the oxygen pressure during growth. Similar

effects were also found in other oxide thin films.[191-193] Various vacuum-based techniques have been employed in the Mn_3O_4 thin film growth, such as atomic layer deposition,[194,195] molecular beam epitaxy (MBE),[180,196] pulsed laser deposition(PLD),[197] and metal-organic chemical vapor deposition (MOCVD).[198,199] However, very few or no report was on the effects of growth parameters on the film microstructure and magnetic properties.

In this work, high quality Mn_3O_4 thin films were processed by PLD on single crystal $SrTiO_3$ (STO) (001) substrates. A systematic study has been made by adjusting the oxygen pressure from vacuum (~1.0×10^{-6} mtorr) to 200mtorr. We observed a strong influence of the oxygen pressure on the film microstructural and magnetic properties.

5.3 Experimental

Mn_3O_4 thin films were deposited on STO (001) single crystal substrates in a PLD system with a KrF excimer laser (Lambda Physik Compex Pro 205, λ= 248 nm). The laser beam was focused to obtain an energy density of 4 J·cm^{-2} at an incidence angle of 45°. The Mn_3O_4 polycrystalline target was prepared by a conventional powder processing method as solid state reaction followed with target sintering under flowing oxygen at 1100°C for 10 hours. An optimized substrate temperature (750 ± 5°C) were maintained during deposition. The film thickness was controlled at 50 nm in this study. The oxygen pressure during deposition was varied from vacuum (~1.0×10^{-6}mtorr), 50 mtorr to 200 mtorr. No post-deposition annealing was performed on the samples.

The microstructure of as-deposited thin films was characterized by X-ray diffraction (XRD) (Rigaku Smartlab thin film X-ray diffractometer), scanning electron microscope (SEM) (JEOL JSM-7500F equipped with a high brightness conical field emission gun and a low aberration conical objective lens) and high resolution transmission electron microscope (TEM) (JEOL-2010 equipped Gatan ORIUS CCD camera with a point resolution of 2.34Å). A standard cross-section TEM specimen preparation procedure was used including manual grinding and thinning of sample followed by a final ion milling step using precision ion polishing system (PIPS 691) at 3.7 KeV. X-ray photoelectron spectrometer (XPS) (Kratos Axis Ultra Imaging XPS) was used for the ionic states analysis. The sample magnetic properties such as magnetization and hysteresis loops were measured by vibrating sample magnetometer (VSM) attached on a physical property measurement system (PPMS, Quantum Design).

5.4 Results and discussion

The epitaxial growth of Mn_3O_4 thin film on STO substrate comes from lattice matching of two face-centered-cubic (FCC) lattice structures with the bottom oxygen ions in Mn_3O_4 and top Sr cations in STO lying on the film/substrate interface.[179] Oxygen pressure could play a critical role in achieving heteroepitaxial growth of Mn_3O_4 thin films on STO(001) substrates. XRD was first conducted (shown in Figure 5.1) to explore the crystallinity variation introduced by different oxygen pressures during PLD. The sample deposited in vacuum shows weak Mn_3O_4 phase as the Mn_3O_4 (004) peak intensity is very low. However no other film phases were detected which

indicates the formation of textured Mn_3O_4 films. As the oxygen pressure increased to 50 mtorr, Mn_3O_4 shows epitaxial film growth as the (004) peak intensity increased and the value of full width at half maximum (FWHM) reduced from 0.18º to 0.11º. It is also worth to note that higher oxygen pressure results in the formation of a second phase, i.e., Mn_2O_3, as indicated by the increasing intensity of Mn_2O_3 (004) peak as oxygen pressure increases. But in the case of 50 mtorr, Mn_3O_4 is the dominant phase with improved crystallinity as compared with the one deposited in vacuum. With even higher oxygen pressure at 200 mtorr, XRD shows polycrystalline film quality, both Mn_3O_4 and Mn_2O_3 phases exist and the Mn_2O_3 phase become the dominant one. At the mean time, MnO phase shows up and textures as (021). The XRD patterns illustrate that the oxygen pressure during deposition play a dominant role in achieving desired MnO_x crystal structures as well as Mn ionic states. i.e., proper oxygen atmosphere is required for growing high quality pure Mn_3O_4 phase.

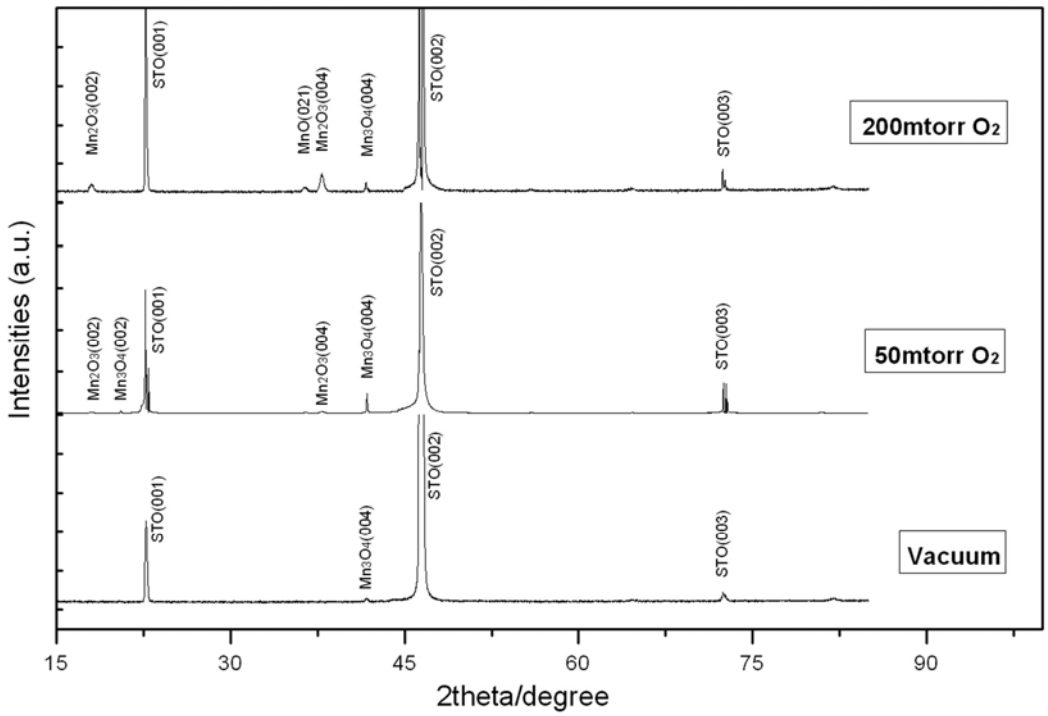

FIG. 5.1. XRD patterns of Mn_3O_4 thin films under different deposition oxygen pressures (in vacuum, 50mtorr and 200mtorr, respectively).

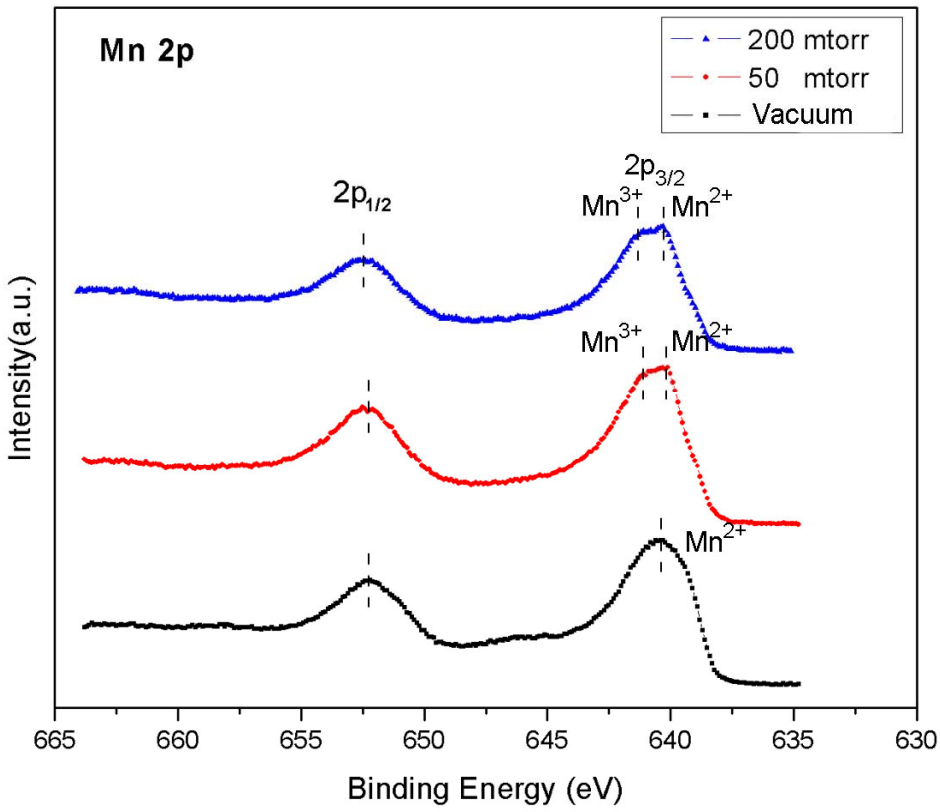

FIG. 5.2. XPS spectra of the Mn 2p regions for Mn_3O_4 thin films deposited under different oxygen pressures (vacuum, 50mtorr and 200mtorr, respectively).

The variations in chemical composition and oxidation state of as-deposited thin films were further examined by XPS with a detailed analysis on binding energy peak positions and shapes. Figure 5.2 shows the XPS spectra of the Mn 2p regions for the samples deposited under different oxygen pressures. The binding energy curve of Mn $2p_{3/2}$ spectra split into two peaks (Mn^{3+} and Mn^{2+}) for the sample deposited under 50

mtorr (in red) and 200 mtorr (in blue) oxygen pressure, and the one deposited in vacuum (in black) only shows single distinct peak. The typical binding energy of Mn ions in Mn_3O_4 and Mn_2O_3 at the Mn($2p_{3/2}$) region have a 1.0eV marginal window within 640.7-641.7eV according to literature report.[200] Obvious splitting of Mn($2p_{3/2}$) spectra for sample deposited with 50 mtorr and 200 mtorr oxygen pressure corresponds to different Mn ionic states in Mn_3O_4 and Mn_2O_3, which does not show in the spectra of sample deposited in vacuum. The extra phases shown in XPS spectra of Mn_3O_4 thin films as increasing oxygen pressure during deposition reveal that oxygen atmosphere could also affect the deposited film stoichiometries even though it helps decreasing the oxygen vacancies and improving the film quality, which is consistent with earlier XRD discussions.

The variation of Mn_3O_4 thin film microstructure and crystallinity as a function of oxygen pressure was studied by cross-section TEM as shown in Figure 5.3 a-f. Mn_3O_4 thin film deposited in vacuum contains obvious grain boundaries (GB) with the average grain size around 50 nm as shown in Figure 5.3a. The 45º in-plane rotated epitaxial growth orientations are determined to be Mn_3O_4(004)//STO(002) and Mn_3O_4(220)//STO(200) from the corresponding selected area diffraction (SAD) pattern as the inset in Figure 5.3a. High resolution TEM image in Figure 5.3b shows vertical grain boundaries within the epitaxial film. Instead of the large amount of vertical grain boundaries, continuous films were formed for the film deposited under 50 mtorr oxygen as shown in Figure 5.3c. Few surface clusters were observed with an average spacing of 80 nm. It is noted that strain contour can be found right underneath the

surface clusters. High quality epitaxial growth is demonstrated from the high resolution image in Figure 5.3d and the corresponding SAD pattern in Figure 5.3c. With increasing oxygen pressure up to 200mtorr, the sample shows improved film crystallinity however the dominated phase is now Mn_2O_3 as evidenced from the high resolution TEM image in Figure 5.3f and the SAD pattern inserted in Figure 5.3e. The film/substrate orientation relations are determined to be $Mn_3O_4(004)//Mn_2O_3(004)//STO(002)$ and $Mn_3O_4(220)//Mn_2O_3(220)//STO(200)$. The distinguished diffraction dots from manganese oxide film demonstrate the epitaxial growth of the film on STO substrate in-plane and out-of-plane. Above TEM study suggests that higher oxygen pressure improves the epitaxial quality of the manganese oxide films. However, proper oxygen pressure is needed for achieving the desired composition and Mn ionic state.

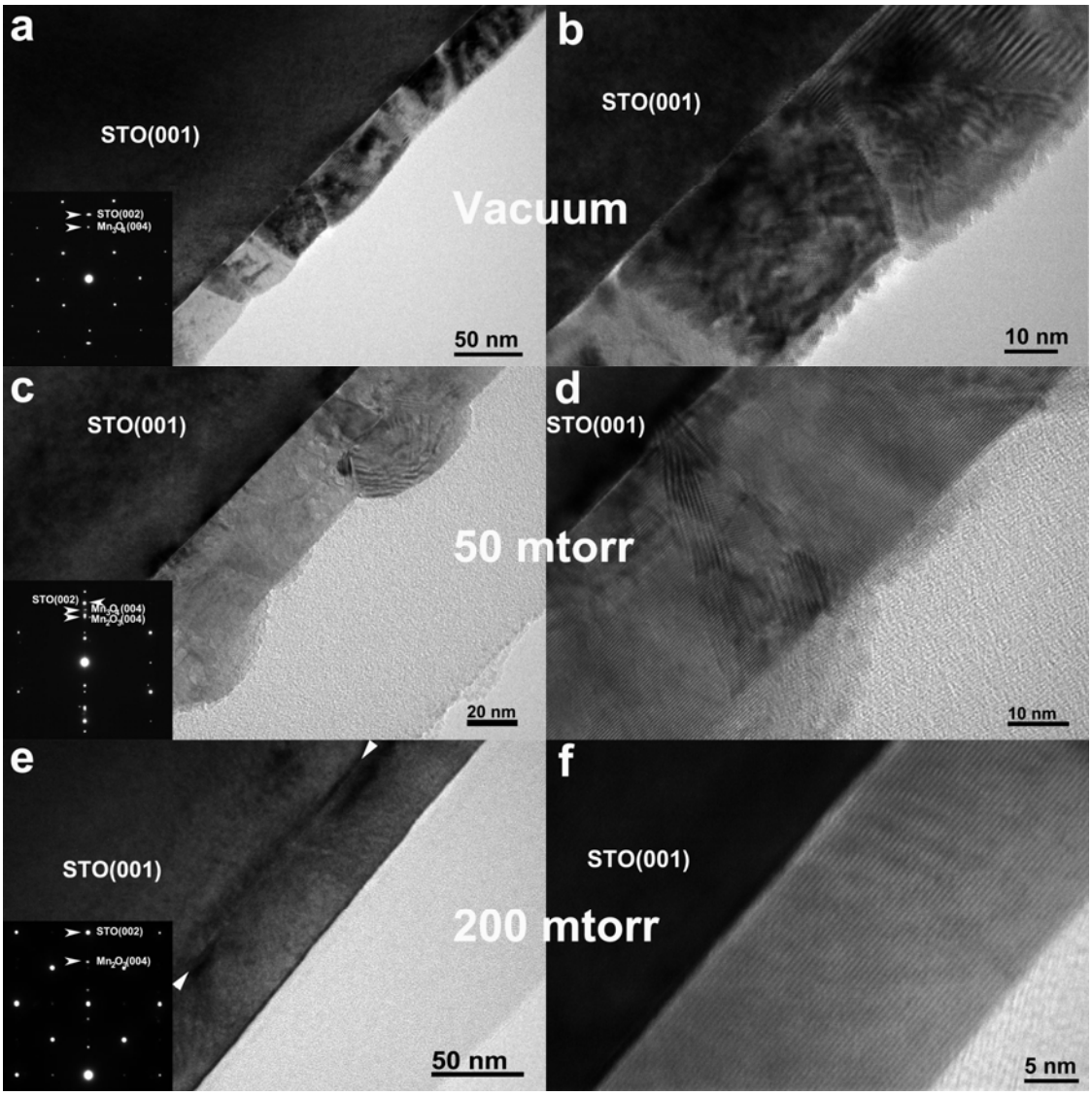

FIG. 5.3. TEM micrographs of Mn_3O_4 films deposited under different oxygen pressures. a) and b) in vacuum; c) and d) with 50mtorr O_2; e) and f) with 200mtorr O_2. Selected area diffraction patterns from all the film and substrate are shown as inset in a, c and e.

High vacuum and proper deposition conditions are critical for achieving high quality thin films by PLD. For example, high deposition pressure will decrease the plume size as well as the mean free path of deposited adatoms.[114,201] In this work, Mn_3O_4 thin films deposited in vacuum have a continuous layer with very smooth surface from SEM study as shown in Figure 5.4a. As the oxygen pressure increased to 50 mtorr and 200 mtorr, rectangular clusters formed on the surface of the continuous films and its density increased as the oxygen pressure increases (Figure 5.4b and c). The cluster formation may be caused by the reduction of the adatoms mean free path / surface diffusion rate as the oxygen pressure increases from vacuum to higher values. And this may also reveals a transition of the Mn_3O_4 thin film growth from Frank-vander Merve (2D, layer by layer) mode to Volmer-Weber (3D, cluster) mode.[202] Proper control in kinetics will help improve film morphologies (e.g., preventing clustering) and achieve stable chemical states.

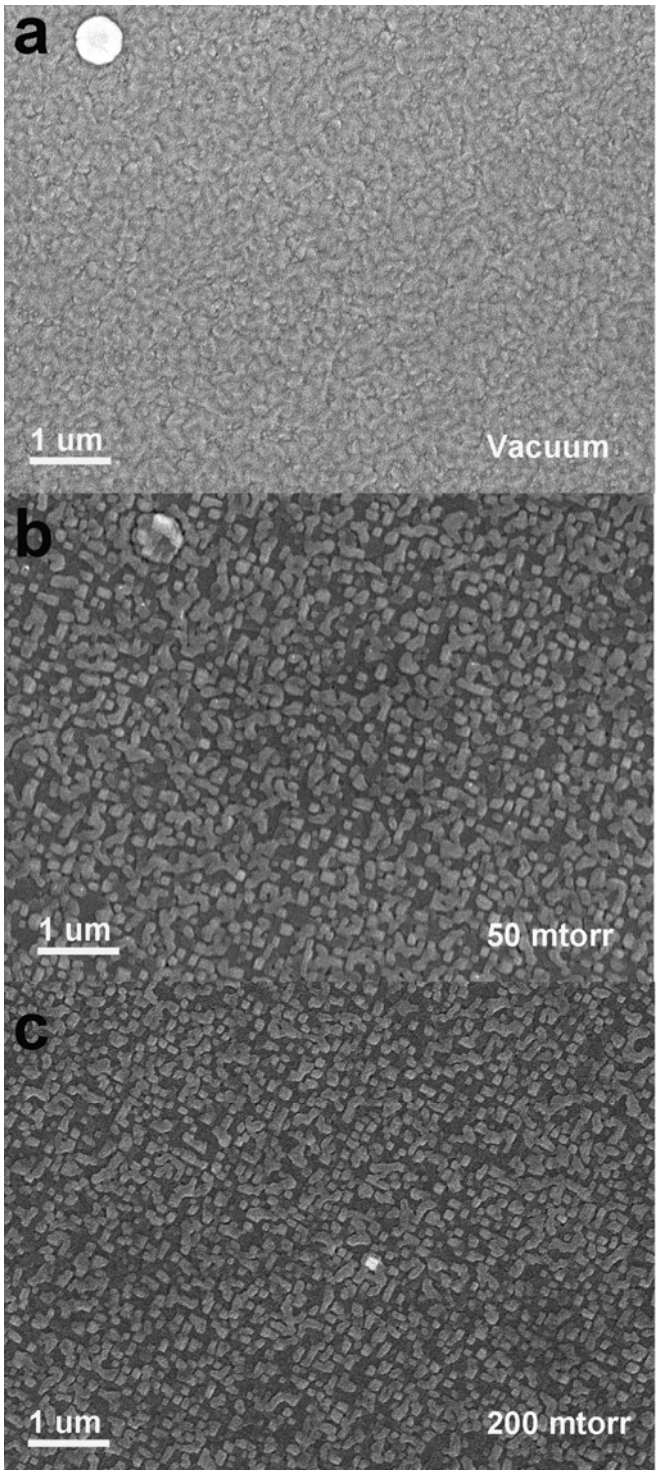

FIG. 5.4. SEM images of Mn_3O_4 thin films deposited under different oxygen pressures (a) in vacuum, b) 50mtorr O_2 and c) 200mtorr O_2 pressure, respectively).

The exchange interaction of Mn^{3+} ions within manganese-oxygen octahedra occurs at lower temperatures, and Mn_3O_4 thin films show ferrimagnetic long-range order below the Curie temperature T_c. Figure 5.5a shows the temperature dependence of magnetization for Mn_3O_4 thin films deposited under different oxygen pressures. The measurements were taken through zero field cooling (ZFC) process. Samples were cooled down from 300K to 5K without external magnetic field, and then the magnetization was measured as a function of temperature under an applied magnetic field of 10000Oe along [100] axis during the warming-up process. T_c is identified using the derivative $|d(M_T)/dT|$ at maximum. Below T_c, the thermal agitation as well as spiral spin caused canted spin array suppresses the demagnetizing field which leads to an increase in magnetization at lower temperatures. Above T_c, the ferrimagnetic long-range ordering disappears and the magnetization drops sharply.[203] ZFC curves in Figure 5.5a show that the curie temperatures for samples deposited under 50 mtorr and 200 mtorr oxygen pressure are 50K and 48K, respectively. The vacuum deposited sample shows weak magnetic performance which may be correlated to its high density grain boundaries and relatively poor crystallinity. The sample deposited under 50 mtorr which has Mn_3O_4 as the dominant phase and best crystallinity, shows higher T_c and magnetization values compared with that of sample deposited under 200 mtorr. The higher T_c may be attributed to the improved film crystallinity by the precise control of the oxygen pressure and film stoichiometry during PLD. In addition, STO(001) substrate used in this study could provide a large film-substrate mismatch (i.e., compression in-plane and tension out-of-plane) compared with other cases, such as

Mn_3O_4 grown on MgO(001) with tension in-plane and compression out-of-plane. Stronger exchange interactions between Mn^{3+} ions with larger c-axis crystal lattice distortion in the manganese-oxygen octahedral could lead to higher T_c value.

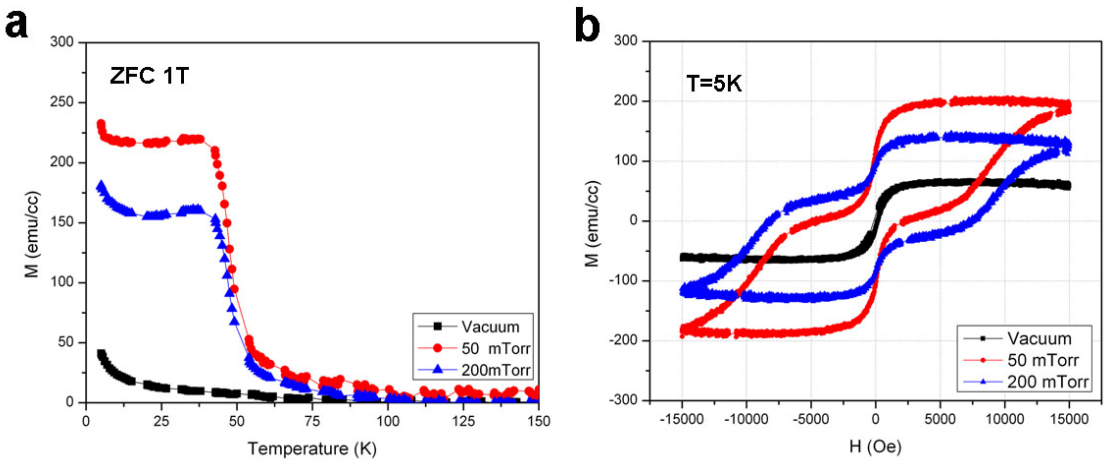

FIG. 5.5. Magnetization measurements of Mn_3O_4 thin film samples. a) Dependence of the magnetization as a function of temperature for Mn_3O_4 thin films deposited under different oxygen pressures. Samples were cooled from 300K to 5K without applying magnetic fields, then measurement start in a magnetic field of 10000Oe, applied along [100] axis. b) The magnetization hysteresis curves of Mn_3O_4 thin films deposited under different oxygen pressures measured at 5K. The magnetic field is applied along the [100] axis.

The magnetization hysteresis loops in Figure 5.5b were measured at 5K along the [100] direction for Mn_3O_4 thin films deposited under different oxygen pressures. It is obvious that the hysteresis loops compose the contributions from both Mn_3O_4 and Mn_2O_3 phases for both 50 mtorr oxygen and 200 mtorr samples. The one deposited under 50 mtorr oxygen pressure shows the highest magnetic saturation at 200emu/cc which is attributed to its dominant Mn_3O_4 phase. This saturation magnetization here is similar to other Mn_3O_4 single crystal and polycrystalline samples as reported.[203,204] The one deposited under 200 mtorr oxygen pressure has lower magnetic saturation at 145emu/cc but a larger coercivity (4000Oe) as compare with that of the sample deposited under 50 mtorr oxygen pressure (7000Oe), which is mainly due to the major Mn_2O_3 phase in the film. Meanwhile, the smaller coercivity might be also resulted from the anisotropy effect due to the disorder based on different crystal orientations and can be improved in single-crystal sample by applying the external magnetic field along an easy magnetization axis. The distortion of hysteresis loops for the 50mtorr and 200mtorr samples indicates the former one has a major Mn_3O_4 phase and Mn_2O_3 phase will become dominant as oxygen pressure increases to 200mtorr. The sample deposited under vacuum does not show obvious ferrimagnetic properties, which is largely attributed to its high density grain boundaries and its relatively poor crystallinity. Its narrow hysteresis loop implies a small amount of dissipated energy in repeatedly reversing the magnetization. Above observations coincide with earlier discussions, i.e., proper oxygen pressure improves the film crystallinity and lead to stronger magnetic responses. On the other hand, extra oxygen could involve the

formation of secondary phases such as Mn_2O_3 and MnO, which might cause opposite moments/ionic states within the sublattices and thus lead to deterioration of magnetic performance.

5.5 Conclusions

We have investigated epitaxial and highly textured Mn_3O_4 thin films grown on single crystal STO (001) substrates under different oxygen pressures. XRD analysis reveals that 50mtorr oxygen pressure results in Mn_3O_4 as the dominant phase with better crystallinity. However, higher oxygen pressure such as 200 mtorr results in the formation of secondary phases such as MnO and Mn_2O_3. TEM study also suggests that proper oxygen pressure helps improving the film quality and decreasing the amount of grain boundaries. The epitaxial Mn_3O_4 thin films with 50mtorr pressure shows an improved T_c of 50K and a saturation magnetization of 200emu/cc which are higher than other literature reports on epitaxial Mn_3O_4 thin films. This work demonstrates that proper oxygen pressure is one of the key factors in achieving better thin film crystallinity/microstructure as well as enhanced ferrimagnetic properties for Mn_3O_4 thin films.

CHAPTER VI

GROWTH MECHANISM STUDY ON $(SrTiO_3)_{0.5}$:$(MgO)_{0.5}$ VERTICALLY ALIGNED NANOCOMPOSITE THIN FILMS

6.1 Overview

Epitaxial two-phase vertically aligned nanocomposite (VAN) $(SiTiO_3)_{0.5}$:$(MgO)_{0.5}$ thin films were deposited by pulsed laser deposition on both $SrTiO_3$ and MgO substrates. The nanocomposite thin films exhibit a highly ordered vertical columnar structure with high epitaxial quality. The growth rate of the nanocomposite thin films can be adjusted by laser energy densities and laser repetition rate. We demonstrate that the strains of the two phases are relaxed as increasing the laser repetitions. The column width is 3nm for MgO columns and 20nm for STO columns in nanocompoiste films deposited on STO and MgO substrates, respectively. It is possible that the in-plane tension induced by MgO substrate causes a faster diffusion rate of STO phase and therefore a relatively larger column dimension was achieved in the nanocomposite thin films. In addition to deposition parameter variation, this study suggests another promising avenue in achieving microstructure control such as the column width in VAN thin films by substrate induced strain engineering.

6.2 Introduction

Over the past several years, vertically aligned nanocomposite (VAN) thin films have received more and more research interest due to its potential in achieving multifunctionality, enhanced single functionality and novel nanostructures.[36,68,100,102] In VAN thin films, two phases are self-assembled heteroepitaxially grown on given substrates and form a unique nano-checkerboard structure in-plane. The VAN architecture (shown in Figure 6.1a) promises a novel way of achieving tunable strains which is very different to the situation on normal composite films. The strains in VAN thin film exist not only on the film-substrate interface due to epitaxial film growth, but also on the vertical interfacial phase boundaries with lattice matching in between. In VAN thin films, the vertical column width are relative small around 20nm that the substrate induced strain can not fully relax. The strain in the lower modulus phase is mainly controlled by that in the higher modulus phase and can be maintained throughout much thicker film thickness (>500nm). The area density of vertical column phase boundary is a main factor that affects the competition between vertical and horizontal strains which can be adjusted by the deposition frequency and composite ratio.[38,114] On the other hand, different substrate induced strain can also play another role in affecting the column width, further more tuning vertical boundary area density as well as the vertical strain.

In this work, we developed VAN $(SrTiO_3)_{0.5}$:$(MgO)_{0.5}$ nanocomposite thin films as model and investigate the substrate strains effect on composite film microstructure

and strains. As shown in Figure 6.1b and c, the composite thin films have been deposited on $SrTiO_3$ (STO) and MgO substrates, respectively. Both phase are in cubic but with different lattice parameters as for STO (a=3.905Å) and MgO (a=4.2 Å). The strains of nanocomposite thin films grown on different substrates are in opposite status. Other factors such as the laser energy density and laser repetition rate during the deposition have also been systematically adjusted to investigate their effect to the growth morphology of the nanocomposite thin films.

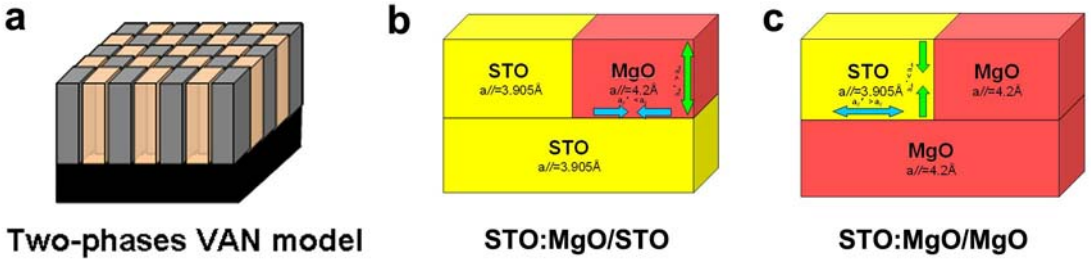

FIG 6.1. Schematics of VAN thin films. (a) Two phases VAN thin film model; (b) STO:MgO VAN thin film grown on STO substrate; (c) STO:MgO VAN thin film grown on MgO substrate.

6.3 Experimental

$(STO)_{0.5}$:$(MgO)_{0.5}$ thin films were deposited on single crystal STO(001) and MgO(001) substrates in a PLD system with a KrF excimer laser (Lambda Physik Compex Pro 205, λ= 248 nm), respectively. The laser beam was focused to obtain an energy density (~ 4 Jcm^{-2}) at an incidence angle of 45°. The $(STO)_{0.5}$:$(MgO)_{0.5}$ target were prepared by a conventional powder mixing method. An optimized substrate temperature (700 ± 5°C) and an oxygen pressure of 0.2 torr were maintained during deposition.

In this work, we processed $(STO)_{0.5}$:$(MgO)_{0.5}$ two-phase VAN thin films grown on STO(001) substrates with different laser energy densities (3.4; 4.3; 5.2 and 6 Jcm^{-2}) and deposition frequencies (Sample Set 1 at 2Hz; Set 2 at 5 Hz; and Set 3 at 10Hz), one of the most important deposition parameters during PLD growth. We conducted a detailed strain analysis in these VAN nanocomposite films as functions of deposition frequency, based on the d-spacing measured from selected diffraction patterns.

The strain and microstructure of the as-deposited films were characterized by X-ray diffraction (XRD) (BRUKER D8 powder X-ray diffractometer), transmission electron microscopy (TEM) (JEOL 2010 analytical microscope with a point-to-point resolution of 0.23 nm) and scanning transmission electron microscopy (STEM) (FEI Tecnai G2 F20). A standard cross-section TEM sample preparation including manual grinding and thinning of sample with a final ion milling step (PIPS 691 precision ion polishing system, 3.7 KeV), was used.

6.4 Results and discussion

$(STO)_{0.5}$:$(MgO)_{0.5}$ thin films grown on STO(001) substrate show vertically aligned columnar structure with good epitaxial quality. The lattice parameters of STO and MgO are 3.905Å and 4.20Å, respectively. The lattice mismatch between MgO phase and STO substrate is around 7% which will lead to a domain matching and epitaxial growth of MgO phase. Since STO phase in the composite thin film have the same material crystal structure to the substrate, it will diffuse much faster as compared to the MgO phase. Figure 6.2a gives the θ-2θ XRD pattern of deposited $(STO)_{0.5}$:$(MgO)_{0.5}$ thin films on STO(001) substrate. It shows an obvious cube-on-cube growth of both phases with the crystal orientation in a relationship of MgO_{film} (002)//STO_{film}(002)//STO_{sub}(002). Cross-section TEM image in Figure 6.2b reveals the film thickness is around 60nm and with smooth film surface for the film deposited at 2Hz. Both STO and MgO phases all aligned alternatively next to each other and the columnar structure go through the whole film thickness. Both phases have grown epitaxially on STO substrate, evidenced by the distinguished diffraction dots from STO and MgO phases in the corresponding selected area diffraction (SAD) patterns in Figure 6.2c. The orientation relationships are determined to be MgO_{film} (002)//STO_{film}(002) and MgO_{film} (020)//STO_{film}(020). Plan-view TEM image in Figure 6.2d confirmed the morphology of two phases in the composite film. Due to their different surface free energy to the substrate and diffusion rate, the $(STO)_{0.5}$:$(MgO)_{0.5}$ thin films grown on STO substrate have MgO columns grown in the STO continued

thin film matrix. One of the most distinguished findings is that this system shows ultra thin column dimension (around 3nm). This may caused by the largely thermal dynamics status of two phases to the substrate. To systematically study the column/domain size variation over a large area, we conducted a detailed scanning transmission electron microscopy (STEM) study on all the samples. STEM under the high angle annular dark field (HAADF) condition, is also called Z-contrast imaging, where the contrast is approximately proportional to the square of the atomic number ($Z^{1.7}$). Figures 6.2e shows the Z-contrast images of $(STO)_{0.5}$:$(MgO)_{0.5}$ VAN thin films grown on STO(002) substrate. The most striking feature is the bright/dark columns that align alternatively in the lateral direction, indicating the presence of vertically aligned STO and MgO columns. The STO film matrix are much brighter than the MgO columns as the Z number of Sr (Z=38) is higher than that of Mg (Z=12). All the nanocolumns are grown vertically through the film thickness without obvious column tilting. No obvious interface mixing was observed in the view areas.

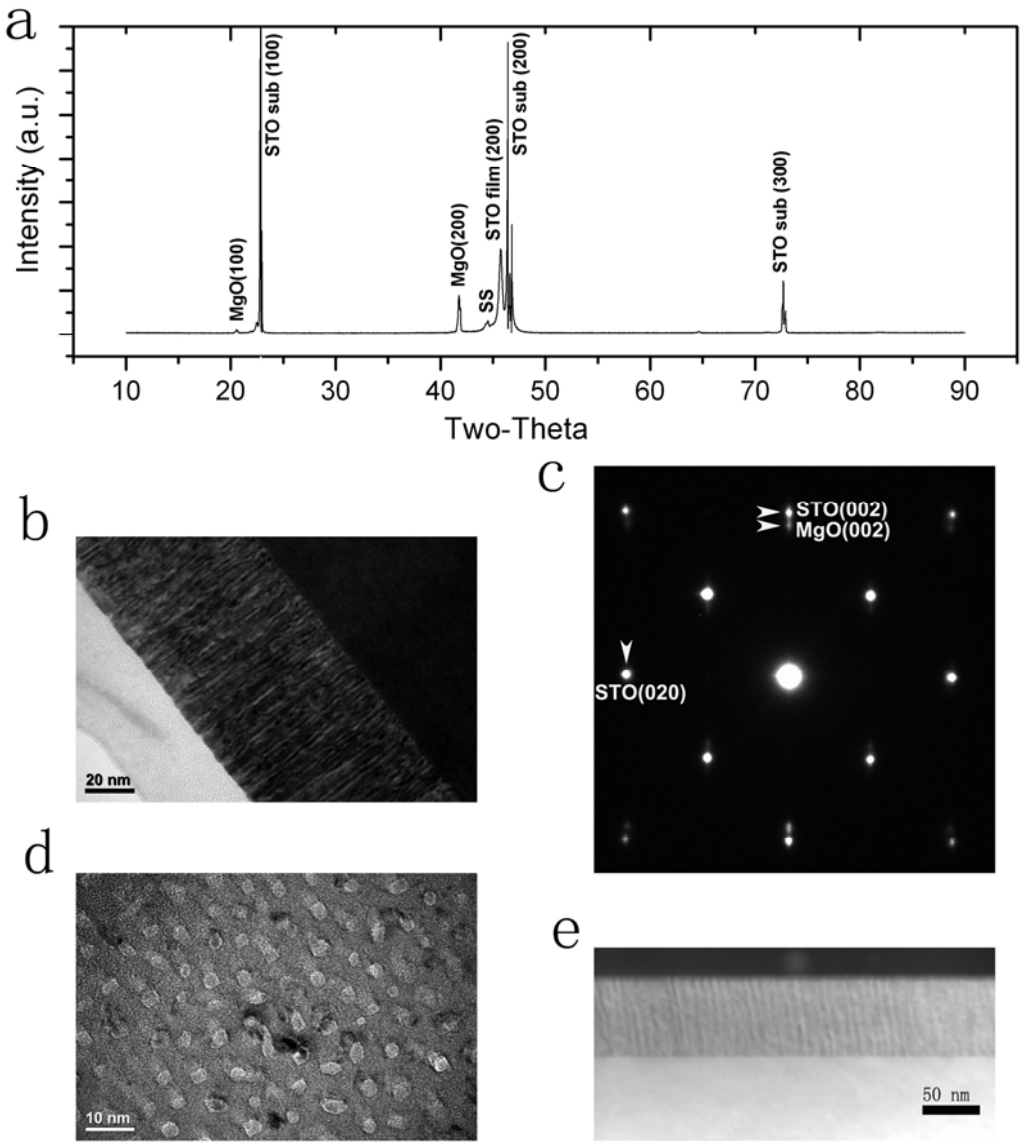

FIG 6.2. Microstructure and crystallinity of $(SrTiO_3)_{0.5}$:$(MgO)_{0.5}$ thin films grown on SrTiO3(001) substrate. (a) XRD θ~2θ scans of STO:MgO films deposited at 2Hz; (b) cross-section TEM image shows vertically columnar growth of both phases; (c) selected area diffraction pattern from the film region; (d) plan-view TEM image of STO:MgO thin film deposited at 2Hz; (e) scanning TEM image shows phases separation and columnar VAN structure.

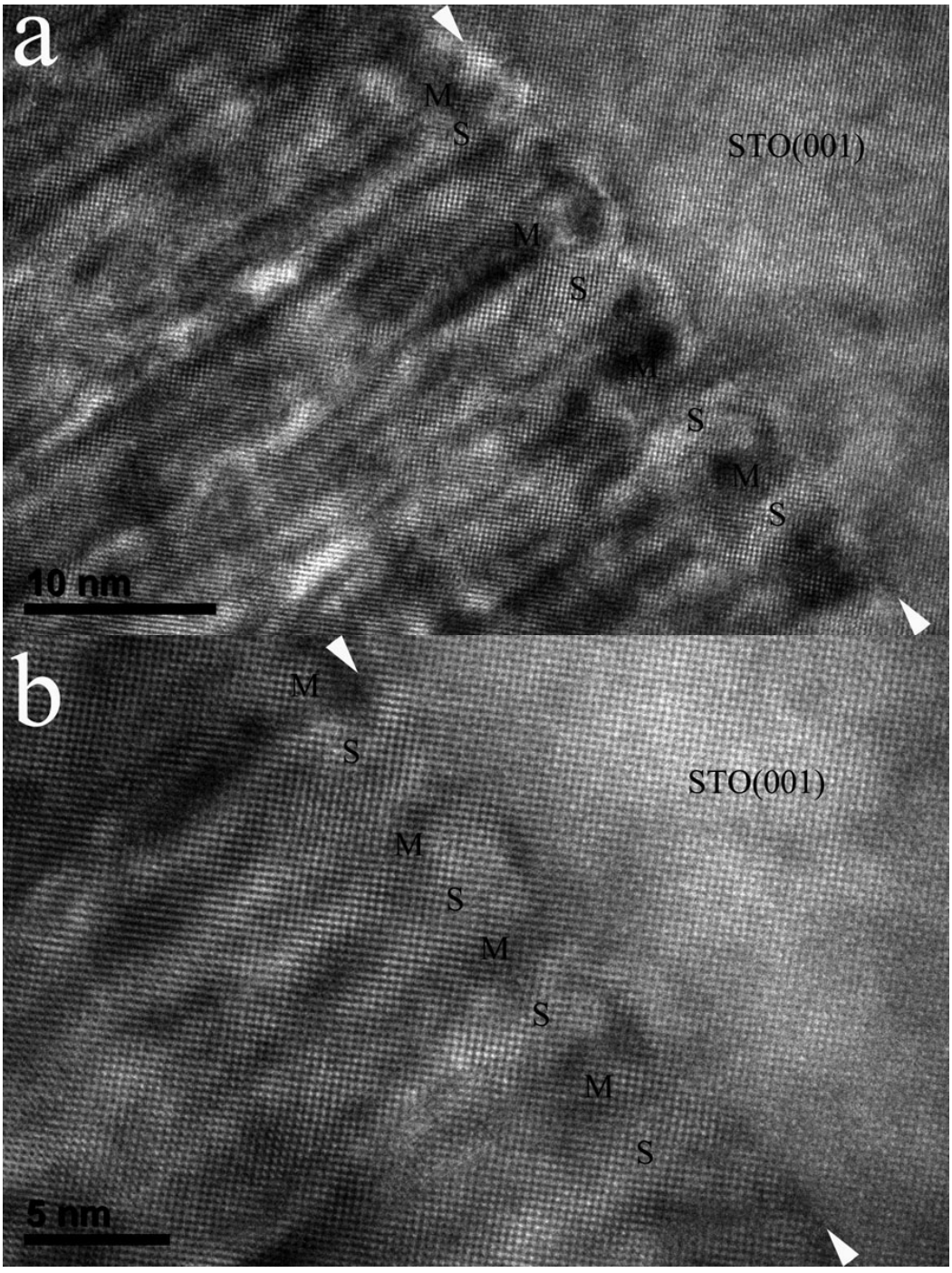

FIG 6.3. High resolution cross-section TEM images of $(SrTiO_3)_{0.5}$:$(MgO)_{0.5}$ thin films grown on $SrTiO_3$(001) substrate deposited at 2Hz. (a) 500K HRTEM image and (b) 800K HRTEM image.

High resolutions cross-section TEM images in Figure 6.3 were taken at 500K magnification and 800K magnification, respectively. It is clearly to see a smooth transition of STO phase from the substrate to film. The MgO phase in the film shows a darker contrast which corresponding to its atomic weight. The MgO columns are extremely narrow as around 3nm in the $(SrTiO_3)_{0.5}$:$(MgO)_{0.5}$ thin films grown on STO substrate.

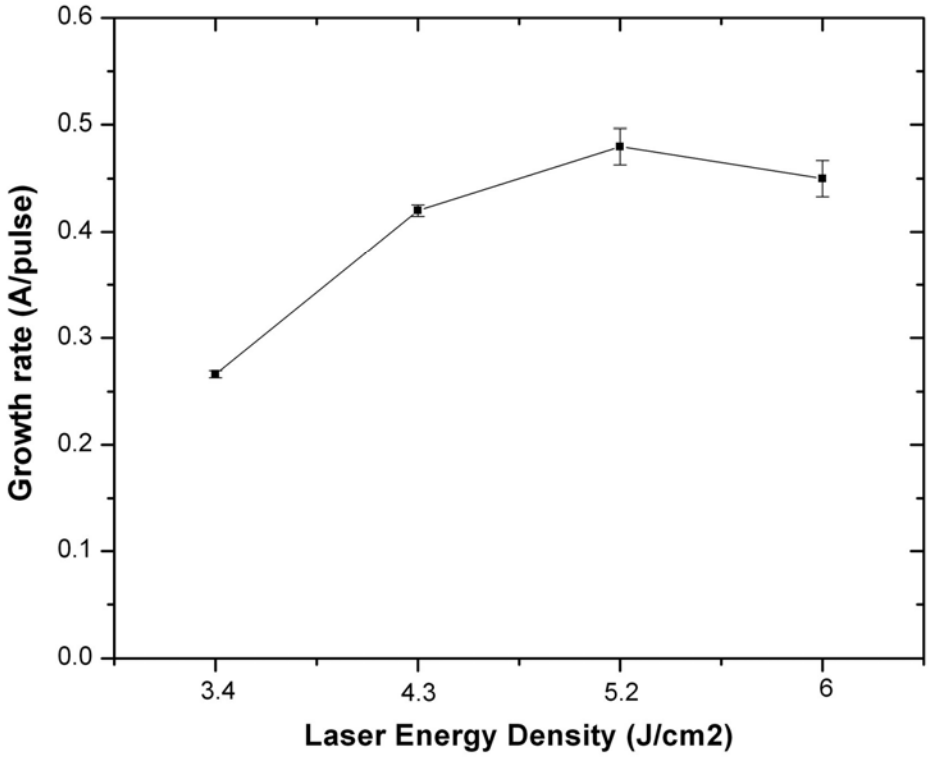

FIG 6.4. The growth rate of $(SrTiO_3)_{0.5}$:$(MgO)_{0.5}$ thin films grown on $SrTiO_3$(001) substrate as a function of laser energy densities.

The growth mechanism of $(SrTiO_3)_{0.5}$:$(MgO)_{0.5}$ nanocomposite thin films is strongly dependent on the growth rate of the film. In this work, the growth rate of deposited thin films has been tuned by adjusting the laser energy densities and pulse repetition rate. Figure 6.4 shows the growth rate of composite thin films deposited with laser energy densities of 3.4 J/cm^2, 4.3 J/cm^2, 5.2 J/cm^2 and 6 J/cm^2, respectively. For all the samples, cross-section TEM images show well aligned VAN architecture and there are no obvious column width changes. The sample deposited with 5.2 J/cm^2 laser energy density shows the highest grow rate. The particles in the laser plasma plume obtain higher kinetic energy when the laser energy density increases.[205] Thus, the diffused length of both $SrTiO_3$ and MgO phases increase which can improve the phase crystallites. However, at the same time, higher laser energy density also produces larger grain size in the films, which degrades the smoothness of the surface.

Laser repetition rate is another important factor that will affect the film microstructures. Figure 6.5 gives the selected area (SAD) diffraction patterns from different sample regions as labeled, respectively. As the laser repetition rate increases from 2Hz to 5Hz and 10Hz, as shown in Figure 6.5 b to d, the in-plane diffraction dots of MgO phase show up instead of overlapping with that of the $SrTiO_3$ phase. The lattice parameter of $SrTiO_3$ phase in the nanocomposite films is similar to that of the substrate due to the surface energy deficiency. SAD patterns reveal that higher laser repetition rate at 5Hz and 10Hz will form the MgO phase with larger in-plane lattice parameters.

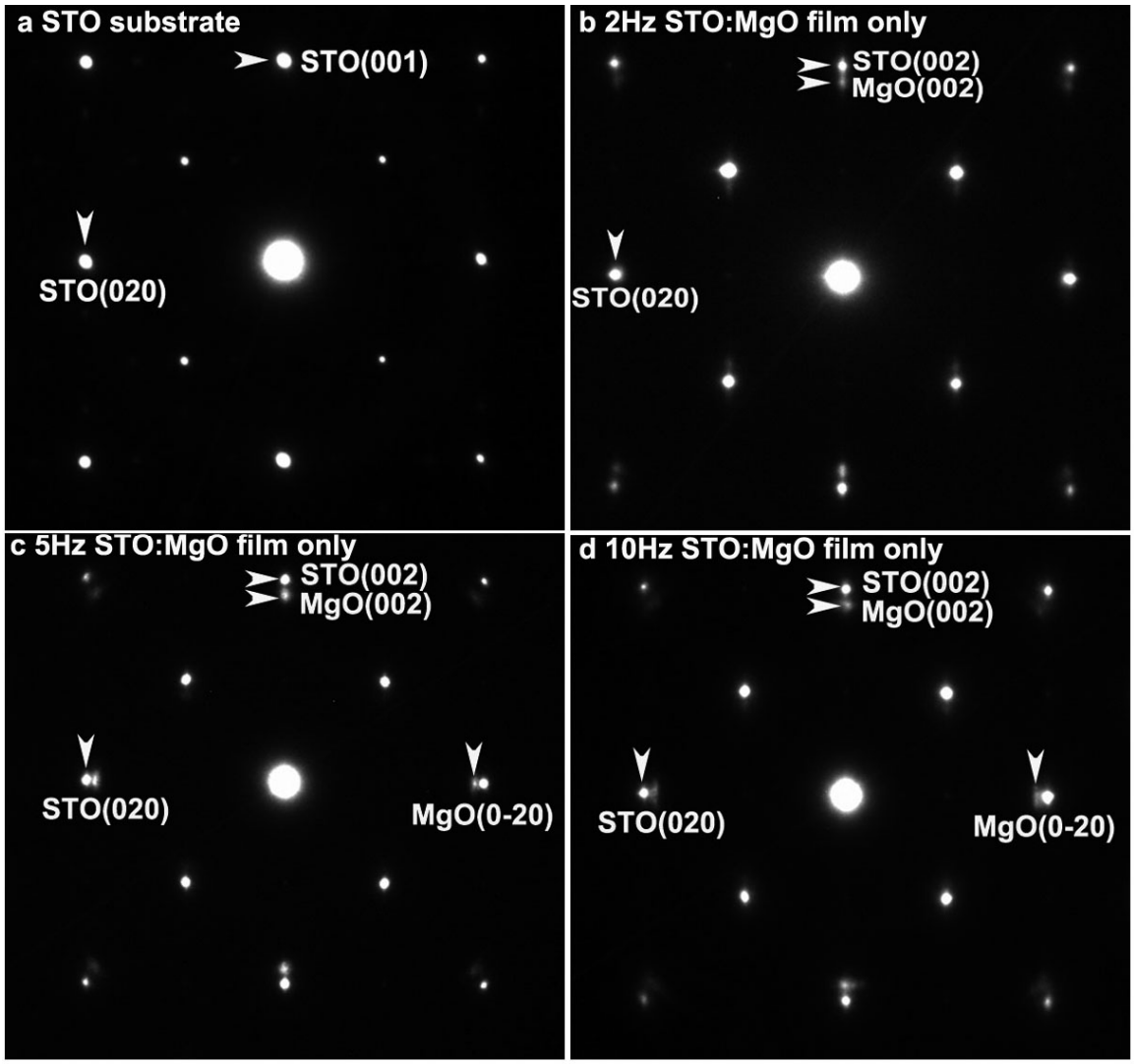

FIG 6.5 Selected area diffraction patterns of $(SrTiO_3)_{0.5}$:$(MgO)_{0.5}$ thin films grown on $SrTiO_3$(001) substrate. (a) SAD pattern from pure STO(001) substrate, (b) SAD of film only region on 2Hz deposited $(SrTiO_3)_{0.5}$:$(MgO)_{0.5}$ thin film; (c) SAD of film only region on 5Hz deposited $(SrTiO_3)_{0.5}$:$(MgO)_{0.5}$ thin film and (d) SAD of film only region on 10Hz deposited $(SrTiO_3)_{0.5}$:$(MgO)_{0.5}$ thin film.

Figure 6.6 reveals the lattice parameters of both STO and MgO phases as a function of laser repetition rate. It is obviously to see that the strain in MgO phase has been largely adjusted as increasing the deposition frequency from 2Hz to 5Hz and 10Hz as compared that of the STO phase. Comparing the lattice paramters of $SrTiO_3$ (a=3.905Å) and MgO(4.2Å), the in-plane compression of MgO phase decreases as increase the laser repetition as shown in Figure 6.6b. Adjusting the laser repetition during deposition will effect the competition between kinetics and thermodynamics at the early stage of nanocomposite thin films growth.

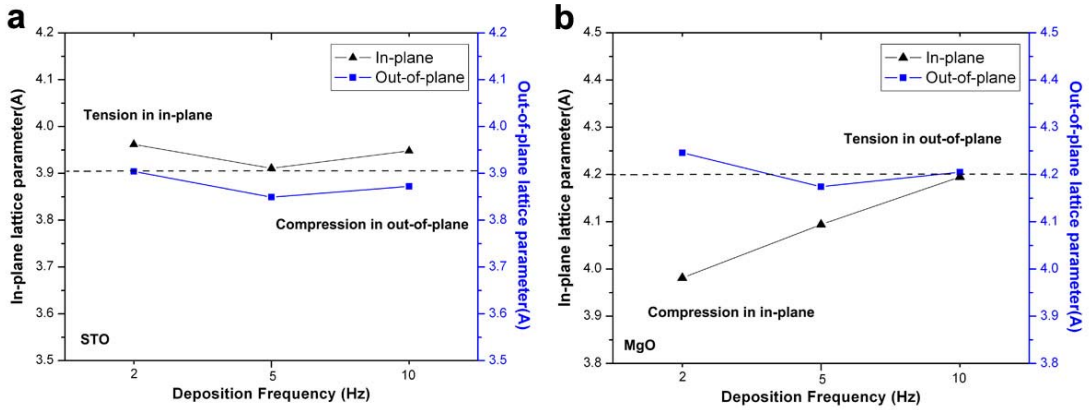

FIG 6.6. Lattice parameters of (a) $SrTiO_3$ and (b) MgO phases in the $(SrTiO_3)_{0.5}$:$(MgO)_{0.5}$ thin films grown on $SrTiO_3$(001) substrate with different deposition frequencies.

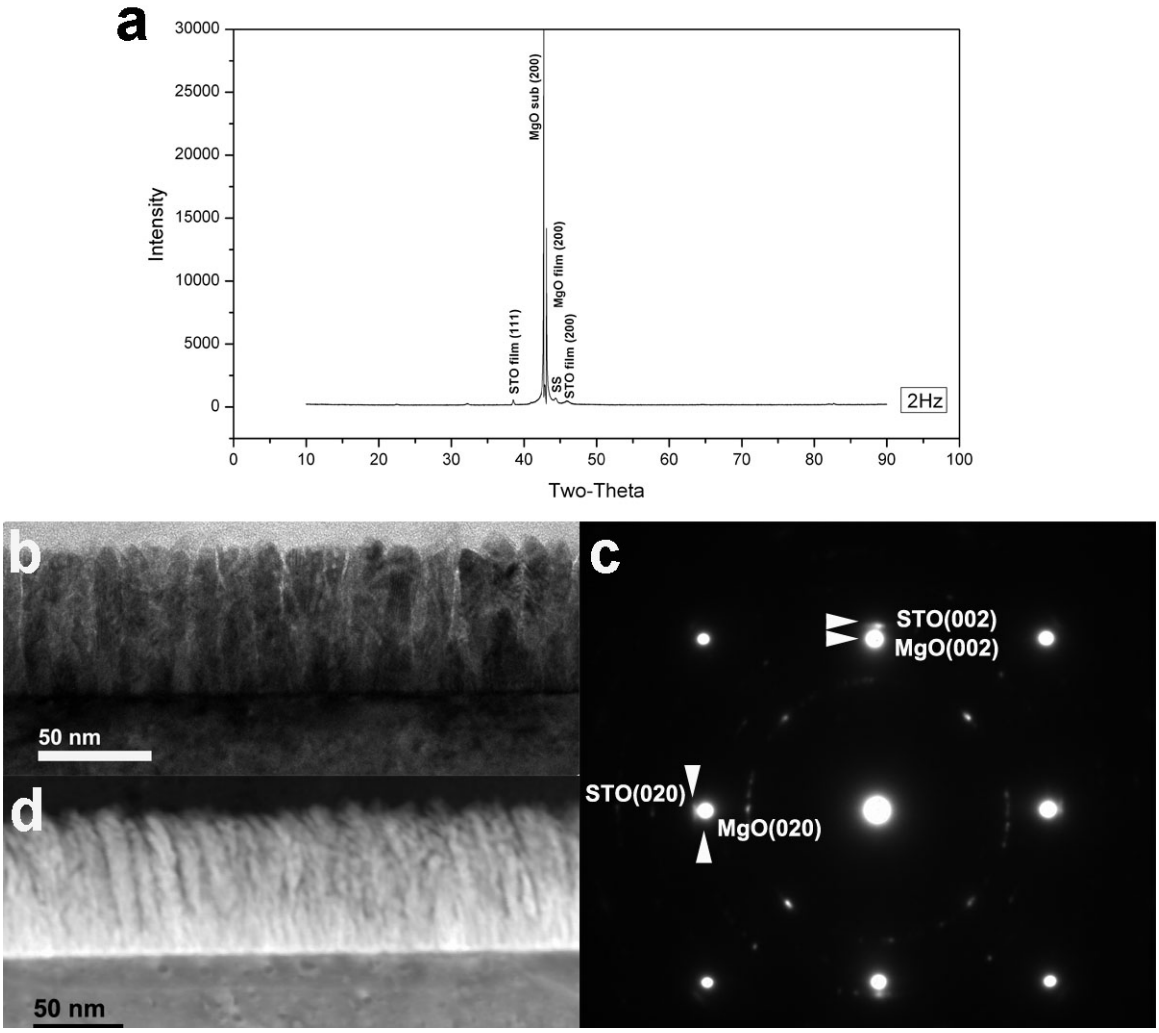

FIG 6.7. Microstructure and crystallinity of $(SrTiO_3)_{0.5}$:$(MgO)_{0.5}$ thin films grown on MgO(001) substrate. (a) XRD θ~2θ scans of STO:MgO films deposited at 2Hz; (b) cross-section TEM image shows vertically columnar growth of both phases; (c) selected area diffraction pattern from the both the film and substrate region; (d) scanning TEM image shows phases separation and columnar VAN structure.

$(STO)_{0.5}$:$(MgO)_{0.5}$ thin films grown on MgO(001) substrate also show vertically aligned columnar structure and epitaxial growth. Similar lattice matching relationships between the growth phases and the MgO substrate, however there is tension in-plane in the STO film phases. Figure 6.7a gives the θ-2θ XRD pattern of deposited $(STO)_{0.5}$:$(MgO)_{0.5}$ thin films on MgO(001) substrate. It shows an cube-on-cube growth of both phases with the crystal orientation in a relationship of MgO_{film} (002)//STO_{film}(002)//STO_{sub}(002). Another STO(111) peak indicate the polycrystal portion in the STO columns. Cross-section TEM image in Figure 6.7b reveals the film thickness is around 60nm but with much larger column width around 20nm as compared to the $(STO)_{0.5}$:$(MgO)_{0.5}$ thin films grown on STO(001) substrate. Both STO and MgO phases all aligned alternatively next to each other and the columnar structure go through the whole film thickness. Both phases have epitaxially growth on STO substrate, evidenced by the distinguished diffraction dots from STO and MgO phases in the corresponding selected area diffraction (SAD) patterns in Figure 6.7c. The orientation relationships are determined to be MgO_{film} (002)//STO_{film}(002) and MgO_{film} (020)//STO_{film}(020). Figures 6.7d shows the Z-contrast images of $(STO)_{0.5}$:$(MgO)_{0.5}$ VAN thin films grown on MgO(001) substrate. The most striking feature is the bright/dark columns that align alternatively in the lateral direction, indicating the presence of vertically aligned STO and MgO columns. All the nanocolumns are grown vertically through the film thickness without obvious column tilting. No obvious interfacial mixing was observed in the view areas.

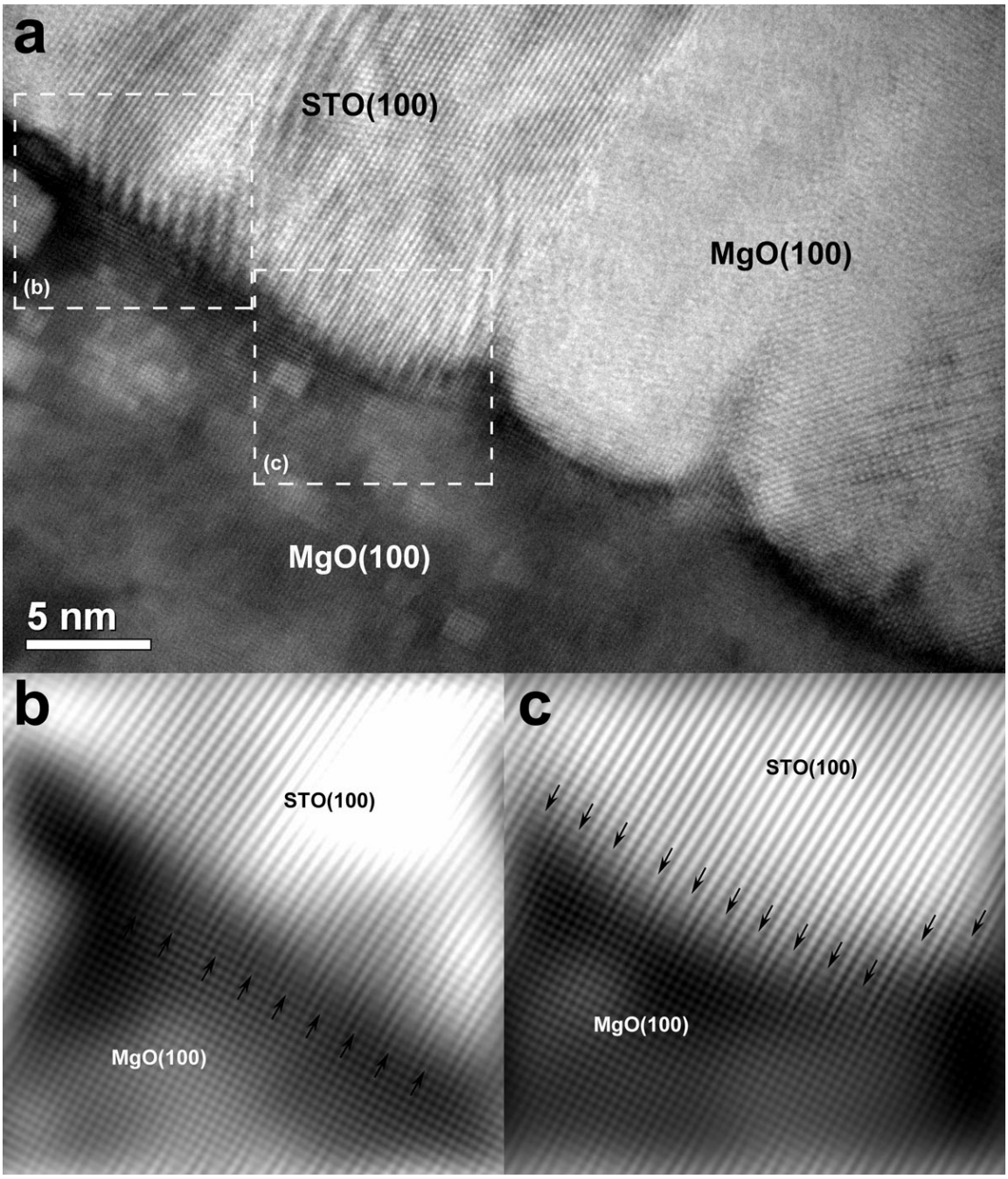

FIG 6.8. (a) High resolution cross-section TEM image of $(SrTiO_3)_{0.5}$:$(MgO)_{0.5}$ thin films grown on MgO(001) substrate. (b) and (c) Fourier transferred TEM images on selected regions.

Figure 6.8 shows high resolution cross-section TEM image of $(STO)_{0.5}$:$(MgO)_{0.5}$ thin films grown on MgO(001) substrate at 2Hz. As mentioned earlier, for an epitaxial growth of MgO with in-plane lattice 4.2Å and STO with in-plane lattice 3.905Å on MgO substrate, there is a 7% lattice mismatching. TEM image shows clear lattice matching with ration around STO:MgO = 4:6. Fourier filtered TEM images on area b and c also demonstrates the lattice matching relations. It should be noticed that the film-substrate interface is not flat from the HRTEM image and also the MgO substrate could be easily contaminated during the deposition. There is a possibility that there may have some extra chemical or physical reactions happened at the beginning of the deposition on MgO substrate.

One of the most obvious points as compare the $(STO)_{0.5}$:$(MgO)_{0.5}$ nanocomposite thin films grown on STO and MgO substrates respectively is that they both have VAN architecture but with different column dimensions. The column width is 3nm for MgO phase and 20nm for STO phase in nanocomposite films grown on STO substrate and MgO substrate, respectively. The big difference of column width of the doped phase in nanocomposite thin films corresponds to the different diffusion rate of phase grown on different substrates. In the initial stage of thin films grown on flat substrates, the diffusion rate determines the average distance an adatom will travel before joining an existing island or create a new island to finally form the columns in VAN thin films. With different in-plane lattice parameters, MgO and STO substrate provide tension and compression to the deposited $(STO)_{0.5}$:$(MgO)_{0.5}$ nanocomposite thin films, respectively. It has been studied that for III-V metal alloys like GeSi growth on substrates with

different strains, the in-plane compression provide faster diffusion rate of the deposited adatoms at the early stage of the film growth.[206] There is diffusion competition between MgO and STO phases in the growth of composite films. The MgO substrate induced tension is believed one of the most important factors that help achieving larger dope column width.

6.5 Conclusions

Epitaxial two-phase vertically aligned nanocomposite $(SiTiO_3)_{0.5}$:$(MgO)_{0.5}$ thin films were deposited by pulsed laser deposition on $SrTiO_3$ and MgO substrates, respectively. The microstructure and crystal orientations of deposited nanocomposite films have been analysis by TEM and XRD. The growth rate including the laser energy densities as well as the laser repetition rate has been adjusted to investigate their influence to the growth morphology of nanocomposite films on different substrates. It is find that higher laser repetition rate can help relax the substrate induced strain in $(SiTiO_3)_{0.5}$:$(MgO)_{0.5}$ thin films grown on STO substrates. With higher depositition frequencies from 2Hz to 5Hz and 10Hz, the in-plane lattice parameters of MgO increases and the compressive strain relaxes. The $(SiTiO_3)_{0.5}$:$(MgO)_{0.5}$ VAN thin films show different column width as grown on STO and MgO substrates, respectively. It is believed that the in-plane tension induced by MgO substrate causes a faster diffusion rate of STO phase and achieves a relatively larger column dimension in the nanocomposite thin films. This work generate the STO:MgO system as a model to

systematically study the growth mechanism of VAN thin films and demonstrate that the microstructure control such as the column width in functional oxide thin films can be achieved by substrate induced strain engineering.

CHAPTER VII

NANOPOROUS THIN FILMS WITH CONTROLLABLE NANOPORES FROM VERTICALLY ALIGNED NANOCOMPOSITES*

7.1 Overview

Porous thin films with ordered nanopores have been processed by thermal treatment on vertically-aligned nanocomposites (VAN), e.g., $(BiFeO_3)_{0.5}$:$(Sm_2O_3)_{0.5}$ VAN thin films. Uniformly distributed nanopores with an average diameter of 60 nm and 150nm were formed at the bottom and the top of the nanoporous films, respectively. Controllable porosity can be achieved by adjusting the microstructure of VAN $(BiFeO_3)$:(Sm_2O_3) thin films and the annealing parameters. In situ heating experiments within a transmission electron microscope (TEM) column at temperatures from 25°C to 850°C, provides significant insights into the phases transformation, evaporation and structure reconstruction during the annealing. The in situ experiments also demonstrate the possibility of processing vertically aligned nanopores (VANP) with one phase stable in columnar structure. These nanoporous thin films with controllable pore size and density could be promising candidates for thin film membranes and catalysis for fuel cell and gas sensor applications.

---

*This chapter is reprinted with permission from "Nanoporous thin films with controllable nanopores processed from vertically aligned nanocomposites" by Z. Bi, O. Anderoglu, X. Zhang, J. L. Driscoll, H. Yang, Q. Jia, and H. Wang, Nanotechnology 21, 285606 (2010). Copyright 2010 by IOP Publishing Ltd.

7.2 Introduction

Nanoporous materials (thin films) is a kind of nanostructured materials with the presence of pores/holes and possess unique surface, structural and bulk properties that lead to important uses in various fields. Nanoporous membranes and thin films have received a wide range of research interests because of their potential applications as porous catalysis membranes in fuel cells,[207,208,209,210,211] gas sensors,[212-214] and porous anodic alumina oxide (AAO) membrane as template for processing nanotubes and nanowires.[215-217] Besides that, nanoporous materials/thin films also hold great promises working in environmental separations, clean energy production and storages.

In nanoporous thin films, the pores are classified into two types: open pores which connect to the surface of the film, and closed pores which are isolated from the outside. The open pores are often used in functional applications such as catalysis, filtration, adsorption and sensing. In contrast, the closed pores are useful in sonic, thermal insulation and lightweight structures. Porous materials could be classified according to their constitients of their properties as shown in Table 7.1. Nanoporous materials/thin films are a set of micropores, mesopores and macropores. Typically it has large porosity (>40%) and with pore diameters between 1-100nm.

Table 7.1 Classification of nanoporous materials.

	Polymeric	Carbon	Glass	Alumino-silicate	Oxides	Metal
Pore size	Meso-macro	Micro-meso	Meso-macro	Micro-meso	Micro-meso	Meso-macro
Porosity	Low >0.6	High 0.3-0.6	Low 0.3-0.6	High 0.3-0.7	Medium 0.3-0.6	Low 0.1-0.7
Permeability	Low-medium	Low-medium	High	Low	Low-medium	High
Strength	Medium	Low	Strong	Weak	weak-medium	Strong
Thermal stab	Low	High	Good	Medium-high	Medium-high	High
Chemical stab	Low-medium	High	High	High	Very high	High
Costs	Low	High	High	Low-medium	Medium	Medium
Life	Short	Long	Long	Medium-long	Long	Long

Processing porous thin films with geometrically controllable nanopores, i.e., controlled pore density and pore size distribution, is important in achieving consistent chemical catalytic properties of thin film membranes for fuel cells and gas sensor applications. Also understanding those parameters are fundamentally important in investigating materials electrical and mechanical properties. It was reported that the same porous material system processed by different techniques results in a large variation in the electrochemical performance of cathode membrane for solid oxide fuel cells (SOFCs).[218-221] Most of the porous structures were either directly deposited by solution-based techniques or other deposition techniques,[222,223] or achieved by post-deposition processes such as chemical etching,[94,224,225] electrochemical process,[226,227] high resolution photolithography patterning,[228] and e-beam etching.[229] Most of these techniques have difficulties in achieving ordered nanoscale porosity with controlled pore density and pore size distribution. Some of the techniques go through multiple steps (e.g., high resolution lithography patterning) and can be very expensive (e.g., e-beam etching).

Our recent work on vertically aligned nanocomposites (VAN) opens a brand new avenue in achieving ordered nanopores structure. Several VAN structures including $BiFeO_3$:Sm_2O_3 (BFO:SmO),[100,114] $La_{0.7}Sr_{0.3}MnO_3$:ZnO (LSMO:ZnO),[37] and few others systems have been demonstrated.[68,230] Both phases in VAN structures have grown epitaxially with each other on substrates and formed a unique nanochecker-board structure in-plane. It shows vertical strain control along the vertical interface which allows highly strained films achieved in thick films. The two phases in VAN structure

are selected based on their similar growth kinetics, thermodynamic stability and epitaxial growth on given substrates.[100,109] Using this two-phase VAN ordered structures as a template, it is highly possible to process ordered nanopore structures by eliminating one phase in the two-phase VAN structures. Geometry nanopores control including the pore density and size can be achieved by: 1) adjusting the phase compositions or the deposition parameters to obtain different column widths in the VAN structures;[114] 2) optimizing the thermal treatment parameters such as annealing temperature and duration.

In this work, we present our initial success in processing nanoporous films by both furnace annealing and in situ heating experiments in a transmission electron microscope (TEM). The VAN system selected for this study is $(BFO)_{0.5}$:$(SmO)_{0.5}$ films for a demonstration. BFO has a melting point of 817~825^{o}C which is lower than that of SmO (2300^{o}C).[231-233] BFO could be decomposed and vaporized and ordered nanopores will be formed during annealing. The effects of annealing temperature on the new nanoporous structures were also investigated to explore the formation mechanisms of the nanopores.

7.3 Experimental

The template we selected to process nanoporous thin films in thermal treatment experiments is $(BFO)_{0.5}$:$(SmO)_{0.5}$ VAN thin films. With 50:50 phase ratios, both BFO and SmO phases show similar columnar width around 10nm and well-separated phase

locations in VAN thin film. As mentioned early in this dissertation, the $(BFO)_{0.5}$:$(SmO)_{0.5}$ VAN thin films were deposited on single crystal $SrTiO_3$(STO) (001) substrates in a pulsed laser deposition (PLD) system with a KrF excimer laser (Lambda Physik Compex Pro 205, λ= 248 nm). The laser beam was focused to obtain an energy density (4 J·cm^{-2}) at an incidence angle of 45°. The $(BFO)_{0.5}$:$(SmO)_{0.5}$ target were prepared by a conventional powder mixing method followed by target sintering with flowing oxygen (0.150 sccm). An optimized substrate temperature (650 ± 5°C) and an oxygen pressure of 0.2 torr were maintained during deposition. Other details can be found from previous literature.[114] The film thickness is controlled at 150 nm for this study.

The microstructure of the as-deposited and annealed films was characterized by X-ray diffraction (XRD) (BRUKER D8 powder X-ray diffractometer), scanning electron microscopy (SEM) (FEI SEM with Field Emission electron gun), atomic force microscopy (AFM) and high resolution TEM. A standard cross-section and plan-view TEM sample preparation procedures was used here including manual grinding and thinning of sample with a final ion milling step (PIPS 691 precision ion polishing system, 3.7 KeV).

Both of the conventional TEM characterization and in situ heating experiments were carried out using JEOL-2010 (LaB_6 electron gun) with stored Gatan ORIUS CCD camera and a point resolution of 2.34Å. In situ heating observation can be used to monitor the behavior, crystal structure and composition of the specimen while applying heat during the reaction. A Gatan-628 side entry, furnace type single tilt heating TEM

specimen holder was used for the in-situ heating experiment. This is a powerful tool in monitoring the microstructure evolution at atomic scale during the annealing process. The temperature was measured using a thermocouple attached to the furnace and the maximum operating temperature is 1300°C. Heating current as well as the ramping rate were carefully calibrated considering the temperature gap between specimen and thermal sensor. During the temperature rising up, electron beam was switched off to avoid the thermal radiation effect.

In this work, we conducted three different experiments of thermal treatment on $(BFO)_{0.5}$:$(SmO)_{0.5}$ VAN thin films: 1) ex situ sintering in tube furnace at 1000C for 1hr; 2) in situ heating in TEM from 25^{o}C to 850^{o}C; 3) ex situ sintering in tube furnace at 1000C for 4hrs on templates with different film thickness. We expected to achieve a nonporous thin film structure and investigated the possible factors that may affect such as temperature and film thickness during the process.

7.4 Results and discussion

7.4.1 Ex situ experiment

A set of $(BFO)_{0.5}$:$(SmO)_{0.5}$ VAN films with film thickness of 150 nm were processed at identical processing conditions for multiple annealing experiments. Figure 7.1 shows high-resolution TEM images from both cross-section (Figure 7.1a, b) and plan-view (Figure 7.1c, d) for an as-deposited $(BFO)_{0.5}$:$(SmO)_{0.5}$ thin film. A clear vertically aligned columnar structure was observed. BFO and SmO phases/columns are

alternating with each other. The average width of the BFO/SmO columns is around 10 nm. A remarkable feature of the $(BFO)_{0.5}$:$(SmO)_{0.5}$ films is the spontaneous phase ordering (Figure 7.1b, d). Both phases have grown epitaxially on $SrTiO_3$(STO) (001) substrate, evidenced by the distinguished diffraction dots from BFO and SmO phases in the corresponding selected area diffraction (SAD) pattern and Fast Fourier Transfer patterns (as inset). The orientation relationships are determined to be BFO(002)//SmO(004)//STO(002) and BFO(200)//SmO(220)//STO(200).

The $(BFO)_{0.5}$:$(SmO)_{0.5}$ VAN thin films were then ex situ annealed at various temperatures and durations to explore the annealing effects on the pore formation. The first annealing was at 1000°C for 1 hour. X-ray diffraction (XRD) was first conducted to explore the microstructure variation introduced by high temperature annealing. Obvious differences can be found from the XRD data in Figure 7.2 for both the as-deposited VAN thin films and the sample after annealing. For the as-deposited sample, both BFO and SmO phases have grown highly textured mainly along STO(*00l*) direction. After annealing, the main peaks are indexed as SmO (*00l*) peaks and no obvious BFO(*00l*) peaks observed. This indicates that a large amount of BFO phase has decomposed and evaporated during the high temperature annealing and SmO is the major phase left in the annealed sample. The intensity of SmO(800) peak was increased after the thermal treatment which suggests that high temperature annealing also improves the SmO phase crystallinity at the same time of the pore formation.

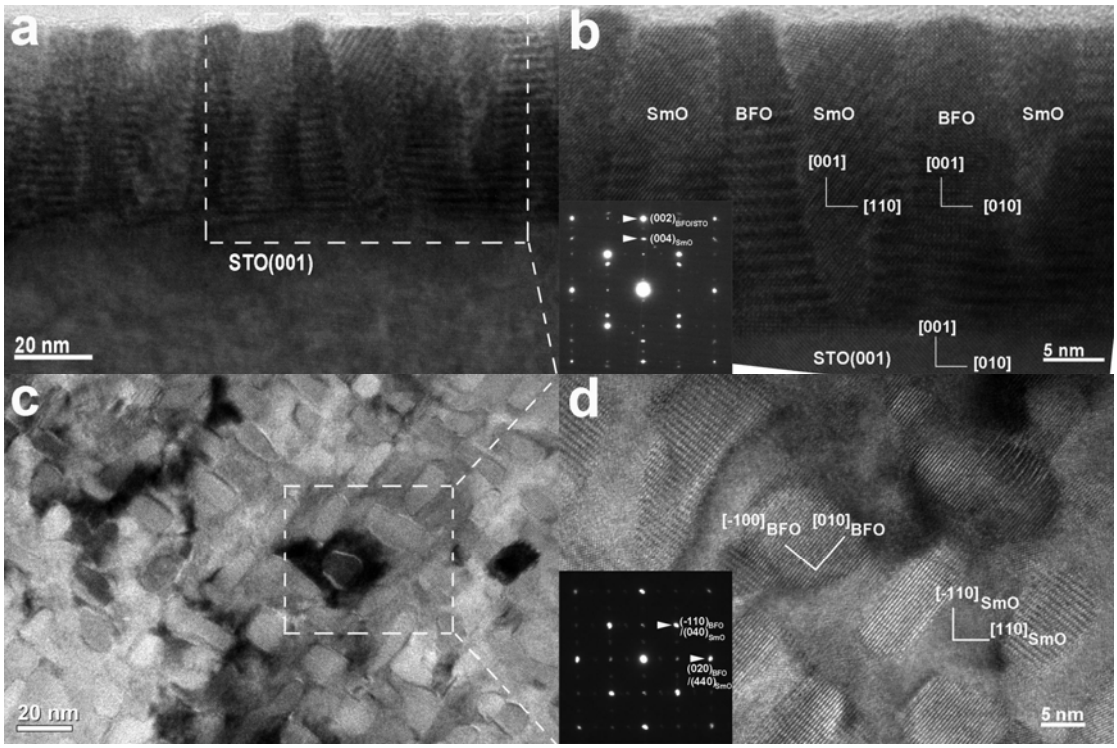

FIG 7.1. TEM analysis on $(BFO)_{0.5}$:$(SmO)_{0.5}$ VAN thin films. (a) Cross-section TEM images of $(BFO)_{0.5}$:$(SmO)_{0.5}$ VAN thin film with (b) zoom-in high resolution TEM images and the corresponding selected-area diffraction pattern as inset; (c) plan-view TEM image of $(BFO)_{0.5}$:$(SmO)_{0.5}$ VAN thin film with (d) zoom-in high resolution TEM image and the corresponding selected-area diffraction pattern as inset. The epitaxial orientation relationships are determined to be BFO(002)//SmO(004)//STO(002) and BFO(200)// SmO(220)// STO(200).

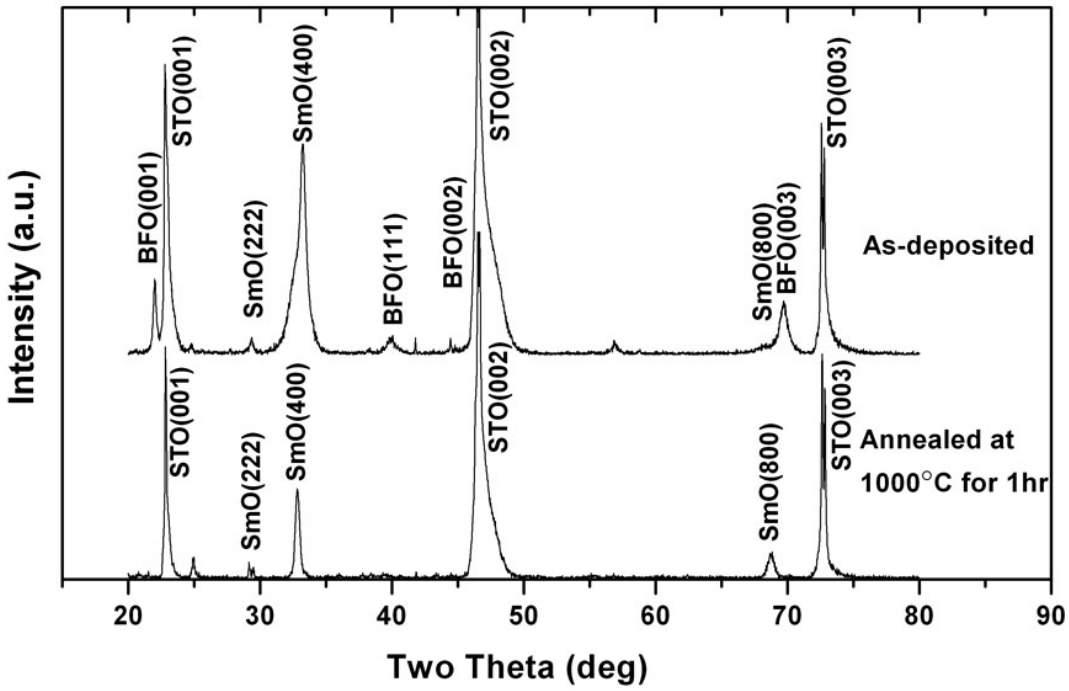

FIG 7.2. XRD θ~2θ scans of $(BFO)_{0.5}$:$(SmO)_{0.5}$ nanocomposite thin films before and after 1000°C 1hr annealing.

Microstructures of the annealed $(BFO)_{0.5}$:$(SmO)_{0.5}$ thin films were examined by using cross-section TEM. One such image in Figure 7.3a shows that highly ordered nanopores have formed in the film with an average pore diameter of 60 nm for the ones close to the film-substrate interface and of 150nm for the ones on the top of the film. High temperature annealing on $(BFO)_{0.5}$:$(SmO)_{0.5}$ VAN thin films forms a unique bi-layer nanopore structure. The spacing between the neighboring pores is around 50nm for both layers of pores. Based on the pore size and distribution, the estimated total

film porosity is around 40%. The corresponding selected area diffraction (SAD) pattern of both film and substrate shown in Figure 7.3b demonstrate the highly epitaxial SmO phase in the annealed film without clear diffractions from BFO. This observation is consistent with the above XRD result. The fast Fourier-transformed patterns processed from selected areas in the high resolution TEM image also suggest that the majority of the phase is SmO with only very small portion of areas identified as BFO.

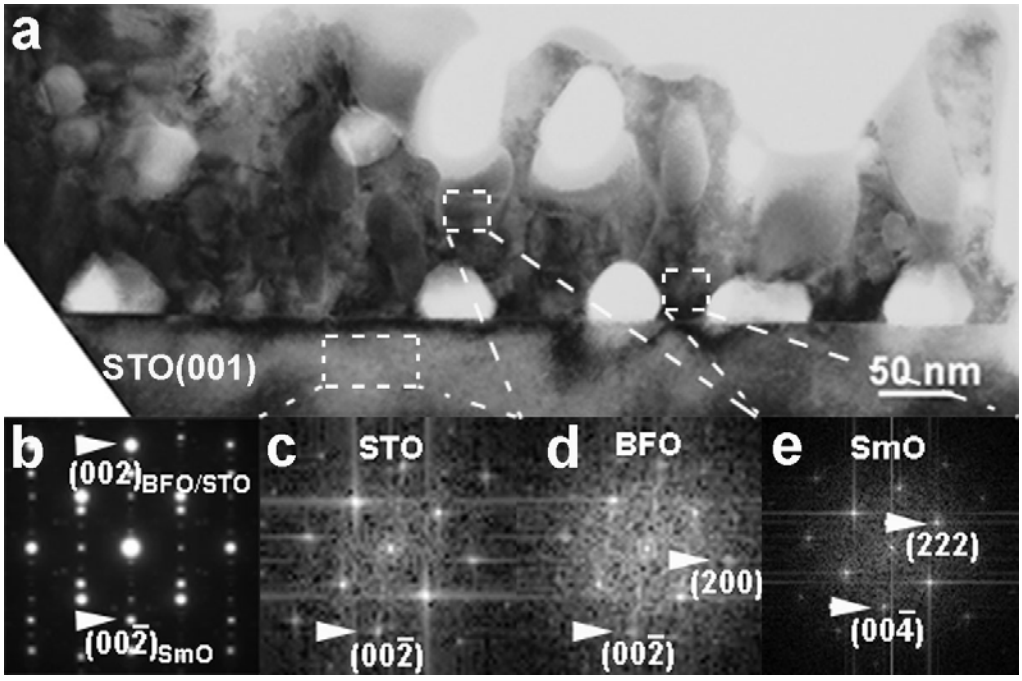

FIG 7.3. TEM image of $(BFO)_{0.5}$:$(SmO)_{0.5}$ nanocomposite thin film after 1000°C 1hr annealing showing bi-layer porous microstructure. Below are (b) selected-area diffraction pattern from both the film and the substrate; and fast Fourier transfer patterns from (c) STO substrate; (d) BFO region; (e) SmO region.

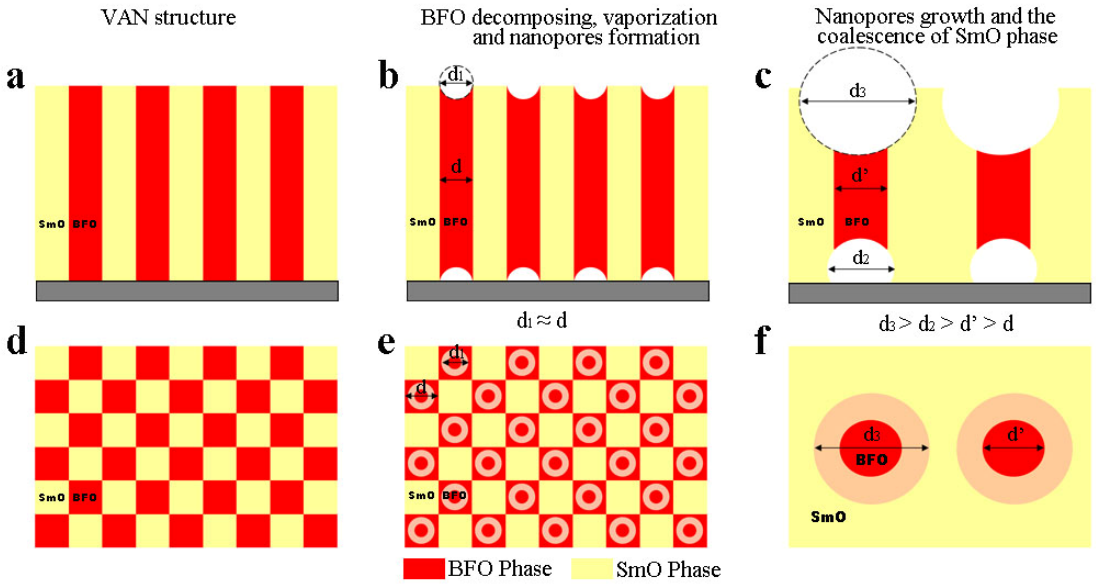

FIG 7.4. Schematic diagrams illustrate a possible pore formation mechanism in $(BFO)_{0.5}$:$(SmO)_{0.5}$ nanocomposite during high temperature annealing. a-c are cross-section view; d-f are plan-view. Areas in red correspond to BFO phase and areas in yellow correspond to SmO phase. a and d illustrates the initial VAN structure with a diameter of *d*. b and e represent the initial decomposing and vaporization process with pore size $d_1=d$. C and f describe the nanopore growth and the coalescence of SmO phase ($d_3 > d_2 > d_1$). *d* is the width of BFO columns before phase coalescence; d_1 is the diameter of the top open and bottom closed pores during annealing; d_2 is the diameter of bottom closed pores after annealing; d_3 is the diameter of top open pores after annealing; *d'* is the width of BFO column left after phase coalescence.

This unique porous structure is mainly related to the original spontaneously ordered vertical columnar structure of the VAN template. Through annealing, the well aligned vertical nanocolumnar structure has been converted into nanoporous film with ordered nanopores uniformly distributed. The diameter of the pores is approximately 6 times of the column width in the as-deposited VAN films. Due to the different melting temperatures of BFO (T_m=817~825^{o}C) and SmO (T_m=2300^{o}C), BFO will decompose and evaporate first before SmO starts to decompose. The schematics in Figure 7.4 show the possible scenario for the pore formation during annealing from both cross-section (a, b, c) and plan-view (d, e, f). During the high temperature annealing (1000^{o}C), the BFO phase went through decomposing – vaporization – diffusion process while the SmO phase went through reconstruction. The top open pores came from the BFO phase vaporization on the top portion of the BFO columns, and the bottom closed pores were formed through the BFO phase decomposition and diffusion to free space (Figure 7.4b and e, $d_1 \approx d$). The closed pores at the film-substrate interface are typically smaller than the open pores on the top of the film since the bottom pore formation is also limited by the diffusion process (Figure 7.4c and f, $d_3 > d_2$).

During the decomposition and vaporization of BFO, SmO columns (as well as a small amount of residual BFO phase) may have combined together formed more continuous frames with much larger nanopores (Figure 7.4c and f, $d' > d$). High resolution SEM image in Figure 7.5a presents the surface pore density of the annealed film. These surface pores are the ones shown on the top layer in the annealed film (shown in Figure 7.3a). Based on the contrast difference (area with dark contrast

corresponding to pores), the surface porosity is estimated to be 35% which is close to the value estimated by the cross-section TEM study. The distribution of the surface pores size is plotted in Figure 7.5b. Most of the surface pores are in the range 100~200nm which are larger than the ones at the substrate-film interface. AFM scanning on the nanoporous thin film sample (not shown here) also confirmed that the average diameter of the top pores is around 150 nm and with 30 nm in depth.

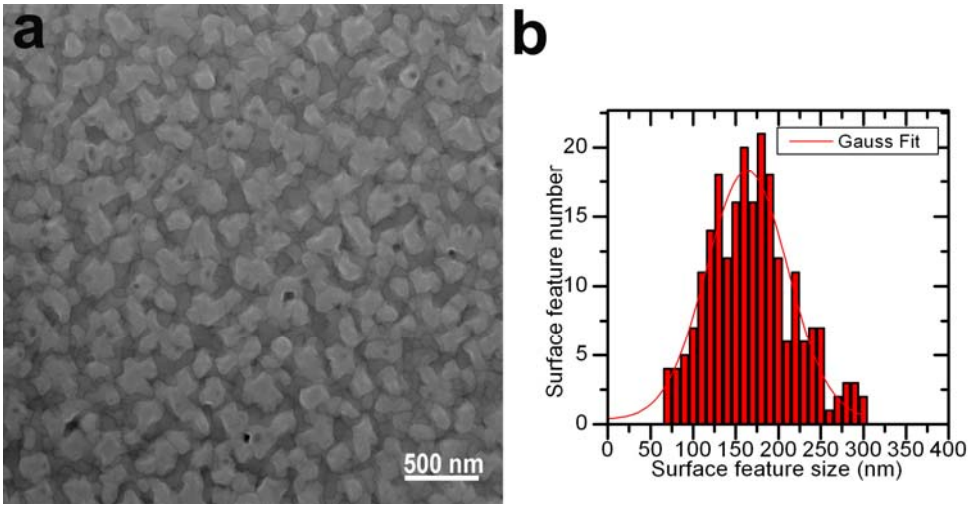

FIG 7.5. (a) High resolution scanning electron microscopy analysis on 1000°C 1hr annealed $(BFO)_{0.5}$:$(SmO)_{0.5}$ nanocomposite thin film show ordered nanopores on film surface. (b) Surface pore density distribution reveals the average pore size of about 150nm.

7.4.2 In situ experiment in TEM

To fully understand this bi-layer nanopores structure formation mechanism during the annealing process, we conducted in situ heating experiments in TEM. It is a powerful tool in monitoring the microstructure evolution at atomic scale during the annealing process. It is noted that the in situ annealing experiment deals with a semi 2D sample foil (with foil thickness around 50-100nm depending on the regions in the foil) which might not completely represent the formation mechanisms of the 3D sample. However this in situ experiment can at least reveal the decomposition and evaporation process of the BFO phases in real time. The movie snapshots from the two-stage annealing, from 25°C to 600°C and from 600°C to 850°C, are shown in Figure 7.6a and b, respectively. During the experiment, ramping rate was gently controlled to avoid the sharp temperature difference between the TEM specimen and the sample stage. From 25°C to 600°C (Figure 7.6a), there is no obvious evaporation observed until the temperature raised up to 600°C with some indication of decomposition and vaporization of BFO phases. From 600°C to 850°C, as shown in Figure 7.6b, the snapshots show obvious material evaporation and structure variation during the annealing process. It is clear that the vaporization of the BFO phases starts uniformly throughout the BFO columns. Starting from 750^{o}C, the majority of the BFO phases has vaporized and left nanopores along the sides of the SmO columns. The SmO columns are largely intact.

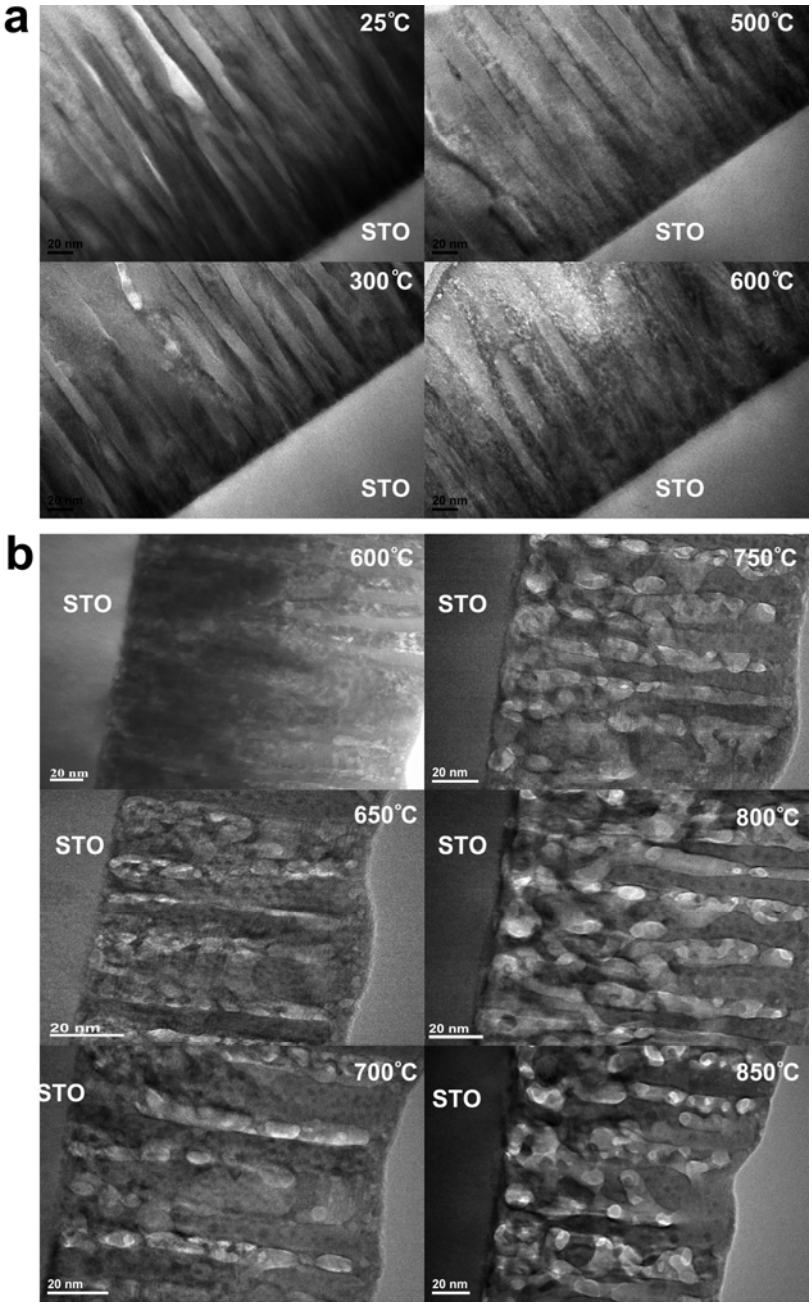

FIG 7.6. In situ heating cross-section TEM analysis on $(BFO)_{0.5}$:$(SmO)_{0.5}$ VAN thin films. (a) Snapshots taking during temperature ramping from room temperature to 600°C. No obvious decomposition and evaporation observed. (b) Snapshots taking from 600°C to 850°C show the sequence of decomposition, evaporation and pore recombination.

Different from the ex situ annealed sample in Figure 7.3, the vaporization of BFO nanopores did not alter the SmO nanocolumns during the in situ experiments. It shows that the well-separated individual nanopores did not coalesce at lower temperature from 650°C to 750°C. Starting from 750 °C to 850°C, the nanopores start to coalesce with the neighboring ones and the SmO nanocolumns begin to lose their vertical alignment and form larger SmO grains around the nanopores.

It is worth to point out that the experimental temperature is lower than the melting temperature of SmO. This suggests that there is a significant amount of materials diffusion promoted by the extra thermal energy, the energy stored at the nanocolumn boundaries and the surface energy of nanopores, which results in the coalescence of the SmO grains even around 800°C. This in situ heating experiment definitely provides useful information for understanding the annealing process and provides a clear insight that it is possible to process ordered vertically aligned nanopores by precisely controlling the annealing process on the VAN structure.

Regarding the materials system selection, a large number of VAN structures have been demonstrated up-to-date.[37,68,100,103,114,230] This gives a vast choice in the material selection of the nanoporous structures. Besides annealing, the secondary phase can be removed by chemical etching or other approaches which are currently under investigation.

7.4.3 Film thickness effect

Above work shows that 1 hour ex situ sintering at 1000°C on $(BFO)_{0.5}$:$(SmO)_{0.5}$ VAN thin films provide a chance to achieve novel bi-layered nanoporous thin film. It will be interesting to investigate the annealing effect with different VAN $(BFO)_{0.5}$:$(SmO)_{0.5}$ film thickness or different thermal treatment duration. From the thermal dynamic point of view, thinner as-deposited film thickness and longer sintering will cause more intensive reactions and film microstructure evolution. In this work, we conducted ex situ high temperature annealing on a set of $(BFO)_{0.5}$:$(SmO)_{0.5}$ VAN thin films for 4hr at 1000°C with different film thickness (25nm; 50nm; 100nm and 150nm). After 4hrs high temperature annealing at 1000°C, $(BFO)_{0.5}$:$(SmO)_{0.5}$ VAN thin films with different film thickness shows different microstructures (as shown in Figure 7.7). For 25nm sample, it is obviously to see both BFO and SmO formed continuous layers aligned alternatively on STO substrate with 100nm alternation. SmO layers were thicker than BFO layers since part of BFO phase has decomposed and evaporated out during the high temperature annealing. For 50nm samples, we found SmO cumulus aligned alternatively with 100nm distance in between on top of BFO continuous layer. It can be found that there is already some BFO layers formed on the bottom below the edge of the SmO layers for annealing at 25nm films. And for the 50nm thin films, after the thermal treatment, all BFO were formed as continuous layer on top of STO substrate with SmO cumulus aligned on the top.

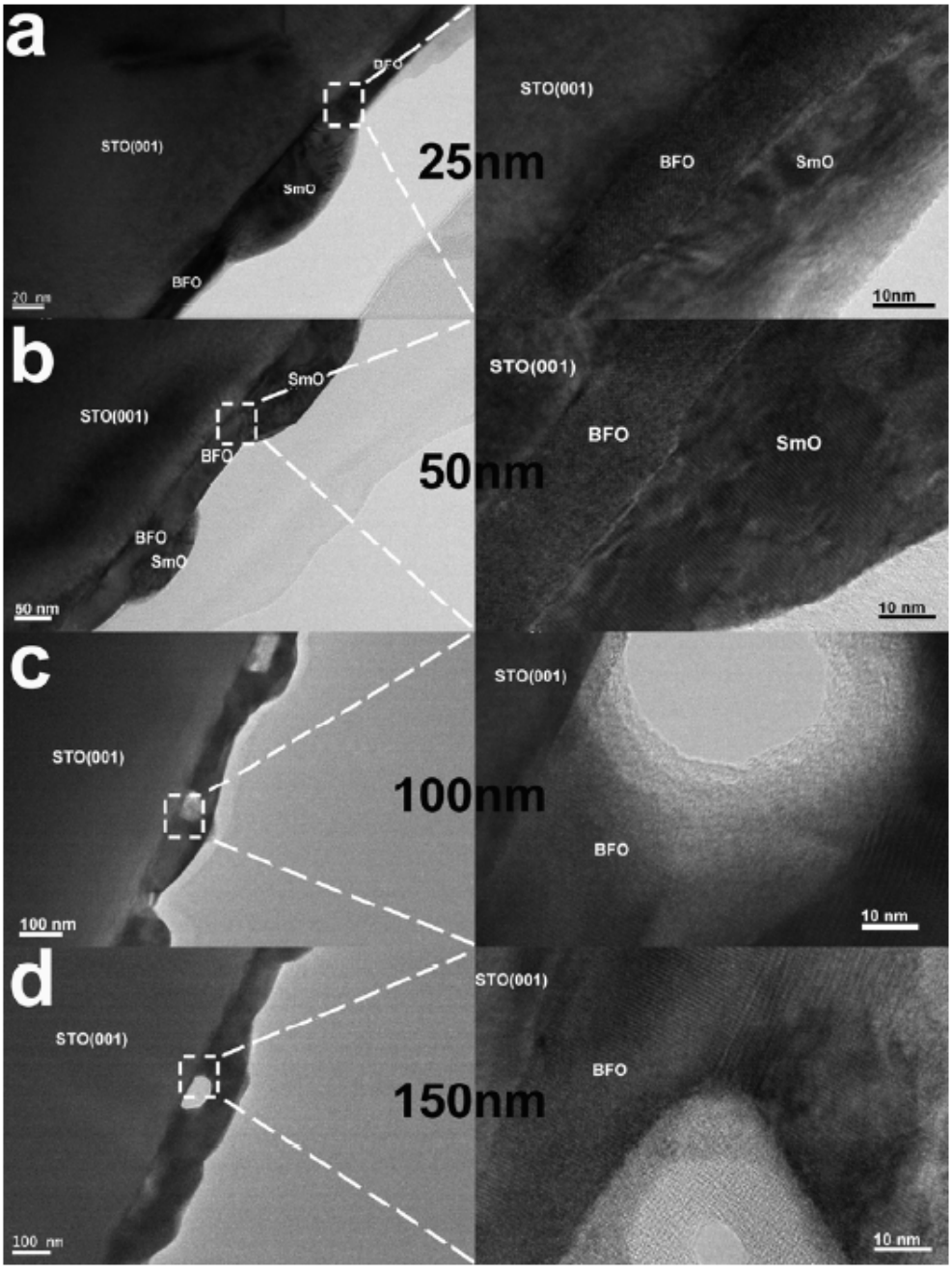

FIG 7.7. Cross-section TEM image of 1000°C 4hr annealed BFO:SmO thin film on STO(001) substrate with different film thickness. A) 25nm; b)50nm; c)100nm; d)150nm. Right columns are high magnification TEM images corresponding to left square areas.

All BFO and SmO phases were highly epitaxial layers or cumulus, and we can see there were no columnar structures anymore after 4 hr 1000°C sintering on 50nm films. For 100nm and 150nm thick $(BFO)_{0.5}$:$(SmO)_{0.5}$ thin films, nanopores started to formed alternatively on STO substrate with 200nm alternation distance after thermal treatment. Right selective area higher magnification TEM images corresponding to Figure 7.7c and d show the pores have a dimension of 100nm in diameter and with BFO phase rounded. There were no obvious regularly aligned VAN columnar structures within the film thickness but only epitaxial BFO and SmO phases mixed with each other.

Compared with samples annealed 1hr at 1000°C, longer annealing duration (4hr) can get larger pores size (2 times in diameter). Above thickness series annealed BFO:SmO thin films analysis can help understanding the two phases VAN microstructure evolution mechanism at high annealing temperature. For thinner $(BFO)_{0.5}$:$(SmO)_{0.5}$ VAN thin films (<25nm), the columns height-width ratio is small (<4). During the 1000°C annealing, BFO will decompose and vaporize out, lose its vertical aligned columnar structure and form continuous layers. SmO will accumulate to cumulus with losing its originally vertical aligned columnar boundaries and recombined to nearby columns. They will form a SmO/BFO/STO multilayered structure because of the relative higher kinetic movement activity of BFO. Besides the vertical atom movement within BFO, there is also a horizontal atom movement within BFO continuous layer since the high evaporation rate on exposed BFO layer. This horizontal density grad will cause BFO atoms move from the middle of SmO/BFO/STO sandwich structures to the BFO/STO single layer area. Finally, the

SmO cumulus on STO substrate within BFO continuous layers (matrix) formed. With thicker $(BFO)_{0.5}$:$(SmO)_{0.5}$ thin films (25-100nm), larger height-width ration (4-14), the evaporation rate will be same but with more BFO content compared with thinner $(BFO)_{0.5}$:$(SmO)_{0.5}$ thin films which will cause the SmO cumulus on BFO continuous layer structure. More BFO content can provide enough materials to form continuous layer even below the SmO cumulus. For even thicker $(BFO)_{0.5}$:$(SmO)_{0.5}$ thin films (>100nm), with even larger heigh-width ratio(>15), the phase with relative larger kinetic movement activity (BFO phase) can not gain enough energy to totally break up the column boundaries limitation with 4hr 1000°C annealing. This will cause closed pores formed at the bottom of BFO:SmO thin films aligned alternatively and two epitaxial phases mixed with each other through the film thickness. Compared with Figure 7.3a and Figure 7.7c and d, it is reasonable to see that with longer thermal treatment duration, the porous size getting larger and the VAN structure getting lost. This demonstrates larger annealing energy introduced into the two phases VAN system is helpful to eliminate the column boundaries. And with thinner $(BFO)_{0.5}$:$(SmO)_{0.5}$ thin films, same amount of introduced annealing energy can not only counteract the column boundaries but also help reorganize separated phases to continuous layers.

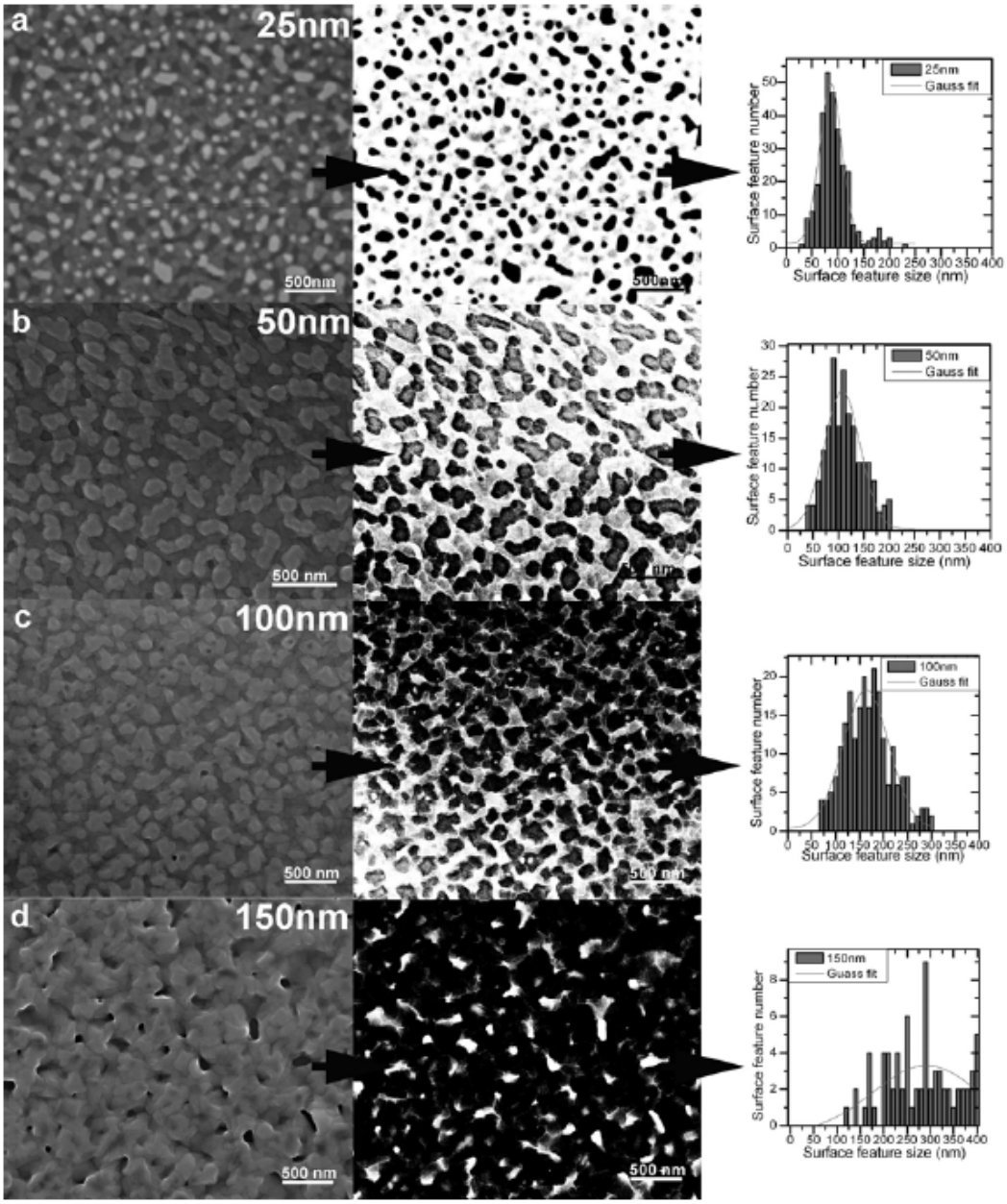

FIG 7.8. SEM images of 1000°C 4hr annealed BFO:SmO thin film on STO(001) substrate with different film thickness. A) 25nm; b) 50nm; c)100nm and d) 150nm. The middle column are corresponding contrast converted images by using IPP software for surface feature size analysis. Right column are corresponding surface feature size analysis with Gauss fit curve.

Figure 7.8 gives the surface morphology analysis on the thickness series $(BFO)_{0.5}$:$(SmO)_{0.5}$ VAN thin films annealed at 1000°C for 4 hrs. 25nm and 50nm thickness annealed samples showed bright color SmO cumulus accumulate on top of BFO dark layers. With less BFO content, 25nm annealed sample showed an uncontinuous layer while there is more consecutive BFO bottom layer in 50nm annealed sample that can be found from Figure 7.8a and b. 50nm and 100nm thickness annealed samples show similar surface morphology from Figure 7.8b and c. All bright SmO cumulus accumulated on top of continuous BFO layer but it is notable to see porous cavities started to form within the bottom continuous BFO layer in 100nm thick sample. The SEM image of 150nm annealed BFO:SmO shows more continuous mixed two phases layer with clearly open pores on surface and closed pores on the bottom.

The nanoporous thin film surface 2D porosity analysis shows a porosity decrease from 84.3% to 3.7% as the film thickness increase from 25nm to 150nm in Figure 7.9. This plotting suggests that the film thickness also play an important role in achieving a controllable porosity within the two phases VAN thin films.

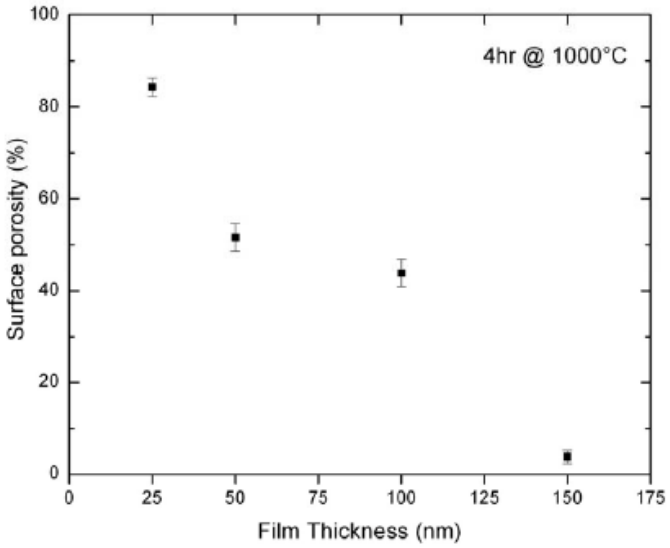

FIG 7.9. Surface porosity of thickness series BFO:SmO thin films annealed at 1000°C for 4hrs which calculated based on the HRSEM analysis.

7.4.4 Thermal treatment duration effect

Another factor that may affect the nanoporous structure is the annealing duration. We select the 150nm $(BFO)_{0.5}$:$(SmO)_{0.5}$ VAN thin films as templates and conducted ex situ thermal treatment at 1000^{o}C for different duration (0.5hr, 1hr and 1.5hr). High resolution SEM analysis show in Figure 7.10 reveals that different annealing duration will cause different microstructure in the nanoporous thin films. As the annealing duration increased from 0.5 hr to 1 hr, the surface nanopores dimension increased from 50nm to 100nm. In the meanwhile the nanoporous thin film surface porosity, which

can be identified from Figure 7.11, also increases from 13% to 32%. With even longer annealing duration for 1.5hr, it is interesting to see closed surface pores former. The open area is with similar size as compared with that of the 1hr annealed case, however it is clear to see an enlarged pore formed right below the film surface. The surface porosity dropped to 5%, however it comes with an enlarged top pores in the bilayer nanoporous thin films.

Above electron microscopy analysis on thermal treatment duration series annealed $(BFO)_{0.5}$:$(SmO)_{0.5}$ VAN thin films demonstrate that the nanopores will grow with longer thermal treatment, especially for the top pores. However, after a period of annealing, SmO will lose its original columnar structure, and collapse to form a continued surface layer. The decreased open region of the top pores may cause a lower efficient for the nonoporous thin films working as membrane or catalysis.

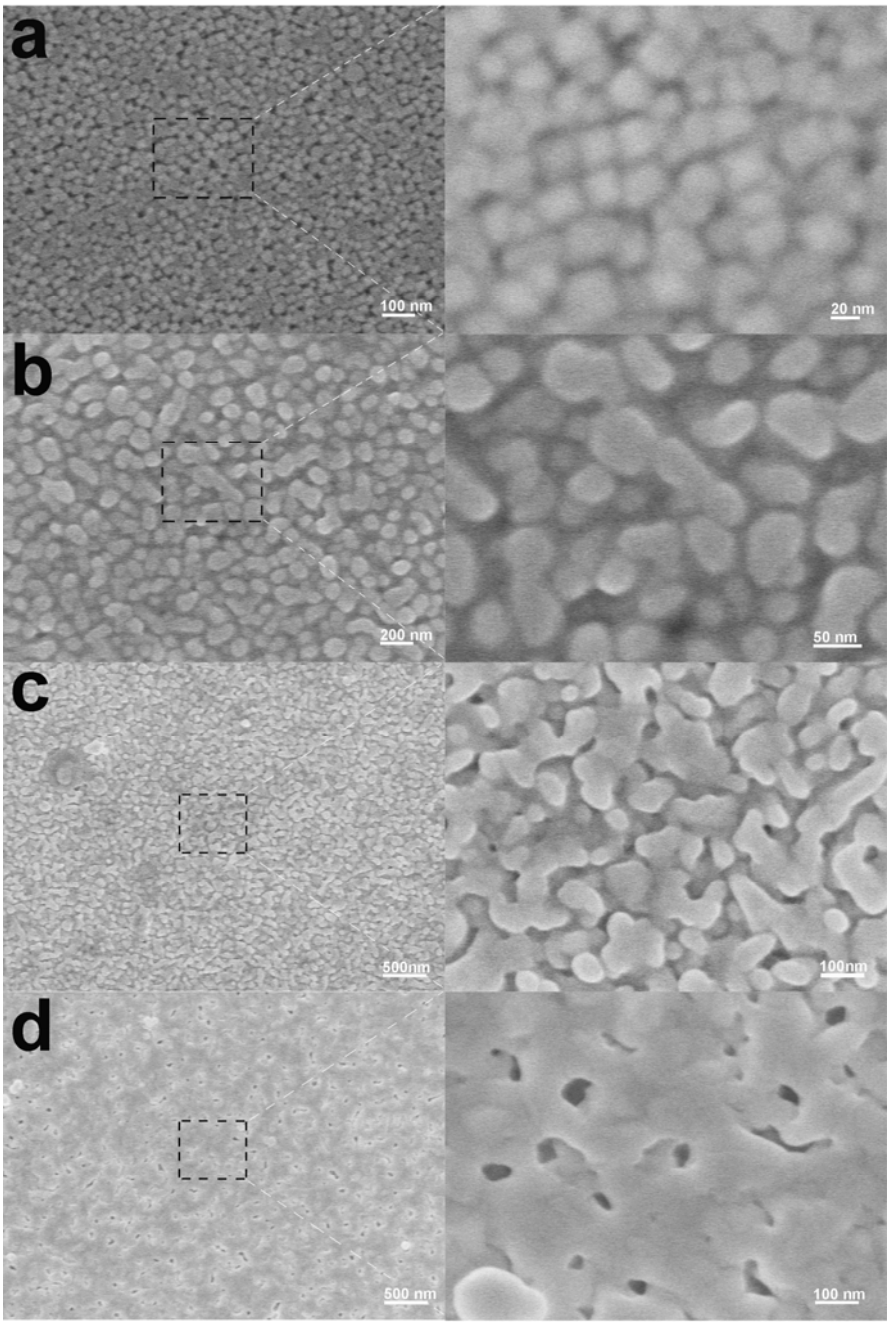

FIG. 7.10. SEM images of 1000°C annealed BFO:SmO thin film on STO(001) substrate with different annealing duration. a) as deposited; b) 0.5 hr annealed; c)1hr annealed and d) 1.5hr annealed. Right column are corresponding zoomed in picture for surface feature analysis.

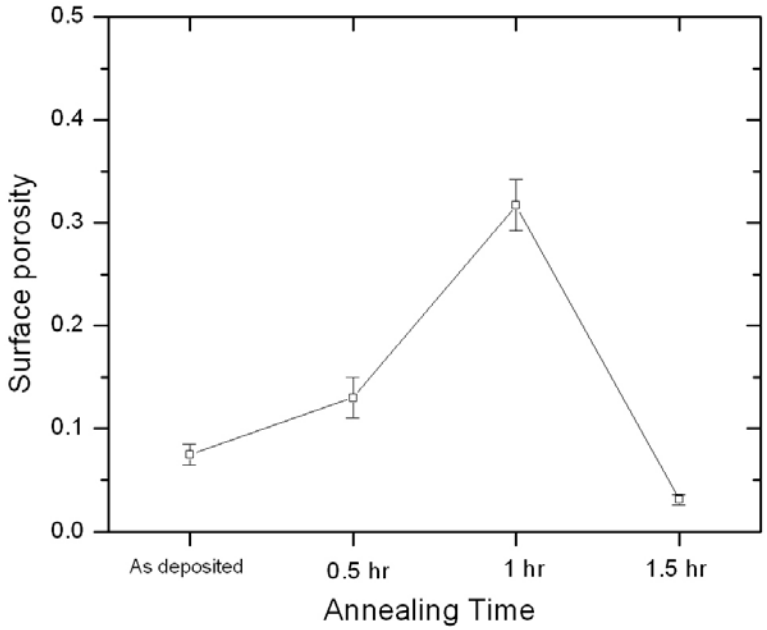

FIG 7.11. Surface porosity of the nanoporous thin films after different thermal treatment duration.

7.5 Conclusions

In summary, we have presented a new approach in processing nanoporous thin film with ordered nanopores from $(BFO)_{0.5}$:$(SmO)_{0.5}$ VAN thin films. High resolution TEM reveals that, after annealing at 1000^{o}C for 1 hour, a bi-layer nanopore structure with open pores on top and closed pores on bottom has formed. In situ heating

experiment in TEM demonstrates that the BFO phases went through a decomposition – vaporization – diffusion process starting from 600^{o}C while SmO phases remain mostly intact. Above 750^{o}C, the nanopores start to coalesce into large pores and the SmO columns start to recombine into large grains around the nanopores. Besides, the thickness of the VAN thin film template and the thermal treatment duration all have been proved to be very important factors that will affect the final nanoporous microstructure. This demonstrates that it is feasible to process vertically aligned nanopores or nanoporous films with controlled nanopore density by controlling the annealing process of VAN structures.

CHAPTER VIII

SUMMARY AND FUTURE WORK

In this dissertation, we performed a systematic study on the vertically aligned nanocomposite oxide thin films. This is an exciting approach and brand new architecture in thin films that promises tunable material functionalities as well as novel nanostructures.

Tunable strain control and physical properties have been demonstrated in BFO:SmO and LSMO:Mn_3O_4 VAN thin film systems by varying the film deposition parameters and the phase compositions. The growth mechanism study on MgO:STO and BFO:SmO VAN systems reveals that both the substrate induced strain and phase composition play important roles in determining the morphology and microstructures of nanocomposite thin films. Ex-situ thermal treatment and in-situ heating experiment in TEM illustrate the feasibility of processing nanoporous thin films with controllable nanopores by using VAN thin film as templates.

Vertically aligned nanocomposite architecture is generic to achieve multifunctionalities and novel nanostructures in thin films. This work also suggests a promising avenue in strain engineering in functional nanocomposite oxide thin films.

Further work can be carried out to address below questions:

1. Is that possible to promote VAN architecture from oxide material to others? What are the critical factors that will restrict this transition?

2. How can the morphology of VAN thin films be controlled as checkerboard in-plane instead of doped columns? Which one is better for precise strain control and device applications?

3. What is the atomistic process in the early stage of VAN thin films growth?

4. How can the self-assembled nanostructures or devices be processed based on VAN architecture? How to selectively eliminate one of the phases?

REFERENCES

[1] Z. L. Wang and Z. C. Kang, *Functional and Smart Materials: Structural Evolution and Structure Analysis* (Putnam, New York, 1998).

[2] M. Tsuchiya, S. K. R. S. Sankaranarayanan, and S. Ramanathan, Progress in Materials Science **54,** 981-1057 (2009).

[3] D. Smyth, *The Defect Chemistry of Metal-oxides* (Oxford University Press, New York, 2000).

[4] C. N. R. Rao and B. Raveau, *Transition Metal Oxides: Structure, Properties, and Synthesis of Ceramic Oxides*, 2nd ed. (Wiley-VCH, New York, 1998).

[5] L. W. Martin, Y. H. Chu, and R. Ramesh, Materials Science & Engineering R: Reports **68,** 89-133 (2010).

[6] A. M. Haghiri-Gosnet and J. P. Renard, Journal of Physics D-Applied Physics **36,** 127-150 (2003).

[7] J. Wang, J. B. Neaton, H. Zheng, V. Nagarajan, S. B. Ogale, B. Liu, D. Viehland, V. Vaithyanathan, D. G. Schlom, U. V. Waghmare, N. A. Spaldin, K. M. Rabe, M. Wuttig, and R. Ramesh, Science **299,** 1719-1722 (2003).

[8] S. Komarneni, Journal of Materials Chemistry **2,** 1219-1230 (1992).

[9] B. Abeles, Applied Solid State Science **6,** 1-117 (1976).

[10] D. Shi, *Functional Thin Films and Functional Materials – New Concepts and Technologies* (Springer, New York, 2003).

[11] S. A. Chambers, Advanced Materials **22,** 219-248 (2010).

[12] J. Maier, Nature Materials **4,** 805-815 (2005).

[13] A. Karthikeyan, M. Tsuchiya, C. L. Chang, and S. Ramanathan, Applied Physics Letters **90,** 263108 (2007).

[14] M. G. Blamire, J. L. MacManus-Driscoll, N. D. Mathur, and Z. H. Barber, Advanced Materials **21,** 3827-3839 (2009).

[15] D. C. Look, Materials Science and Engineering B-Solid State Materials for Advanced Technology **80,** 383-387 (2001).

[16] A. Tsukazaki, A. Ohtomo, T. Onuma, M. Ohtani, T. Makino, M. Sumiya, K. Ohtani, S. F. Chichibu, S. Fuke, Y. Segawa, H. Ohno, H. Koinuma, and M. Kawasaki, Nature Materials **4,** 42-46 (2005).

[17] U. Ozgur, Y. I. Alivov, C. Liu, A. Teke, M. A. Reshchikov, S. Dogan, V. Avrutin, S. J. Cho, and H. Morkoc, Journal of Applied Physics **98,** 041301 (2005).

[18] J. F. Muth, R. M. Kolbas, A. K. Sharma, S. Oktyabrsky, and J. Narayan, Journal of Applied Physics **85,** 7884-7887 (1999).

[19] J. J. Hopfield, Journal of Physics and Chemistry of Solids **15,** 97-107 (1960).

[20] J. L. Snoek, *New Development in Ferromagnetic Materials* (Elsevier, New York, 1947).

[21] J. Stohr and H. C. Siegmann, *Magnetism, from Fundamentals to Nanoscale Dynamics* (Springer - Verlag, New York, 2006).

[22] P. W. Anderson, Physical Review **79,** 350-356 (1950).

[23] C. Zener, Physical Review **82,** 403-405 (1951).

[24] K. Yosida, Physical Review **1,** 893-898 (1957).

[25] J. M. D. Coey, M. Viret, and S. von Molnar, Advances in Physics **58,** 567-569 (2009).

[26] C. Zener, Physical Review **83,** 299-301 (1951).

[27] K. Chahara, T. Ohno, M. Kasai, and Y. Kozono, Applied Physics Letters **63,** 1990-1992 (1993).

[28] R. Vonhelmolt, J. Wecker, B. Holzapfel, L. Schultz, and K. Samwer, Physical Review Letters **71,** 2331-2333 (1993).

[29] A. J. Millis, P. B. Littlewood, and B. I. Shraiman, Physical Review Letters **74,** 5144-5147 (1995).

[30] X. L. Wang, S. X. Dou, H. K. Liu, M. Ionescu, and B. Zeimetz, Applied Physics Letters **73,** 396-398 (1998).

[31] M. Bibes, M. Bowen, A. Barthelemy, A. Anane, K. Bouzehouane, C. Carretero, E. Jacquet, J. P. Contour, and O. Durand, Applied Physics Letters **82,** 3269-3271 (2003).

[32] R. Mahesh, R. Mahendiran, A. K. Raychaudhuri, and C. N. R. Rao, Applied Physics Letters **68,** 2291-2293 (1996).

[33] T. Walter, K. Dorr, K. H. Muller, B. Holzapfel, D. Eckert, M. Wolf, D. Schlafer, L. Schultz, and R. Grotzschel, Applied Physics Letters **74,** 2218-2220 (1999).

[34] S. L. Cheng and J. G. Lin, Journal of Applied Physics **98,** 114318 (2005).

[35] A. Gupta, G. Q. Gong, G. Xiao, P. R. Duncombe, P. Lecoeur, P. Trouilloud, Y. Y. Wang, V. P. Dravid, and J. Z. Sun, Physical Review B **54,** 15629-15632 (1996).

[36] O. I. Lebedev, J. Verbeeck, G. Van Tendeloo, O. Shapoval, A. Belenchuk, V. Moshnyaga, B. Damashcke, and K. Samwer, Physical Review B **66,** 104421 (2002).

[37] B. S. Kang, H. Wang, J. L. MacManus-Driscoll, Y. Li, Q. X. Jia, I. Mihut, and J. B. Betts, Applied Physics Letters **88,** 192514 (2006).

[38] Z. Bi, E. Weal, H. Luo, A. Chen, J. Driscoll, Q. Jia, and H. Wang, Journal of Applied Physics **109,** 054302 (2011).

[39] F. Jona and G. Shirane, *Ferroelectric Crystals* (Pergamon Press, New York, 1962).

[40] H. D. Megaw, *Ferroelectricity in Crystals* (Methuen, London, 1957).

[41] B. Jaffe, W. R. Cook, and H. Affe, *Piezoelectric Ceramics* (Academic Press, London, 1971).

[42] W. D. Kingery, H. W. Bowen, and D. R. Uhlmann, *Introduction to Ceramics*, 2nd ed. (Wiley, New York, 1976).

[43] T. Tybell, C. H. Ahn, and J. M. Triscone, Applied Physics Letters **75,** 856-858 (1999).

[44] D. G. Schlom, L. Q. Chen, C. B. Eom, K. M. Rabe, S. K. Streiffer, and J. M. Triscone, Annual Review of Materials Research **37,** 589-626 (2007).

[45] Y. L. Li and L. Q. Chen, Applied Physics Letters **88,** 072905 (2006).

[46] Y. H. Chu, Q. Zhan, L. W. Martin, M. P. Cruz, P. L. Yang, G. W. Pabst, F. Zavaliche, S. Y. Yang, J. X. Zhang, L. Q. Chen, D. G. Schlom, I. N. Lin, T. B. Wu, and R. Ramesh, Advanced Materials **18,** 2307-2311 (2006).

[47] I. Vrejoiu, M. Alexe, D. Hesse, and U. Gosele, Advanced Functional Materials **18,** 3892-3906 (2008).

[48] V. Nagarajan, C. L. Jia, H. Kohlstedt, R. Waser, I. B. Misirlioglu, S. P. Alpay, and R. Ramesh, Applied Physics Letters **86,** 184104 (2005).

[49] C. L. Jia, S. B. Mi, K. Urban, I. Vrejoiu, M. Alexe, and D. Hesse, Nature Materials **7,** 57-61 (2008).

[50] W. Li and M. Alexe, Applied Physics Letters **91,** 262903 (2007).

[51] P. Paruch, T. Tybell, and J. M. Triscone, Applied Physics Letters **79,** 530-532 (2001).

[52] J. Junquera and P. Ghosez, Nature **422,** 506-509 (2003).

[53] A. Stanishevsky, B. Nagaraj, J. Melngailis, R. Ramesh, L. Khriachtchev, and E. McDaniel, Journal of Applied Physics **92,** 3275-3278 (2002).

[54] W. Lee, M. Alexe, K. Nielsch, and U. Gosele, Chemistry of Materials **17,** 3325-3327 (2005).

[55] M. Dawber, K. M. Rabe, and J. F. Scott, Reviews of Modern Physics **77,** 1083-1130 (2005).

[56] R. Ramesh and N. A. Spaldin, Nature Materials **6,** 21-29 (2007).

[57] L. Martin, S. P. Crane, Y. H. Chu, M. B. Holcomb, M. Gajek, M. Huijben, C. H. Yang, N. Balke, and R. Ramesh, Journal of Physics-Condensed Matter **20,** 434220 (2008).

[58] E. Ascher, H. Rieder, H. Schmid, and H. Stossel, Journal of Applied Physics **37,** 1404-1405 (1966).

[59] A. Loidl, H. von Loehneysen, and G. M. Kalvius, Journal of Physics-Condensed Matter **20,** 430301 (2008).

[60] D. Khomskii, Physics **2,** 20-28 (2009).

[61] T. Kimura, T. Goto, H. Shintani, K. Ishizaka, T. Arima, and Y. Tokura, Nature **426,** 55-58 (2003).

[62] C. A. F. Vaz, J. Hoffman, C. H. Anh, and R. Ramesh, Advanced Materials **22,** 2900-2918 (2010).

[63] W. Eerenstein, F. D. Morrison, J. Dho, M. G. Blamire, J. F. Scott, and N. D. Mathur, Science **307,** 1203-1203 (2005).

[64] H. Bea, M. Bibes, A. Barthelemy, K. Bouzehouane, E. Jacquet, A. Khodan, J. P. Contour, S. Fusil, F. Wyczisk, A. Forget, D. Lebeugle, D. Colson, and M. Viret, Applied Physics Letters **87,** 072508 (2005).

[65] N. Sai, B. Meyer, and D. Vanderbilt, Physical Review Letters **84,** 5636-5639 (2000).

[66] C. G. Duan, S. S. Jaswal, and E. Y. Tsymbal, Physical Review Letters **97,** 047201 (2006).

[67] H. Tanaka, J. Zhang, and T. Kawai, Physical Review Letters **88,** 027204 (2002).

[68] H. Zheng, J. Wang, S. E. Lofland, Z. Ma, L. Mohaddes-Ardabili, T. Zhao, L. Salamanca-Riba, S. R. Shinde, S. B. Ogale, F. Bai, D. Viehland, Y. Jia, D. G. Schlom, M. Wuttig, A. Roytburd, and R. Ramesh, Science **303,** 661-663 (2004).

[69] H. Zheng, Q. Zhan, F. Zavaliche, M. Sherburne, F. Straub, M. P. Cruz, L. Q. Chen, U. Dahmen, and R. Ramesh, Nano Letters **6,** 1401-1407 (2006).

[70] J. H. Li, I. Levin, J. Slutsker, V. Provenzano, P. K. Schenck, R. Ramesh, J. Ouyang, and A. L. Roytburd, Applied Physics Letters **87,** 072909 (2005).

[71] J. G. Wan, X. W. Wang, Y. J. Wu, M. Zeng, Y. Wang, H. Jiang, W. Q. Zhou, G. H. Wang, and J. M. Liu, Applied Physics Letters **86,** 122501 (2005).

[72] J. X. Zhang, D. G. Schlom, L. Q. Chen, and C. B. Eom, Applied Physics Letters **95,** 122904 (2009).

[73] J. F. Scott, Nature Materials **6,** 256-257 (2007).

[74] H. Wang, S. R. Foltyn, P. N. Arendt, Q. X. Jia, J. L. MacManus-Driscoll, L. Stan, Y. Li, X. Zhang, and P. C. Dowden, Journal of Materials Research **19,** 1869-1875 (2004).

[75] J. Narayan and B. C. Larson, Journal of Applied Physics **93,** 278-285 (2003).

[76] A. J. Millis, T. Darling, and A. Migliori, Journal of Applied Physics **83,** 1588-1591 (1998).

[77] L. Ranno, A. Llobet, R. Tiron, and E. Favre-Nicolin, Applied Surface Science **188,** 170-175 (2002).

[78] W. Zhong and D. Vanderbilt, Physical Review Letters **74,** 2587-2590 (1995).

[79] B. Noheda, J. A. Gonzalo, L. E. Cross, R. Guo, S. E. Park, D. E. Cox, and G. Shirane, Physical Review B **61,** 8687-8695 (2000).

[80] D. I. Bilc and D. J. Singh, Physical Review Letters **96,** 147602 (2006).

[81] A. J. Hatt and N. A. Spaldin, Applied Physics Letters **90,** 242916 (2007).

[82] D. Fuchs, E. Arac, C. Pinta, S. Schuppler, R. Schneider, and H. V. von Lohneysen, Physical Review B **77,** 014434 (2008).

[83] D. Fuchs, L. Dieterle, E. Arac, R. Eder, P. Adelmann, V. Eyert, T. Kopp, R. Schneider, D. Gerthsen, and H. von Lohneysen, Physical Review B **79,** 24424 (2009).

[84] H. Alison, Dissertation, University of California, Santa Barbara, 2010.

[85] N. A. Pertsev, A. G. Zembilgotov, and A. K. Tagantsev, Physical Review Letters **80,** 1988-1991 (1998).

[86] Y. L. Li, S. Y. Hu, Z. K. Liu, and L. Q. Chen, Applied Physics Letters **78,** 3878-3880 (2001).

[87] N. A. Pertsev, V. G. Kukhar, H. Kohlstedt, and R. Waser, Physical Review B **67,** 054107 (2003).

[88] J. H. Haeni, P. Irvin, W. Chang, R. Uecker, P. Reiche, Y. L. Li, S. Choudhury, W. Tian, M. E. Hawley, B. Craigo, A. K. Tagantsev, X. Q. Pan, S. K. Streiffer, L. Q. Chen, S. W. Kirchoefer, J. Levy, and D. G. Schlom, Nature **430,** 758-761 (2004).

[89] R. J. Zeches, M. D. Rossell, J. X. Zhang, A. J. Hatt, Q. He, C. H. Yang, A. Kumar, C. H. Wang, A. Melville, C. Adamo, G. Sheng, Y. H. Chu, J. F. Ihlefeld, R. Erni, C. Ederer, V. Gopalan, L. Q. Chen, D. G. Schlom, N. A. Spaldin, L. W. Martin, and R. Ramesh, Science **326,** 977-980 (2009).

[90] P. Hansmann, X. P. Yang, A. Toschi, G. Khaliullin, O. K. Andersen, and K. Held, Physical Review Letters **103,** 016401 (2009).

[91] M. T. Yin and M. L. Cohen, Physical Review B **26,** 5668-5687 (1982).

[92] V. L. Moruzzi, A. R. Williams, and J. F. Janak, Physical Review B **15,** 2854-2857 (1977).

[93] A. G. Lehmann, C. Sanna, F. Congiu, G. Concas, and L. Maritato, Physica Status Solidi B-Basic Solid State Physics **246,** 1948-1955 (2009).

[94] C. Adamo, X. Ke, H. Q. Wang, H. L. Xin, T. Heeg, M. E. Hawley, W. Zander, J. Schubert, P. Schiffer, D. A. Muller, L. Maritato, and D. G. Schlom, Applied Physics Letters **95,** 112504 (2009).

[95] A. R. James and X. X. Xi, Journal of Applied Physics **92,** 6149-6152 (2002).

[96] Z. C. Zhang, Y. H. Chen, S. Y. Yang, F. Q. Zhang, B. S. Ma, B. Xu, Y. P. Zeng, Z. G. Wang, and X. P. Zhang, Semiconductor Science and Technology **18,** 955-959 (2003).

[97] D. G. Schlom, J. H. Haeni, J. Lettieri, C. D. Theis, W. Tian, J. C. Jiang, and X. Q. Pan, Materials Science and Engineering B-Solid State Materials for Advanced Technology **87,** 282-291 (2001).

[98] D. A. Tenne, A. Bruchhausen, N. D. Lanzillotti-Kimura, A. Fainstein, R. S. Katiyar, A. Cantarero, A. Soukiassian, V. Vaithyanathan, J. H. Haeni, W. Tian, D. G. Schlom, K. J. Choi, D. M. Kim, C. B. Eom, H. P. Sun, X. Q. Pan, Y. L. Li, L. Q. Chen, Q. X. Jia, S. M. Nakhmanson, K. M. Rabe, and X. X. Xi, Science **313,** 1614-1616 (2006).

[99] E. Weal, S. Patnaik, Z. Bi, H. Wang, T. Fix, A. Kursumovic, and J. L. M. Driscoll, Applied Physics Letters **97,** 153121 (2010).

[100] J. L. Macmanus-Driscoll, P. Zerrer, H. Y. Wang, H. Yang, J. Yoon, A. Fouchet, R. Yu, M. G. Blamire, and Q. X. Jia, Nature Materials **7,** 314-320 (2008).

[101] W. Lee, H. Han, A. Lotnyk, M. A. Schubert, S. Senz, M. Alexe, D. Hesse, S. Baik, and U. Gosele, Nature Nanotechnology **3,** 402-407 (2008).

[102] Z. Bi, O. Anderoglu, X. H. Zhang, J. L. MacManus-Driscoll, H. Yang, Q. X. Jia, and H. Y. Wang, Nanotechnology **21,** 285606 (2010).

[103] H. Yang, H. Y. Wang, J. Yoon, Y. Q. Wang, M. Jain, D. M. Feldmann, P. C. Dowden, J. L. MacManus-Driscoll, and Q. X. Jia, Advanced Materials **21,** 3794-3798 (2009).

[104] S. O. Kim, H. H. Solak, M. P. Stoykovich, N. J. Ferrier, J. J. de Pablo, and P. F. Nealey, Nature **424,** 411-414 (2003).

[105] Y. Le Bouar, A. Loiseau, and A. G. Khachaturyan, Acta Materialia **46,** 2777-2788 (1998).

[106] S. A. Koster, V. Moshnyaga, K. Samwer, O. I. Lebedev, G. van Tendeloo, O. Shapoval, and A. Belenchuk, Applied Physics Letters **81,** 1648-1650 (2002).

[107] Z. Bi, H. Wang, submitted to Journal of Applied Physics, (2011).

[108] I. Fina, N. Dix, L. Fabrega, F. Sanchez, and J. Fontcuberta, Journal of Applied Physics **108,** 034108 (2010).

[109] H. M. Zheng, F. Straub, Q. Zhan, P. L. Yang, W. K. Hsieh, F. Zavaliche, Y. H. Chu, U. Dahmen, and R. Ramesh, Advanced Materials **18,** 2747 (2006).

[110] I. Levin, J. H. Li, J. Slutsker, and A. L. Roytburd, Advanced Materials **18,** 2044 (2006).

[111] N. Ortega, P. Bhattacharya, R. S. Katiyar, P. Dutta, A. Manivannan, M. S. Seehra, I. Takeuchi, and S. B. Majumder, Journal of Applied Physics **100,** 126105 (2006).

[112] H. Ryu, P. Murugavel, J. H. Lee, S. C. Chae, T. W. Noh, Y. S. Oh, H. J. Kim, K. H. Kim, J. H. Jang, M. Kim, C. Bae, and J. G. Park, Applied Physics Letters **89,** 102907 (2006).

[113] H. M. Luo, H. Yang, S. A. Bally, O. Ugurlu, M. Jain, M. E. Hawley, T. M. McCleskey, A. K. Burrell, E. Bauer, L. Civale, T. G. Holesinger, and Q. X. Jia, Journal of the American Chemical Society **129,** 14132 (2007).

[114] Z. X. Bi, J. H. Lee, H. Yang, Q. X. Jia, J. L. MacManus-Driscoll, and H. Y. Wang, Journal of Applied Physics **106,** 094309 (2009).

[115] S. Harrington, Z. Bi, H. Wang, J. L. Macmanus-Driscoll, submitted to Nature Nanotechnology, (2011).

[116] K. Pohl, M. C. Bartelt, J. de la Figuera, N. C. Bartelt, J. Hrbek, and R. Q. Hwang, Nature **397,** 238-241 (1999).

[117] H. Takeshita, Y. Suzuki, H. Akinaga, W. Mizutani, K. Tanaka, T. Katayama, and A. Itoh, Applied Physics Letters **68,** 3040-3042 (1996).

[118] V. A. Shchukin and D. Bimberg, Reviews of Modern Physics **71,** 1125-1171 (1999).

[119] C. Teichert, Physics Reports-Review Section of Physics Letters **365,** 335-432 (2002).

[120] A. Putnis, *Introduction to Mineral Sciences* (Cambridge University Press, Cambridge, 1992).

[121] H. Zheng, Dissertation, University of Maryland, College Park, 2004.

[122] Q. Zhan, R. Yu, S. P. Crane, H. Zheng, C. Kisielowski, and R. Ramesh, Applied Physics Letters **89,** 172902 (2006).

[123] J. V. Suchtelen, Philips Research Reports **27,** 28-37 (1972).

[124] J. Vandenboomgaard and R. A. J. Born, Journal of Materials Science **13,** 1538-1548 (1978).

[125] G. Harshe, J. P. Gougherty, and R. E. Newnham, International Journal of Applied Electromagnetics in Materials **4,** 145-159 (1993).

[126] I. Levin, J. Slutsker, J. H. Li, Z. P. Tan, and A. L. Roytburd, Applied Physics Letters **91,** 062912 (2007).

[127] M. Murakami, S. Fujino, S. H. Lim, L. G. Salamanca-Riba, M. Wuttig, I. Takeuchi, B. Varughese, H. Sugaya, T. Hasegawa, and S. E. Lofland, Applied Physics Letters **88,** 112505 (2006).

[128] F. Zavaliche, H. Zheng, L. Mohaddes-Ardabili, S. Y. Yang, Q. Zhan, P. Shafer, E. Reilly, R. Chopdekar, Y. Jia, P. Wright, D. G. Schlom, Y. Suzuki, and R. Ramesh, Nano Letters **5,** 1793-1796 (2005).

[129] F. Zavaliche, T. Zhao, H. Zheng, F. Straub, M. P. Cruz, P. L. Yang, D. Hao, and R. Ramesh, Nano Letters **7,** 1586-1590 (2007).

[130] A. E. Berkowitz and K. Takano, Journal of Magnetism and Magnetic Materials **200,** 552-570 (1999).

[131] J. Nogues and I. K. Schuller, Journal of Magnetism and Magnetic Materials **192,** 203-232 (1999).

[132] E. Weal, Applied Physics Letters, in press (2011).

[133] W. L. Winterbo, Acta Metallurgica **15,** 303-310 (1967).

[134] L. Mohaddes-Ardabili, H. Zheng, S. B. Ogale, B. Hannoyer, W. Tian, J. Wang, S. E. Lofland, S. R. Shinde, T. Zhao, Y. Jia, L. Salamanca-Riba, D. G. Schlom, M. Wuttig, and R. Ramesh, Nature Materials **3,** 533-538 (2004).

[135] J. L. MacManus-Driscoll, Advanced Functional Materials **20,** 2035-2045 (2010).

[136] R. Eason, *Pulsed Laser Deposition of Thin Films: Applications-Led Growth of Functional Materials* (Wiley, New York, 2006).

[137] R. K. Singh, O. W. Holland, and J. Narayan, Journal of Applied Physics **68,** 233-247 (1990).

[138] R. K. Singh and J. Narayan, Physical Review B **41,** 8843-8859 (1990).

[139] T. C. Jeffrey, *History and Fundamentals of Pulsed Laser Deposition, Pulsed Laser Deposition of Thin Films* (Wiley, New York, 1994).

[140] G. J. H. M. Rijnders, G. Koster, D. H. A. Blank, and H. Rogalla, Applied Physics Letters **70,** 1888-1890 (1997).

[141] C. Suryanarayana and M. G. Norton, *X-Ray Diffraction: A Practical Approach* (Springer, New York, 1998).

[142] J. Als-Nielsen and D. McMorrow, *Elements of Modern X-ray Physics* (John Wiley & Sons Ltd., West Sussex UK, 2001).

[143] V. Holy, U. Pietsch, and T. Baumbach, *High Resolution X-ray Scattering from Thin Films and Multilayers* (Springer, Berlin, 2003).

[144] B. Fultz and J. Howe, *Transmission Electron Microscopy and Diffractometry of Materials*, 3rd ed. (Springer, Berlin, 2007).

[145] P. J. Goodhew, F. J. Humphreys, and R. Beanland, *Electron Microscopy and Analysis,* (Taylor & Francis, New York, 2000).

[146] M. A. O'Keefe, Proceedings of the 3rd Pfeffercorn Conference on Electron Optical Systems, 209-220 (1984).

[147] D. B. Williams and C. B. Carter, *Transmission Electron Microscopy A Textbook for Materials Science*, 2nd ed. (Springer, New York, 2008).

[148] Y. H. Chu, L. W. Martin, Q. Zhan, P. L. Yang, M. P. Cruz, K. Lee, M. Barry, S. Y. Yang, and R. Ramesh, Ferroelectrics **354,** 167-177 (2007).

[149] D. N. R. V. A. Murashiov, V. M. Ionov, I. S. Dubeko, and Y. V. Titov, Ferroelectrics **164,** 4 (1994).

[150] Y. F. Popov, A. M. Kadomtseva, G. P. Vorobev, and A. K. Zvezdin, Ferroelectrics **162,** 135-140 (1994).

[151] J. Kabelac, S. Ghosh, P. Dobal, and R. Katiyar, Journal of Vacuum Science & Technology B **25,** 1049-1052 (2007).

[152] S. Iakovlev, C. H. Solterbeck, M. Kuhnke, and M. Es-Souni, Journal of Applied Physics **97,** 094901 (2005).

[153] A. A. Dakhel, Journal of Alloys and Compounds **365,** 233-239 (2004).

[154] V. A. Rozhkov, A. Y. Trusova, and I. G. Berezhnoy, Thin Solid Films **325,** 151-155 (1998).

[155] M. Fanciulli and G. Scale, *Rare Earth Oxide Thin Film: Growth, Characterization, and Applications*, Vol. 106 (Springer, Berlin, 2007).

[156] M. P. Cruz, Y. H. Chu, J. X. Zhang, P. L. Yang, F. Zavaliche, Q. He, P. Shafer, L. Q. Chen, and R. Ramesh, Physical Review Letters **99,** 217601 (2007).

[157] Y. H. Lee, J. M. Wu, Y. L. Chueh, and L. J. Chou, Applied Physics Letters **87,** 172901 (2005).

[158] K. Saito, A. Ulyanenkov, V. Grossmann, H. Ress, L. Bruegemann, H. Ohta, T. Kurosawa, S. Ueki, and H. Funakubo, Japanese Journal of Applied Physics, Part 1: Regular Papers, Short Notes & Review Papers **45,** 7311 (2006).

[159] H. Yang, H. Wang, H. M. Luo, D. M. Feldmann, P. C. Dowden, R. F. DePaula, and Q. X. Jia, Applied Physics Letters **92,** 142904 (2008).

[160] R. J. Keyse, *Royal Microscopical, Introduction to Scanning Transmission Electron Microscopy* (Springer, New York, 1998).

[161] J. M. D. Coey, M. Viret, and S. von Molnar, Advances in Physics **48,** 167-293 (1999).

[162] A. M. Haghiri-Gosnet and J. P. Renard, Journal of Physics D-Applied Physics **36,** R127-R150 (2003).

[163] W. Prellier, P. Lecoeur, and B. Mercey, Journal of Physics-Condensed Matter **13,** R915-R944 (2001).

[164] H. Y. Hwang, S. W. Cheong, N. P. Ong, and B. Batlogg, Physical Review Letters **77,** 2041-2044 (1996).

[165] P. K. Siwach, H. K. Singh, and O. N. Srivastava, Journal of Physics-Condensed Matter **20,** 273201 (2008).

[166] F. Guinea, Physical Review B **58,** 9212-9216 (1998).

[167] L. Balcells, A. E. Carrillo, B. Martinez, and J. Fontcuberta, Applied Physics Letters **74,** 4014-4016 (1999).

[168] Y. M. Kang, H. J. Kim, and S. I. Yoo, Applied Physics Letters **95,** 052510 (2009).

[169] D. Das, A. Saha, S. E. Russek, R. Raj, and D. Bahadur, Journal of Applied Physics **93,** 8301-8303 (2003).

[170] P. Kameli, H. Salamati, M. Eshraghi, and M. R. Mohammadizadeh, Journal of Applied Physics **98,** 043908 (2005).

[171] D. K. Petrov, L. Krusin-Elbaum, J. Z. Sun, C. Feild, and P. R. Duncombe, Applied Physics Letters **75,** 995-997 (1999).

[172] S. Gupta, R. Ranjit, C. Mitra, P. Raychaudhuri, and R. Pinto, Applied Physics Letters **78,** 362-364 (2001).

[173] B. Vertruyen, R. Cloots, M. Ausloos, J. F. Fagnard, and P. Vanderbemden, Physical Review B **75,** 165112 (2007).

[174] J. A. M. Vanroosmalen, P. Vanvlaanderen, E. H. P. Cordfunke, W. L. Ijdo, and D. J. W. Ijdo, Journal of Solid State Chemistry **114,** 516-523 (1995).

[175] Y. F. Lu, J. Klein, F. Herbstritt, J. B. Philipp, A. Marx, and R. Gross, Physical Review B **73,** 054302 (2006).

[176] F. Tsui, M. C. Smoak, T. K. Nath, and C. B. Eom, Applied Physics Letters **76,** 2421-2423 (2000).

[177] V. Moshnyaga, S. Klimm, R. Tidecks, S. Horn, and K. Samwer, Journal of Magnetism and Magnetic Materials **211,** 167-172 (2000).

[178] M. Koubaa, A. M. Haghiri-Gosnet, R. Desfeux, P. Lecoeur, W. Prellier, and B. Mercey, Journal of Applied Physics **93,** 5227-5235 (2003).

[179] O. Y. Gorbenko, S. V. Samoilenkov, I. E. Graboy, and A. R. Kaul, Chemistry of Materials **14,** 4026-4043 (2002).

[180] L. W. Guo, D. L. Peng, H. Makino, K. Inaba, H. J. Ko, K. Sumiyama, and T. Yao, Journal of Magnetism and Magnetic Materials **213,** 321-325 (2000).

[181] A. V. Narlikar, *Frontiers in Magnetic Materials* (Springer, New York, 2005).

[182] T. Suzuki and T. Katsufuji, Physical Review B **77,** 054412 (2008).

[183] N. N. Zhao, W. Nie, X. B. Liu, S. Z. Tian, Y. Zhang, and X. L. Ji, Small **4,** 77-81 (2008).

[184] W. Z. Wang, C. K. Xu, G. H. Wang, Y. K. Liu, and C. L. Zheng, Advanced Materials **14,** 837-840 (2002).

[185] W. X. Zhang, C. Wang, X. M. Zhang, Y. Xie, and Y. T. Qian, Solid State Ionics **117,** 331-335 (1999).

[186] D. Jarosch, Mineralogy and Petrology **37,** 15-23 (1987).

[187] N. N. Greenwood and A. Earnshaw, *Chemistry of the Elements*, 2nd ed. (Butterworth-Heinemann, Oxford, 1997).

[188] O. Y. Gorbenko, I. E. Graboy, V. A. Amelichev, A. A. Bosak, A. R. Kaul, B. Guttler, V. L. Svetchnikov, and H. W. Zandbergen, Solid State Communications **124,** 15-20 (2002).

[189] J. H. Song, J. H. Park, Y. H. Jeong, and T. Y. Koo, Physica B-Condensed Matter **312,** 729-731 (2002).

[190] R. A. Rao, D. Lavric, T. K. Nath, C. B. Eom, L. Wu, and F. Tsui, Applied Physics Letters **73,** 3294-3296 (1998).

[191] T. Suzuki, I. Kosacki, H. U. Anderson, and P. Colomban, Journal of the American Ceramic Society **84,** 2007-2014 (2001).

[192] J. H. Lee, C. Y. Chou, Z. X. Bi, C. F. Tsai, and H. Y. Wang, Nanotechnology **20,** 395704 (2009).

[193] B. L. Zhu, X. Z. Zhao, S. Xu, F. H. Su, G. H. Li, X. G. Wu, J. Wu, R. Wu, and J. Liu, Japanese Journal of Applied Physics **47,** 2225-2229 (2008).

[194] O. Nilsen, H. Fjellvag, and A. Kjekshus, Thin Solid Films **444,** 44-51 (2003).

[195] O. Nilsen, S. Foss, H. Fjellvag, and A. Kjekshus, Thin Solid Films **468,** 65-74 (2004).

[196] L. W. Guo, H. J. Ko, H. Makino, Y. F. Chen, K. Inaba, and T. Yao, Journal of Crystal Growth **205,** 531-536 (1999).

[197] S. Isber, E. Majdalani, M. Tabbal, T. Christidis, K. Zahraman, and B. Nsouli, Thin Solid Films **517,** 1592-1595 (2009).

[198] T. Maruyama and Y. Osaki, Journal of the Electrochemical Society **142,** 3137-3141 (1995).

[199] V. Caslavsk and R. Roy, Journal of Applied Physics **41,** 825 (1970).

[200] H. W. Nesbitt and D. Banerjee, American Mineralogist **83,** 305-315 (1998).

[201] J. H. Song, T. Susaki, and H. Y. Hwang, Advanced Materials **20,** 2528-2532 (2008).

[202] Z. Y. Zhang and M. G. Lagally, Science **276,** 377-383 (1997).

[203] K. Dwight and N. Menyuk, Physical Review **119,** 1470-1479 (1960).

[204] I. S. Jacobs, Journal of Physics and Chemistry of Solids **11,** 1-11 (1959).

[205] L. Lu, Q. Li, L. Li, and M. Zheng, Optoelectronics Letters **3,** 20-25 (2006).

[206] Z. Zhang and M. G. Lagally, Science **276,** 377-383 (1997).

[207] S. F. Corbin, R. M. C. Clemmer, and Q. Yang, Journal of the American Ceramic Society **92,** 331-337 (2009).

[208] X. W. Teng, X. Y. Liang, S. Rahman, and H. Yang, Advanced Materials **17,** 2237-2241 (2005).

[209] S. Jou and T. H. Wu, Journal of Physics and Chemistry of Solids **69,** 2804-2812 (2008).

[210] E. Kjeang, R. Michel, D. A. Harrington, N. Djilali, and D. Sinton, Journal of the American Chemical Society **130,** 4000-4006 (2008).

[211] M. Yoshikawa, A. Boden, M. Sparr, and G. Lindbergh, Journal of Power Sources **158,** 94-102 (2006).

[212] Q. Zhang, L. V. Saraf, J. R. Smitha, P. Jha, and F. Hua, Sensors and Actuators A - Physical **151,** 154-158 (2009).

[213] V. Aroutiounian, V. Arakelyan, V. Galstyan, K. Martirosyan, and P. Soukiassian, IEEE Sensors Journal **9,** 9-12 (2009).

[214] H. M. Martinez, N. E. Rincon, J. Torres, and J. E. Alfonso, Microelectronics Journal **39,** 1354-1355 (2008).

[215] J. E. Houser and K. R. Hebert, Nature Materials **8,** 415-420 (2009).

[216] F. Yang, B. Y. Xie, J. Z. Sun, H. K. Jin, and M. Wang, Materials Letters **62,** 1302-1304 (2008).

[217] M. L. Tian, S. Y. Xu, J. G. Wang, N. Kumar, E. Wertz, Q. Li, P. M. Campbell, M. H. W. Chan, and T. E. Mallouk, Nano Letters **5,** 697-703 (2005).

[218] J. H. Joo and G. M. Choi, Solid State Ionics **178,** 1602-1607 (2007).

[219] X. Q. Ma, J. X. Dai, H. Zhang, J. Roth, T. D. Xiao, and D. E. Reisner, Journal of Fuel Cell Science and Technology **2,** 190-196 (2005).

[220] B. Lin, W. P. Sun, K. Xie, Y. C. Dong, D. H. Dong, X. Q. Liu, J. F. Gao, and G. Y. Meng, Journal of Alloys and Compounds **465,** 285-290 (2008).

[221] D. Ding, L. Li, K. Feng, Z. B. Liu, and C. R. Xia, Journal of Power Sources **187,** 400-402 (2009).

[222] J. P. Liu, Y. Y. Li, X. T. Huang, G. Y. Li, and Z. K. Li, Advanced Functional Materials **18,** 1448-1458 (2008).

[223] Y. F. Gao, A. Nagai, Y. Masuda, F. Sato, W. S. Seo, and K. Koumoto, Langmuir **22,** 3521-3527 (2006).

[224] Y. Hayashi, H. Ohtake, J. Kawahara, M. Tada, S. Saito, N. Inoue, F. Ito, M. Tagami, M. Ueki, N. Furutake, T. Takeuchi, H. Yamamoto, and M. Abe, IEEE Transactions on Semiconductor Manufacturing **21,** 469-480 (2008).

[225] C. S. Solanki, R. R. Bilyalov, J. Poortmans, J. P. Celis, and J. Nijs, Physica Status Solidi A - Applied Research **197,** 507-511 (2003).

[226] S. L. Chou, J. Z. Wang, H. K. Liu, and S. X. Dou, Journal of Power Sources **182,** 359-364 (2008).

[227] B. Djurfors, J. N. Broughton, M. J. Brett, and D. G. Ivey, Journal of the Electrochemical Society **153,** A64-A68 (2006).

[228] M. Ohmukai, K. Okada, and Y. Tsutsumi, Journal of Materials Science-Materials in Electronics **16,** 119-121 (2005).

[229] M. Nakao, S. Oku, T. Tamamura, K. Yasui, and H. Masuda, Japanese Journal of Applied Physics Part 1-Regular Papers Short Notes & Review Papers **38,** 1052-1055 (1999).

[230] V. Moshnyaga, B. Damaschke, O. Shapoval, A. Belenchuk, J. Faupel, O. I. Lebedev, J. Verbeeck, G. Van Tendeloo, M. Mucksch, V. Tsurkan, R. Tidecks, and K. Samwer, Nature Materials **2,** 247-252 (2003).

[231] F. Tyholdt, S. Jorgensen, H. Fjellvag, and A. E. Gunnaes, Journal of Materials Research **20,** 2127-2139 (2005).

[232] J. Mukherje and F. F. Y. Wang, Journal of the American Ceramic Society **54,** 31-34 (1971).

[233] O. V. Andreev, A. S. Vysokikh, and V. G. Vaulin, Russian Journal of Inorganic Chemistry **53,** 1320-1324 (2008).

VITA

Zhenxing Bi received his B.E. and M.E. degrees both in electrical engineering from Tianjin University, Tianjin, China in 2004 and 2007, respectively. He joined the Wang functional thin films group at TAMU in fall 2007 and received his Ph.D. degree in electrical engineering in May 2011. His research interests include functional oxide thin films, the film microstructure-property relationships and electron microscopy. He published 13 journal articles and 15 conference presentations during his Ph.D. study at TAMU.

Zhenxing Bi may be reached at Department of Electrical and Computer Engineering, Texas A&M University, College Station, TX 77843. His email is zhenxingbi@yahoo.com.